12. Short and Ultrashort Laser Pulses

In this contribution some basic properties of femtosecond laser pulses are summarized. In Sect. 12.1 we start with the linear properties of ultrashort light pulses. Nonlinear optical effects that would alter the frequency spectrum of an ultrashort pulse are not considered. However, due to the large bandwidth, the linear dispersion is responsible for dramatic effects. For example, a 10 fs laser pulse at a center wavelength of 800 nm propagating through 4 mm of BK7 glass will be temporally broadened to 50 fs. In order to describe and manage such dispersion effects a mathematical description of an ultrashort laser pulse is given first before we continue with methods how to change the temporal shape via the frequency domain. The chapter ends with a paragraph on the powerful technique of pulse shaping, which can be used to create complex-shaped ultrashort laser pulses with respect to phase, amplitude and polarization state.

In Sect. 12.2 the generation of femtosecond laser pulses via mode locking is described in simple physical terms. As femtosecond laser pulses can be generated directly from a wide variety of lasers with wavelengths ranging from the ultraviolet to the infrared no attempt is made to cover the different technical approaches.

Part C | 12

In Sect. 12.3 we deal with the measurement of ultrashort pulses. Traditionally a short event has been characterized with the aid of an even shorter event. This is not an option for ultrashort light pulses. The characterization of ultrashort pulses with respect to amplitude and phase is therefore based on optical correlation techniques that make use of the short pulse itself. Methods operating in the time–frequency domain are especially useful.

A central building block for generating femtosecond light pulses are lasers. Within only two decades of the invention of the laser the duration of the shortest pulse shrunk by six orders of magnitude from the nanosecond regime to the femtosecond regime. Nowadays femtosecond pulses in the range of 10 fs and below can be generated directly from compact and reliable laser oscillators and the temporal resolution of measurements has outpaced the resolution even of modern sampling oscilloscopes by orders of magnitude. With the help of some simple comparisons the incredibly fast femtosecond time scale can be put into perspective: on a logarithmic time scale one minute is approximately half-way between 10 fs and the age of the universe. Taking the speed of light in vacuum into account, a 10 fs light pulse can be considered as a 3 μm thick slice of light whereas a light pulse of one second spans approximately the distance between earth and moon. It is also useful to realize that the fastest molecular vibrations in nature have an oscillation time of about 10 fs.

It is the unique attributes of these light pulses that open up new frontiers both in basic research and for applications. The *ultrashort pulse duration* for example allows the motion of electrons and molecules to be frozen by making use of so-called pump probe techniques that work similar to strobe light techniques. In chemistry complex reaction dynamics have been

measured directly in the time domain and this work was rewarded with the Nobel price in chemistry for A. H. Zewail in 1999. The *broad spectral width* can be used for example in medical diagnostics or – by taking the longitudinal frequency comb mode structure into account – for high-precision optical frequency metrology. The latter is expected to outperform today's state-of-the-art caesium clocks and was rewarded with the 2005 Nobel price in physics for J. L. Hall and T. W. Hänsch. The extreme concentration of a modest energy content in focused femtosecond pulses delivers *high peak intensities* that are used for example in a reversible light matter interaction regime for the development of nonlinear microscopy techniques. The irreversible light matter regime can be for example applied to nonthermal ma-

terial processing leading to precise microstructures in a whole variety of solid state materials. Finally the *high pulse repetition rate* is exploited, for example, in telecommunication applications.

These topics have been reviewed recently in [12.1]. The biannual international conference series *Ultrafast Phenomena* and *Ultrafast Optics*, including the corresponding conference proceedings, cover a broad range of applications and latest developments.

Besides the specific literature given in the individual chapters some textbooks devoted to ultrafast laser pulses are recommended for a more in-depth discussion of the topics presented here and beyond (see, for example, [12.2–5] and especially for the measurement of ultrashort pulses see [12.6]).

12.1 Linear Properties of Ultrashort Light Pulses

12.1.1 Descriptive Introduction

It is quite easy to construct the electric field of a *Gedanken* optical pulse at a fixed position in space, corresponding to the physical situation of a fixed detector in space. Assuming the light field to be linearly

Fig. 12.1a–d Electric field $E(t)$ and temporal amplitude function $A(t)$ for a cosine pulse **(a)**, a sine pulse **(b)**, an up-chirped pulse **(c)** and a down-chirped pulse **(d)**. The pulse duration in all cases is $\Delta t = 5$ fs. For **(c)** and **(d)** the parameter a was chosen to be $\pm 0.15/\text{fs}^2$

polarized, we may write the real electric field strength $E(t)$ as a scalar quantity whereas a harmonic wave is multiplied with a temporal amplitude or envelope function $A(t)$
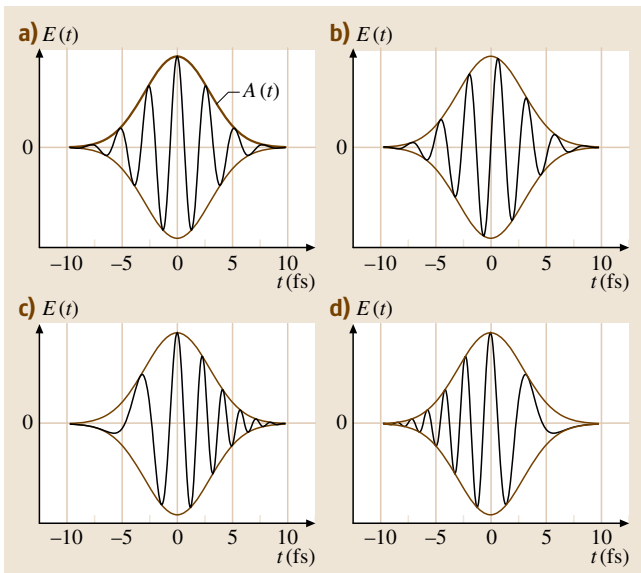
$$E(t) = A(t)\cos(\Phi_0 + \omega_0 t) \tag{12.1}$$

with ω_0 being the carrier circular (or angular) frequency. The light frequency is given by $\nu_0 = \omega_0/2\pi$. In the following, angular frequencies and frequencies are only distinguished from each other via their notation. For illustration we will use optical pulses centered at 800 nm, corresponding to a carrier frequency of $\omega_0 = 2.35$ rad/fs (oscillation period $T = 2.67$ fs) with a Gaussian envelope function (the numbers refer to pulses that are generated by the widely spread femtosecond laser systems based on Ti:sapphire as the active medium). For simple envelope functions the pulse duration Δt is usually defined by the FWHM (full width at half-maximum) of the temporal intensity function $I(t)$

$$I(t) = \frac{1}{2}\varepsilon_0 c n A(t)^2 , \tag{12.2}$$

with ε_0 being the vacuum permittivity, c the speed of light and n the refractive index. The factor $1/2$ arises from averaging the oscillations. If the temporal intensity is given in W/cm^2 the temporal amplitude $A(t)$ (in V/cm for $n = 1$) is given by

$$A(t) = \sqrt{\frac{2}{\varepsilon_0 c}}\sqrt{I(t)} = 27.4\sqrt{I(t)} . \tag{12.3}$$

Figure 12.1a displays $E(t)$ for a Gaussian pulse with $\Delta t = 5$ fs and $\Phi_0 = 0$. At $t = 0$ the electric field strength

reaches its maximum value. This situation is called a cosine pulse: for $\Phi_0 = -\pi/2$ we get a sine pulse $E(t) = A(t)\sin(\omega_0 t)$ (Fig. 12.1b) where the maxima of the carrier oscillations do not coincide with the maximum of the envelope $A(t)$ at $t = 0$ and the maximum value of $E(t)$ is therefore smaller than in a cosine pulse. In general Φ_0 is termed the absolute phase or carrier-envelope phase and determines the temporal relation of the pulse envelope with respect to the underlying carrier oscillation. The absolute phase is not important if the pulse envelope $A(t)$ does not significantly vary within one oscillation period T. The longer the temporal duration of the pulses, the more closely this condition is met and the decomposition of the electric field into an envelope function and a harmonic oscillation with carrier frequency ω_0 (12.1) is meaningful. Conventional pulse characterization methods as described in Sect. 12.3 are not able to measure the absolute value of Φ_0. Furthermore the absolute phase does not remain stable in a conventional femtosecond laser system. Progress in controlling and measuring the absolute phase has been made only recently [12.7–10] and experiments depending on the absolute phase are starting to appear [12.11–13]. In the following we will not emphasize the role of Φ_0 any more.

In general, we may add an additional time dependent phase function $\Phi_a(t)$ to the temporal phase term in (12.1)

$$\Phi(t) = \Phi_0 + \omega_0 t + \Phi_a(t) \tag{12.4}$$

and define the momentary or instantaneous light frequency $\omega(t)$ as

$$\omega(t) = \frac{\mathrm{d}\Phi(t)}{\mathrm{d}t} = \omega_0 + \frac{\mathrm{d}\Phi_a(t)}{\mathrm{d}t} . \tag{12.5}$$

This additional phase function describes variations of the frequency in time, called a chirp. In Fig. 12.1c,d $\Phi_a(t)$ is set to be at^2. For $a = 0.15/\mathrm{fs}^2$ we see a linear increase of the frequency in time, called a linear up-chirp. For $a = -0.15/\mathrm{fs}^2$ a linear down-chirped pulse is obtained with a linear decrease of the frequency in time. However, a direct manipulation of the temporal phase cannot be achieved by any electronic device. Note that nonlinear optical processes such as, for example, self-phase modulation (SPM) are able to influence the temporal phase and lead to a change in the frequency spectrum of the pulse. In this chapter we will mainly focus on linear optical effects where the spectrum of the pulse is unchanged and changes in the temporal pulse shape are due to manipulations in the frequency domain (Sect. 12.1.3). Before we start, a more mathematical description of an ultrashort light pulse is presented.

12.1.2 Mathematical Description

For the mathematical description we followed the approaches of [12.4, 14–19]. In linear optics the superposition principle holds and the real-valued electric field $E(t)$ of an ultrashort optical pulse at a fixed point in space has the Fourier decomposition into monochromatic waves

$$E(t) = \frac{1}{2\pi} \int_{-\infty}^{\infty} \tilde{E}(\omega)\,\mathrm{e}^{\mathrm{i}\omega t}\,\mathrm{d}\omega . \tag{12.6}$$

The, in general complex-valued, spectrum $\tilde{E}(\omega)$ is obtained by the Fourier inversion theorem

$$\tilde{E}(\omega) = \int_{-\infty}^{\infty} E(t)\,\mathrm{e}^{-\mathrm{i}\omega t}\,\mathrm{d}t . \tag{12.7}$$

Since $E(t)$ is real-valued $\tilde{E}(\omega)$ is Hermitian, i. e., obeys the condition

$$\tilde{E}(\omega) = \tilde{E}^*(-\omega) , \tag{12.8}$$

where $*$ denotes complex conjugation. Hence knowledge of the spectrum for positive frequencies is sufficient for a full characterization of a light field without DC component we can define the positive part of the spectrum as

$$\begin{aligned} \tilde{E}^+(\omega) &= \tilde{E}(\omega) \quad \text{for } \omega \geq 0 \quad \text{and} \\ &\quad 0 \quad \text{for } \omega < 0 . \end{aligned} \tag{12.9}$$

The negative part of the spectrum $\tilde{E}^-(\omega)$ is defined as

$$\begin{aligned} \tilde{E}^-(\omega) &= \tilde{E}(\omega) \quad \text{for} \quad \omega < 0 \quad \text{and} \\ &\quad 0 \quad \text{for} \quad \omega \geq 0 . \end{aligned} \tag{12.10}$$

Just as the replacement of real-valued sines and cosines by complex exponentials often simplifies Fourier analysis, so too does the use of complex-valued functions in place of the real electric field $E(t)$. For this purpose we separate the Fourier transform integral of $E(t)$ into two parts. The complex-valued temporal function $E^+(t)$ contains only the positive frequency segment of the spectrum. In communication theory and optics $E^+(t)$ is termed the analytic signal (its complex conjugate is $E^-(t)$ and contains the negative frequency part). By definition $E^+(t)$ and $\tilde{E}^+(\omega)$ as well as $E^-(t)$ and $\tilde{E}^-(\omega)$ are Fourier pairs where only the relations for the
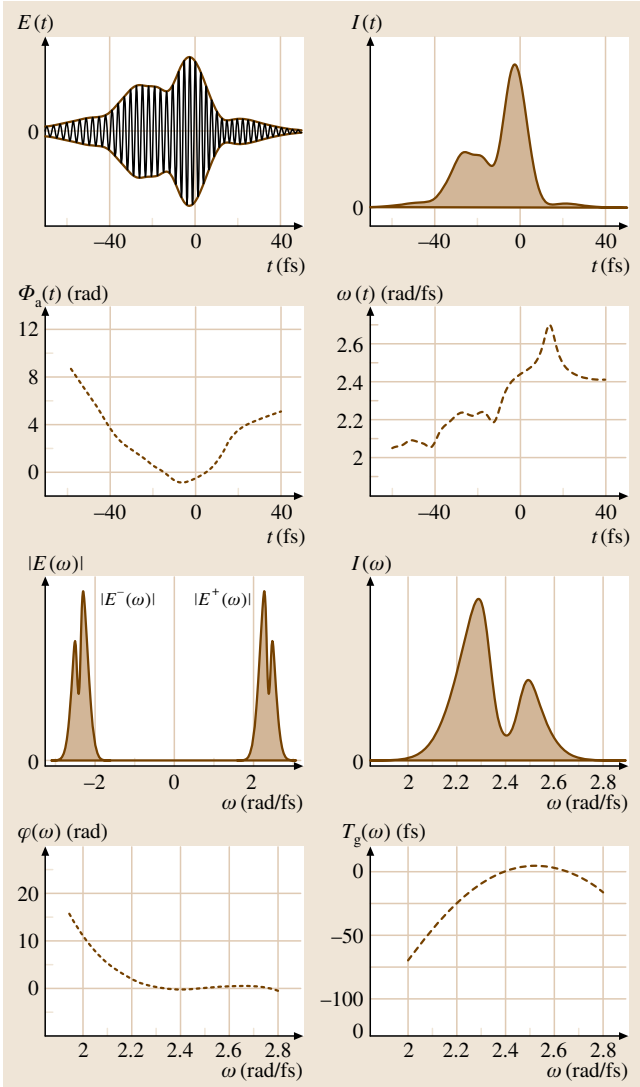
Fig. 12.2 Electric field $E(t)$, temporal intensity $I(t)$, additional temporal phase $\Phi_a(t)$, instantaneous frequency $\omega(t)$, spectrum $|\tilde{E}(\omega)|$, spectral intensity $I(\omega)$, spectral phase $\varphi(\omega)$ and group delay $T_g(\omega)$ of a pulse that looks complicated on first glance (having a relatively simple spectral phase $\varphi(\omega)$). When measured with a spectrometer the spectral intensity as a function of wavelength is usually obtained, and the corresponding transformation on the basis of $I(\lambda)\,d\lambda = I(\omega)\,d\omega$ yields $I(\lambda) = -I(\omega)2\pi c/\lambda^2$ where the minus sign indicates the change in the direction of the axis. To avoid phase jumps when the phase exceeds 2π, *phase unwrapping* is employed. That means adding or subtracting 2π to the phase at each discontinuity. When the intensity is close to zero, the phase is meaningless and usually the phase is not plotted in such regions (phase blanking)

positive-frequency part are given as

$$E^+(t) = \frac{1}{2\pi}\int_{-\infty}^{\infty} \tilde{E}^+(\omega)\,e^{i\omega t}\,d\omega \tag{12.11}$$

$$\tilde{E}^+(\omega) = \int_{-\infty}^{\infty} E^+(t)\,e^{-i\omega t}\,dt \ . \tag{12.12}$$

These quantities relate to the real electric field

$$\begin{aligned}
E(t) &= E^+(t) + E^-(t) \\
&= 2\,\mathrm{Re}\{E^+(t)\} \\
&= 2\,\mathrm{Re}\{E^-(t)\}
\end{aligned} \tag{12.13}$$

and its complex Fourier transform

$$\tilde{E}(\omega) = \tilde{E}^+(\omega) + \tilde{E}^-(\omega) \ . \tag{12.14}$$

$E^+(t)$ is complex-valued and can therefore be expressed uniquely in terms of its amplitude and phase

$$\begin{aligned}
E^+(t) &= |E^+(t)|\,e^{i\Phi(t)} \\
&= |E^+(t)|\,e^{i\Phi_0}\,e^{i\omega_0 t}\,e^{i\Phi_a(t)} \\
&= \sqrt{\frac{I(t)}{2\varepsilon_0 cn}}\,e^{i\Phi_0}\,e^{i\omega_0 t}\,e^{i\Phi_a(t)} \\
&= \frac{1}{2}A(t)\,e^{i\Phi_0}\,e^{i\omega_0 t}\,e^{i\Phi_a(t)} \\
&= E_c(t)\,e^{i\Phi_0}\,e^{i\omega_0 t}
\end{aligned} \tag{12.15}$$

where the meaning of $A(t)$, Φ_0, ω_0 and $\Phi_a(t)$ is the same as in Sect. 12.1.1 and $E_c(t)$ is the complex-valued envelope function without the absolute phase and without the rapidly oscillating carrier-frequency phase factor, a quantity often used in ultrafast optics. The envelope function $A(t)$ is given by

$$A(t) = 2|E^+(t)| = 2|E^-(t)| = 2\sqrt{E^+(t)E^-(t)} \tag{12.16}$$

and coincides with the less general expression in (12.1). The complex positive-frequency part $\tilde{E}^+(\omega)$ can be analogously decomposed into amplitude and phase

$$\begin{aligned}
\tilde{E}^+(\omega) &= |\tilde{E}^+(\omega)|\,e^{-i\phi(\omega)} \\
&= \sqrt{\frac{\pi}{\varepsilon_0 cn}I(\omega)}\,e^{-i\phi(\omega)} \ ,
\end{aligned} \tag{12.17}$$

where $|\tilde{E}^+(\omega)|$ is the spectral amplitude, $\phi(\omega)$ is the spectral phase and $I(\omega)$ is the spectral intensity proportional to the power spectrum density (PSD) – the familiar quantity measured with a spectrometer. From

Fig. 12.3a–o Examples for changing the temporal shape of a 800 nm 10 fs pulse via the frequency domain (except (**n**)). *Left*: temporal intensity $I(t)$ (*shaded*), additional temporal phase $\Phi_a(t)$ (*dotted*), instantaneous frequency $\omega(t)$ (*dashed*), *right*: spectral intensity $I(\omega)$ (*shaded*), spectral phase $\phi(\omega)$ (*dotted*) and group delay $T_g(\omega)$ (*dashed*) for a: (**a**) bandwidth-limited Gaussian laser pulse of 10 fs duration; (**b**) bandwidth-limited Gaussian laser pulse of 10 fs duration shifted in time to -20 fs due to a linear phase term in the spectral domain ($\phi' = -20$ fs); (**c**) symmetrical broadened Gaussian laser pulse due to $\phi'' = 200$ fs²; (**d**) third-order spectral phase ($\phi''' = 1000$ fs³) leading to a quadratic group delay. The central frequency of the pulse arrives first, while frequencies on either side arrive later. The corresponding differences in frequencies cause beats in the temporal intensity profile. Pulses with cubic spectral phase distortion have therefore oscillations after (or before) a main pulse depending on the sign of ϕ'''. The higher the side pulses, the less meaningful the FWHM pulse duration; (**e**) combined action of all spectral phase coefficients (**a**)–(**d**). Phase unwrapping and blanking is employed when appropriate ▶

(12.8) the relation $-\phi(\omega) = \phi(-\omega)$ is obtained. As will be shown in Sect. 12.1.3 it is precisely the manipulation of this spectral phase $\phi(\omega)$ in the experiment which – by virtue of the Fourier transformation (12.11) – creates changes in the real electric field strength $E(t)$ (12.13) without changing $I(\omega)$. If the spectral intensity $I(\omega)$ is manipulated as well, additional degrees of freedom are accessible for generating temporal pulse shapes at the expense of lower energy.

Note that the distinction between positive- and negative-frequency parts is made for mathematical correctness. In practice only real electric fields and positive frequencies are displayed. Moreover, as usually only the shape and not the absolute magnitude of the envelope functions in addition to the phase function are the quantities of interest, all the prefactors are commonly omitted.

The temporal phase $\Phi(t)$ (12.4) contains frequency-versus-time information, leading to the definition of the instantaneous frequency $\omega(t)$ (12.5). In a similar fashion $\phi(\omega)$ contains time-versus-frequency information and we can define the group delay $T_g(\omega)$, which describes the relative temporal delay of a given spectral component (Sect. 12.1.3)

$$T_g(\omega) = \frac{d\phi}{d\omega} \, . \tag{12.18}$$
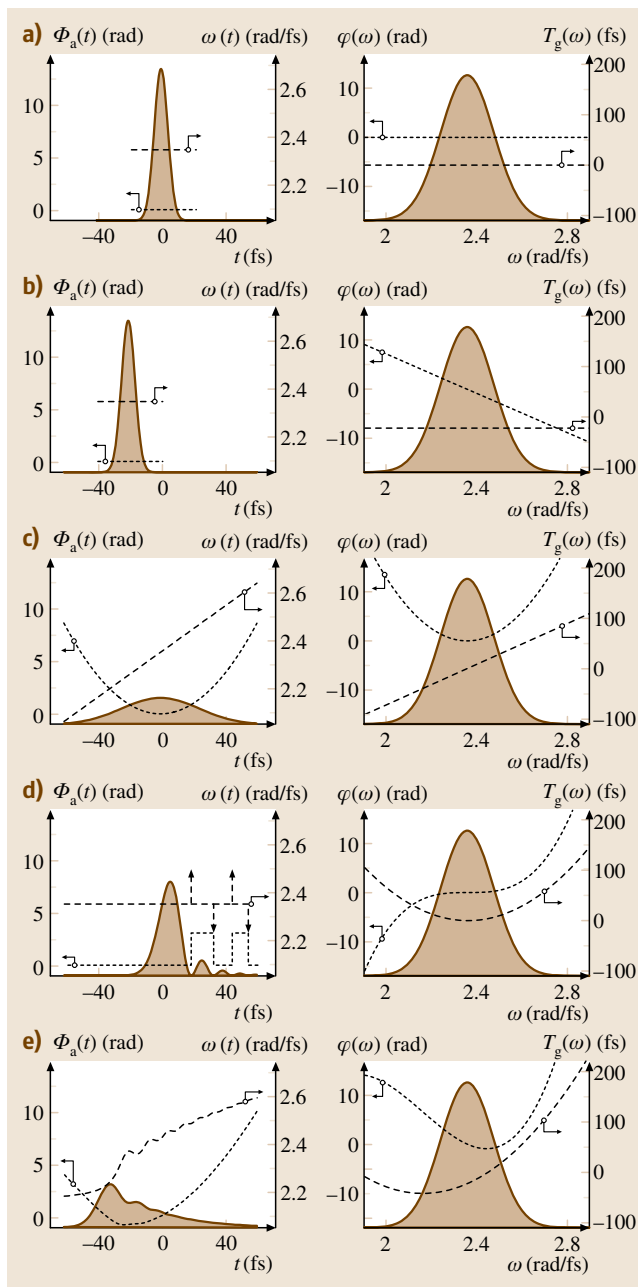
All quantities discussed so far are displayed in Fig. 12.2 for a pulse that initially appears to be complex. Usually the spectral amplitude is distributed around a center frequency (or carrier frequency) ω_0. Therefore – for *well-behaved* pulses – it is often helpful to expand the
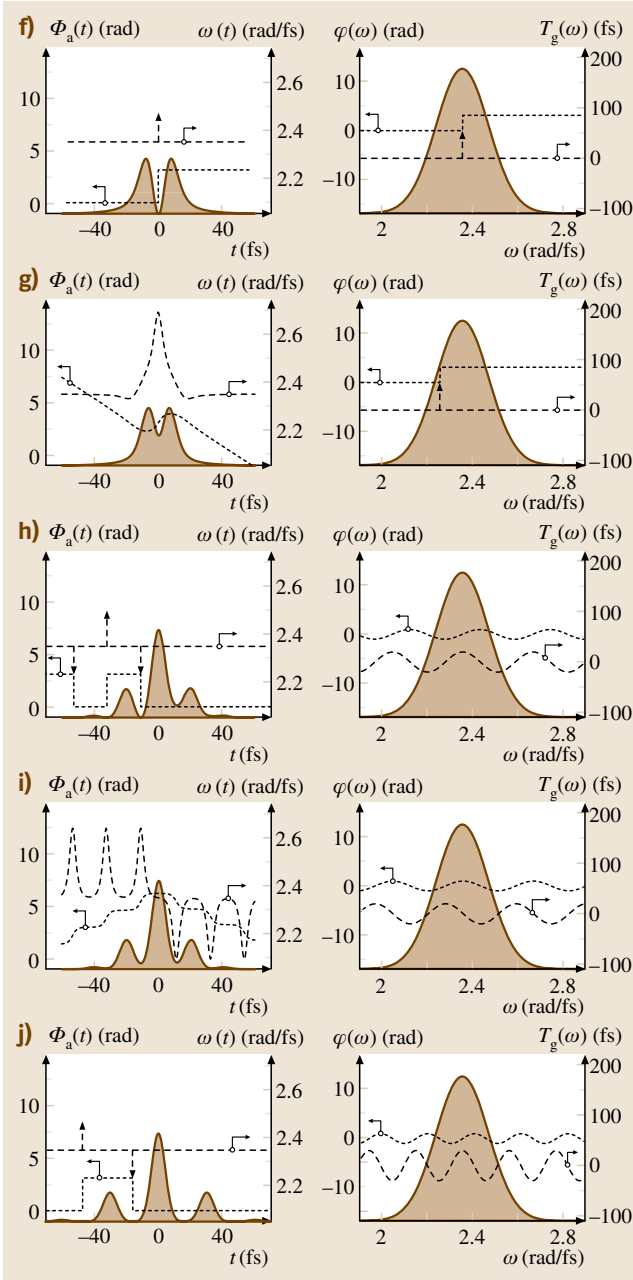
Fig. 12.3 (f) π step at the central frequency; **(g)** π step displaced from central frequency; **(h)** sine modulation at central frequency with $\phi(\omega) = 1\sin(20\,\text{fs}(\omega - \omega_0))$; **(i)** cosine modulation at central frequency with $\phi(\omega) = 1\cos(20\,\text{fs}(\omega - \omega_0))$; **(j)** sine modulation at central frequency with $\phi(\omega) = 1\sin(30\,\text{fs}(\omega - \omega_0))$

spectral phase into a Taylor series

$$\phi(\omega) = \sum_{j=0}^{\infty} \frac{\phi^{(j)}(\omega_0)}{j!} \cdot (\omega - \omega_0)^j$$

$$\text{with} \quad \phi^{(j)}(\omega_0) = \left.\frac{\partial^j \phi(\omega)}{\partial \omega^j}\right|_{\omega_0}$$

$$= \phi(\omega_0) + \phi'(\omega_0)(\omega - \omega_0)$$

$$+ \frac{1}{2}\phi''(\omega_0)(\omega - \omega_0)^2$$

$$+ \frac{1}{6}\phi'''(\omega_0)(\omega - \omega_0)^3 + \dots \quad (12.19)$$

The spectral phase coefficient of zeroth order describes in the time domain the absolute phase ($\Phi_0 = -\phi(\omega_0)$). The first-order term leads to a temporal translation of the envelope of the laser pulse in the time domain (the Fourier shift theorem) but not to a translation of the carrier. A positive $\phi'(\omega_0)$ corresponds to a shift towards later times. An experimental distinction between the temporal translation of the envelope via linear spectral phases in comparison to the temporal translation of the whole pulse is, for example, discussed in [12.20, 21]. The coefficients of higher order are responsible for changes in the temporal structure of the electric field. The minus sign in front of the spectral phase in (12.17) is chosen so that a positive $\phi''(\omega_0)$ corresponds to a linearly up-chirped laser pulse. For illustrations see Figs. 12.2 and 12.3a–e.

There is a variety of analytical pulse shapes where this formalism can be applied to get analytical expressions in both domains. For general pulse shapes a numerical implementation is helpful. For illustrations we will focus on a Gaussian laser pulse $E_{\text{in}}^+(t)$ (not normalized to pulse energy) with a corresponding spectrum $\tilde{E}_{\text{in}}^+(\omega)$. Phase modulation in the frequency domain leads to a spectrum $\tilde{E}_{\text{out}}^+(\omega)$ with a corresponding electric field $E_{\text{out}}^+(t)$ of

$$E_{\text{in}}^+(t) = \frac{E_0}{2} e^{-2\ln 2 \frac{t^2}{\Delta t^2}} e^{i\omega_0 t} . \quad (12.20)$$

Here Δt denotes the FWHM of the corresponding intensity $I(t)$. The absolute phase is set to zero, the carrier frequency is set to ω_0, additional phase terms are set to zero as well. The pulse is termed an unchirped pulse in the time domain. For $\tilde{E}_{\text{in}}^+(\omega)$ we obtain the spectrum

$$\tilde{E}_{\text{in}}^+(\omega) = \frac{E_0 \Delta t}{2} \sqrt{\frac{\pi}{2\ln 2}} e^{-\frac{\Delta t^2}{8\ln 2}(\omega - \omega_0)^2} . \quad (12.21)$$

The FWHM of the temporal intensity profile $I(t)$ and the spectral intensity profile $I(\omega)$ are related by $\Delta t \Delta \omega = 4 \ln 2$, where $\Delta \omega$ is the FWHM of the spectral intensity profile $I(\omega)$.

Usually this equation, known as the time–bandwidth product, is given in terms of frequencies ν rather than circular frequencies ω and we obtain

$$\Delta t \Delta \nu = \frac{2 \ln 2}{\pi} = 0.441 \ . \tag{12.22}$$

Several important consequences arise from this approach and are summarized before we proceed:

- The shorter the pulse duration, the larger the spectral width. A Gaussian pulse with $\Delta t = 10$ fs centered at 800 nm has a ratio of $\Delta \nu / \nu \approx 10\%$, corresponding to a wavelength interval $\Delta \lambda$ of about 100 nm. Taking into account the wings of the spectrum, a bandwidth comparable to the visible spectrum is *consumed* to create the 10 fs pulse.
- For a Gaussian pulse the equality in (12.22) is only reached when the instantaneous frequency (12.5) is time-independent, that is the temporal phase variation is linear. Such pulses are termed Fourier-transform-limited pulses or bandwidth-limited pulses.
- Adding nonlinear phase terms leads to the inequality $\Delta t \Delta \nu \geq 0.441$.
- For other pulse shapes a similar time-bandwidth inequality can be derived

$$\Delta t \Delta \nu \geq K \ . \tag{12.23}$$

Values of K for different pulse shapes are given in Table 12.1 and [12.22].

- Sometimes pulse durations and spectral widths defined by the FWHM values are not suitable measures. This is, for example, the case in pulses with substructure or broad wings causing a considerable part of the energy to lie outside the range given by the FWHM. In these cases one can use averaged values derived from the appropriate second-order moments [12.4, 23]. By this it can be shown [12.6, 24, 25] that, for any spectrum, the shortest pulse in time always occurs for a constant spectral phase $\phi(\omega)$. Taking a shift in the time domain also into account a description of a bandwidth-limited pulse is given by

$$\tilde{E}^+(\omega) = |\tilde{E}^+(\omega)| \mathrm{e}^{-\mathrm{i}\phi(\omega_0)} \mathrm{e}^{-\mathrm{i}\phi'(\omega_0)(\omega-\omega_0)} \ .$$
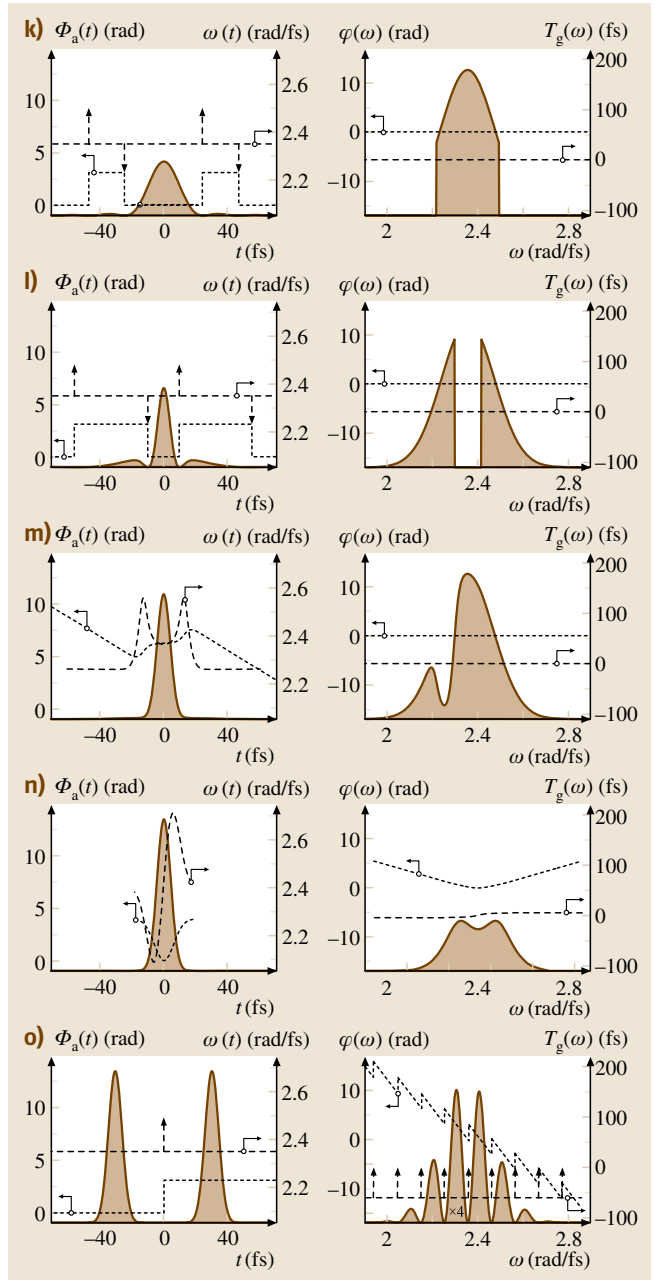
Fig. 12.3k–m Amplitude modulation: (**k**) symmetrical clipping of spectrum; (**l**) blocking of central frequency components; (**m**) off center absorption. (**n–o**) Modulation in time domain: (**n**) self-phase modulation. Note the spectral broadening; (**o**) double pulse with pulse to pulse delay of 60 fs

Part C | 12.1

Table 12.1 Temporal and spectral intensity profiles and time bandwidth products ($\Delta\nu\Delta t \geq K$) of various pulse shapes; $\Delta\nu$ and Δt are FWHM quantities of the corresponding intensity profiles. The ratio $\Delta t_{intAC}/\Delta t$, where Δt_{intAC} is the FWHM of the intensity autocorrelation with respect to background (Sect. 12.3.2), is also given. In the following formulas employed in the calculations we set $\omega_0 = 0$ for simplicity.

Gaussian:
$$E^+(t) = \frac{E_0}{2} e^{-2\ln 2\left(\frac{t}{\Delta t}\right)^2} \qquad\qquad \tilde{E}^+(\omega) = \frac{E_0\Delta t}{2}\sqrt{\frac{\pi}{2\ln 2}}\, e^{-\frac{\Delta t^2}{8\ln 2}\omega^2} ,$$

Sech:
$$E^+(t) = \frac{E_0}{2}\operatorname{sech}\left[2\ln\left(1+\sqrt{2}\right)\frac{t}{\Delta t}\right] \qquad\qquad \tilde{E}^+(\omega) = E_0\Delta t\frac{\pi}{4\ln\left(1+\sqrt{2}\right)}$$
$$\times\operatorname{sech}\left(\frac{\pi\Delta t}{4\ln\left(1+\sqrt{2}\right)}\omega\right) ,$$

Rect:
$$E^+(t) = \frac{E_0}{2} \quad t \in \left[-\frac{\Delta t}{2},\frac{\Delta t}{2}\right],\ 0\text{ elsewhere} \qquad \tilde{E}^+(\omega) = \frac{E_0\Delta t}{2}\operatorname{sinc}\left(\frac{\Delta t}{2}\omega\right) ,$$

Single sided Exp.:
$$E^+(t) = \frac{E_0}{2} e^{-\frac{\ln 2}{2}\frac{t}{\Delta t}} \quad t\in[0,\infty],\ 0\text{ elsewhere} \qquad \tilde{E}^+(\omega) = \frac{E_0\Delta t}{2i\Delta t\,\omega + \ln 2} ,$$

Symmetric Exp.:
$$E^+(t) = \frac{E_0}{2} e^{-\ln 2\frac{t}{\Delta t}} \qquad\qquad \tilde{E}^+(\omega) = \frac{E_0\Delta t\ln 2}{\Delta t^2\omega^2 + (\ln 2)^2} .$$

Shape	$I(t)$	$I(\omega)$	$\Delta\nu\cdot\Delta t$	$\Delta t_{intAC}/\Delta t$
Gaussian			0.441	1.414
Hyperbolic sechant			0.315	1.543
Square			0.886	1.000
Single sided exponential			0.110	2.000
Symmetric exponential			0.142	2.421

Table 12.2 Temporal broadening of a Gaussian laser pulse Δt_{out} in fs for various initial pulse durations Δt and various values of the second-order phase coefficient ϕ'', calculated with the help of (12.26). (The passage of a bandwidth-limited laser pulse at 800 nm through 1 cm of BK7 glass corresponds to $\phi'' = 440\,\text{fs}^2$. For the dispersion parameters of other materials see Table 12.3. Dispersion parameters of further optical elements are given in Sect. 12.1.3)

Δt(fs)	ϕ'' 100 fs^2	200 fs^2	500 fs^2	1000 fs^2	2000 fs^2	4000 fs^2	8000 fs^2
5	55.7	111.0	277.3	554.5	1109.0	2218.1	4436.1
10	29.5	56.3	139.0	277.4	554.6	1109.1	2218.1
20	24.3	34.2	72.1	140.1	278.0	554.9	1109.2
40	40.6	42.3	52.9	80.0	144.3	280.1	556.0
80	80.1	80.3	81.9	87.2	105.9	160.1	288.6
160	160.0	160.0	160.2	160.9	163.9	174.4	211.7

One feature of Gaussian laser pulses is that adding the quadratic term $\frac{1}{2}\phi''(\omega_0)(\omega - \omega_0)^2$ to the spectral phase function also leads to a quadratic term in the temporal phase function and therefore to linearly chirped pulses. This situation arises for example when passing an optical pulse through a transparent medium as will be shown in Sect. 12.1.3. The complex fields for such laser pulses are given by [12.26, 27]

$$\tilde{E}_{\text{out}}^+(\omega) = \frac{E_0 \Delta t}{2}$$
$$\times \sqrt{\frac{\pi}{2\ln 2}}\, e^{-\frac{\Delta t^2}{8\ln 2}(\omega - \omega_0)^2}\, e^{-i\frac{1}{2}\phi''(\omega_0)(\omega - \omega_0)^2}$$

$$(12.24)$$

$$E_{\text{out}}^+(t) = \frac{E_0}{2\gamma^{\frac{1}{4}}}\, e^{-\frac{t^2}{4\beta\gamma}}\, e^{i\omega_0 t}\, e^{i(at^2 - \varepsilon)} \qquad (12.25)$$

with

$$\beta = \frac{\Delta t_{\text{in}}^2}{8\ln 2}, \quad \gamma = 1 + \frac{\phi''^2}{4\beta^2}, \quad a = \frac{\phi''}{8\beta^2\gamma},$$

and

$$\varepsilon = \frac{1}{2}\arctan\left(\frac{\phi''}{2\beta}\right) = -\Phi_0.$$

For the pulse duration Δt_{out} (FWHM) of the linearly chirped pulse (quadratic temporal phase function at^2) we obtain the convenient formula

$$\Delta t_{\text{out}} = \sqrt{\Delta t^2 + \left(4\ln 2\frac{\phi''}{\Delta t}\right)^2}. \qquad (12.26)$$

The statistical definition of the pulse duration derived with the help of the second moment of the intensity distribution uses twice the standard deviation σ to characterize the pulse duration by

$$2\sigma = \frac{\Delta t_{\text{out}}}{\sqrt{2\ln 2}}, \qquad (12.27)$$

which is slightly shorter than the FWHM. These values are exact for Gaussian pulses considering only the ϕ'' part and can be used as a first estimate for temporal pulse broadening whenever ϕ'' effects are the dominant contribution (Sect. 12.1.3). Some values of the symmetric pulse broadening due to ϕ'' are given in Table 12.2 and exemplified in Fig. 12.3c.

Spectral phase coefficients of third order, i.e., a contribution to the phase function $\phi(\omega)$ of the form $\frac{1}{6}\phi'''(\omega_0)\cdot(\omega - \omega_0)^3$ are referred to as third-order dispersion (TOD). TOD applied to the spectrum given by (12.21) yields the phase-modulated spectrum

$$\tilde{E}_{\text{out}}^+(\omega) = \frac{E_0 \Delta t}{2}$$
$$\times \sqrt{\frac{\pi}{2\ln 2}}\, e^{-\frac{\Delta t^2}{8\ln 2}(\omega - \omega_0)^2}\, e^{-i\frac{1}{6}\phi'''(\omega_0)\cdot(\omega - \omega_0)^3}$$

$$(12.28)$$

and leads to asymmetric temporal pulse shapes [12.27] of the form

$$E_{\text{out}}^+(t) = \frac{E_0}{2}\sqrt{\frac{\pi}{2\ln 2}}\frac{\Delta t}{\tau_0}\text{Ai}\left(\frac{\tau - t}{\Delta\tau}\right)e^{\frac{\ln 2}{2}\cdot\frac{\frac{2}{3}\tau - t}{\tau_{1/2}}}e^{i\omega_0 t}$$

with $\tau_0 = \sqrt[3]{\frac{|\phi'''|}{2}} \quad \phi^3 = 2(\ln 2)^2\phi'''$

$$\Delta\tau = \tau_0\,\text{sign}(\phi''')$$

$$\tau = \frac{\Delta t^4}{16\phi^3} \quad \text{and} \quad \tau_{1/2} = \frac{\phi^3}{\Delta t^2} \qquad (12.29)$$

where Ai describes the Airy function. Equation (12.29) shows that the temporal pulse shape is given by the product of an exponential decay with a half-life period of $\tau_{1/2}$ and the Airy function shifted by τ and stretched by $\Delta\tau$. Figure 12.3d shows an example of a pulse subjected to TOD. The pulse shape is characterized by a strong initial pulse followed by a decaying pulse sequence. Because TOD leads to a quadratic group delay the central fre-

Table 12.3 Dispersion parameters n, $\mathrm{d}n/\mathrm{d}\lambda$, $\mathrm{d}^2n/\mathrm{d}\lambda^2$, $\mathrm{d}^3n/\mathrm{d}\lambda^3$, T_g, GDD and TOD for common optical materials for $L = 1\,\mathrm{mm}$. The data were calculated using Sellmeier's equation in the form $n^2(\lambda) - 1 = B_1\lambda^2/(\lambda^2 - C_1) + B_2\lambda^2/(\lambda^2 - C_2) + B_3\lambda^2/(\lambda^2 - C_3)$ and data from various sources (BK7, SF10 from *Schott – Optisches Glas* catalogue; sapphire and quartz from the *Melles Griot* catalogue)

Material	λ (nm)	$n(\lambda)$	$\frac{\mathrm{d}n}{\mathrm{d}\lambda} \cdot 10^{-2}$ (1/μm)	$\frac{\mathrm{d}^2 n}{\mathrm{d}\lambda^2} \cdot 10^{-1}$ (1/μm²)	$\frac{\mathrm{d}n^3}{\mathrm{d}\lambda^3}$ (1/μm³)	T_g (fs/mm)	GDD (fs²/mm)	TOD (fs³/mm)
BK7	400	1.5308	−13.17	10.66	−12.21	5282	120.79	40.57
	500	1.5214	−6.58	3.92	−3.46	5185	86.87	32.34
	600	1.5163	−3.91	1.77	−1.29	5136	67.52	29.70
	800	1.5108	−1.97	0.48	−0.29	5092	43.96	31.90
	1000	1.5075	−1.40	0.15	−0.09	5075	26.93	42.88
	1200	1.5049	−1.23	0.03	−0.04	5069	10.43	66.12
SF10	400	1.7783	−52.02	59.44	−101.56	6626	673.68	548.50
	500	1.7432	−20.89	15.55	−16.81	6163	344.19	219.81
	600	1.7267	−11.00	6.12	−4.98	5980	233.91	140.82
	800	1.7112	−4.55	1.58	−0.91	5830	143.38	97.26
	1000	1.7038	−2.62	0.56	−0.27	5771	99.42	92.79
	1200	1.6992	−1.88	0.22	−0.10	5743	68.59	107.51
Sapphire	400	1.7866	−17.20	13.55	−15.05	6189	153.62	47.03
	500	1.7743	−8.72	5.10	−4.42	6064	112.98	39.98
	600	1.7676	−5.23	2.32	−1.68	6001	88.65	37.97
	800	1.7602	−2.68	0.64	−0.38	5943	58.00	42.19
	1000	1.7557	−1.92	0.20	−0.12	5921	35.33	57.22
	1200	1.7522	−1.70	0.04	−0.05	5913	13.40	87.30
Quartz	300	1.4878	−30.04	34.31	−54.66	5263	164.06	46.49
	400	1.4701	−11.70	9.20	−10.17	5060	104.31	31.49
	500	1.4623	−5.93	3.48	−3.00	4977	77.04	26.88
	600	1.4580	−3.55	1.59	−1.14	4934	60.66	25.59
	800	1.4533	−1.80	0.44	−0.26	4896	40.00	28.43
	1000	1.4504	−1.27	0.14	−0.08	4880	24.71	38.73
	1200	1.4481	−1.12	0.03	−0.03	4875	9.76	60.05

quency of the pulse arrives first, while frequencies on either side arrive later. The corresponding differences in frequencies cause beats in the temporal intensity profile explaining the oscillations after (or before) the main pulse. The beating is also responsible for the phase jumps of π which occur at the zeros of the Airy function. Most of the relevant properties of TOD modulation are determined by the parameter $\Delta\tau$, which is proportional to $\sqrt[3]{|\phi'''|}$. The ratio $\Delta\tau/\Delta t$ determines whether the pulse is significantly modulated. If $|\Delta\tau/\Delta t| \geq 1$, a series of sub-pulses and phase jumps are observed. The sign of ϕ''' controls the time direction of the pulse shape: a positive value of ϕ''' leads to a series of post-pulses as shown in Fig. 12.3d whereas negative values of ϕ''' cause a series of prepulses. The time shift of the most intense sub-pulse with respect to the unmodulated pulse

and the FWHM of the sub-pulses are on the order of $\Delta\tau$. For these highly asymmetric pulses, the FWHM is not a meaningful quantity to characterize the pulse duration. Instead, the statistical definition of the pulse duration yields a formula similar to (12.26) and (12.27)

$$2\sigma = \sqrt{\frac{\Delta t^2}{2\ln 2} + 8(\ln 2)^2 \left(\frac{\phi'''}{\Delta t^2}\right)^2}. \tag{12.30}$$

It is a general feature of polynomial phase modulation functions that the statistical pulse duration of a modulated pulse is

$$2\sigma = \sqrt{\tau_1^2 + \tau_2^2}, \tag{12.31}$$

where $\tau_1 = \Delta t/\sqrt{2\ln 2}$ is the statistical duration of the unmodulated pulse [cf. (12.21)] and $\tau_2 \propto \phi^{(n)}/\Delta t^{n-1}$

a contribution only dependent on the nth-order spectral phase coefficient. As a consequence, for strongly modulated pulses, when $\tau_2 \gg \tau_1$, the statistical pulse duration increases approximately linearly with $\phi^{(n)}$.

It is not always advantageous to expand the phase function $\phi(\omega)$ into a Taylor series. Periodic phase functions, for example, are generally not well approximated by polynomial functions. For sinusoidal phase functions of the form $\phi(\omega) = A\sin(\omega\Upsilon + \varphi_0)$ analytic solutions for the temporal electric field can be found for any arbitrary unmodulated spectrum $\tilde{E}_{in}^{+}(\omega)$. To this end we consider the modulated spectrum (Sect. 12.1.3)

$$\tilde{E}_{out}^{+}(\omega) = \tilde{E}_{in}^{+}(\omega)\mathrm{e}^{-\mathrm{i}A\sin(\omega\Upsilon+\varphi_0)} , \tag{12.32}$$

where A describes the amplitude of the sinusoidal modulation, Υ the frequency of the modulation function (in units of time) and φ_0 the absolute phase of the sine function. Making use of the Jacobi–Anger identity

$$\mathrm{e}^{-A\sin(\omega\Upsilon+\varphi_0)} = \sum_{n=-\infty}^{\infty} J_n(A)\mathrm{e}^{-\mathrm{i}n(\omega\Upsilon+\varphi_0)} , \tag{12.33}$$

where $J_n(A)$ describes the Bessel function of the first kind and order n, we rewrite the phase modulation function

$$\tilde{M}(\omega) = \sum_{n=-\infty}^{\infty} J_n(A)\mathrm{e}^{-\mathrm{i}n(\omega\Upsilon+\varphi_0)} \tag{12.34}$$

to obtain its Fourier transform

$$M(t) = \sum_{n=-\infty}^{\infty} J_n(A)\mathrm{e}^{-\mathrm{i}n\varphi_0}\delta(n\Upsilon - t) , \tag{12.35}$$

where $\delta(t)$ describes the delta function. Since multiplication in the frequency domain corresponds to convolution in the time domain, the modulated temporal electrical field $E_{out}^{+}(t)$ is given by the convolution of the unmodulated field $E_{in}^{+}(t)$ with the Fourier transform of the modulation function $M(t)$, i.e., $E_{out}^{+}(t) = E_{in}^{+}(t) * M(t)$. Making use of (12.35) the modulated field reads

$$E_{out}^{+}(t) = \sum_{n=-\infty}^{\infty} J_n(A)E_{in}^{+}(t - n\Upsilon)\mathrm{e}^{-\mathrm{i}n\varphi_0} . \tag{12.36}$$

Equation (12.36) shows that sinusoidal phase modulation in the frequency domain produces a sequence of sub-pulses with a temporal separation determined by the parameter Υ and well-defined relative temporal phases controlled by the absolute phase φ_0. Provided the individual sub-pulses are temporally separated, i.e., Υ is chosen to exceed the pulse width, the envelope of each sub-pulse is a (scaled) replica of the unmodu-

lated pulse envelope. The amplitudes of the sub-pulses are given by $J_n(A)$ and can therefore be controlled by the modulation parameter A. Examples of sinusoidal phase modulation are shown in Fig. 12.3h–j. The influence of the absolute phase φ_0 is depicted in Fig. 12.3h and i, whereas Fig. 12.3j shows how separated pulses are obtained by changing the modulation frequency Υ. A detailed description of the effect of sinusoidal phase modulation can be found in [12.28].

12.1.3 Changing the Temporal Shape via the Frequency Domain

For the following discussion it is useful to think of an ultrashort pulse as being composed of groups of quasi-monochromatic waves, that is of a set of much longer wave packets of narrow spectrum all added together coherently. In vacuum the phase velocity $v_p = \omega/k$ and the group velocity $v_g = \mathrm{d}\omega/\mathrm{d}k$ are both constant and equal to the speed of light c, where k denotes the wave number. Therefore an ultrashort pulse – no matter how complicated its temporal electric field is – will maintain its shape upon propagation in vacuum. In the following we will always consider a bandwidth-limited pulse entering an optical system such as, for example, air, lenses, mirrors, prisms, gratings and combinations of these optical elements. Usually these optical systems will introduce dispersion, that is a different group velocity for each group of quasi-monochromatic waves, and consequently the initial short pulse will broaden in time. In this context the group delay $T_g(\omega)$ defined in (12.18) is the transit time for such a group of monochromatic waves through the system. As long as the intensities are kept low, no new frequencies are generated. This is the area of linear optics and the corresponding pulse propagation has been termed linear pulse propagation. It is convenient to describe the passage of an ultrashort pulse through a linear optical system by a complex optical transfer function [12.4, 25, 29]

$$\tilde{M}(\omega) = \tilde{R}(\omega)\mathrm{e}^{-\mathrm{i}\phi_d} , \tag{12.37}$$

that relates the incident electric field $\tilde{E}_{in}^{+}(\omega)$ to the output field

$$\tilde{E}_{out}^{+}(\omega) = \tilde{M}(\omega)\tilde{E}_{in}^{+}(\omega) = \tilde{R}(\omega)\mathrm{e}^{-\mathrm{i}\phi_d}\tilde{E}_{in}^{+}(\omega) , \tag{12.38}$$

where $\tilde{R}(\omega)$ is the real-valued spectral amplitude response describing for example the variable diffraction efficiency of a grating, linear gain or loss or direct amplitude manipulation. The phase $\phi_d(\omega)$ is termed the spectral phase transfer function. This is the phase ac-

cumulated by the spectral component of the pulse at frequency ω upon propagation between the input and output planes that define the optical system. It is this spectral phase transfer function that plays a crucial role in the design of ultrafast optical systems. Note that this approach is more involved when additional spatial coordinates have to be taken into account as, for example, in the case of *spatial chirp* (i. e., each frequency is displaced in the transverse spatial coordinates). Neglecting spatial chirp this approach can be taken as a first-order analysis of ultrafast optical systems. Although inside an optical system this condition might not be met, usually at the input and output all frequencies are assumed to be spatially overlapped for this kind of analysis. Note also that the independence of the different spectral components in this picture does not mean that the phase relations are random – they are uniquely defined with respect to each other. That means that the corresponding pulse in the time domain (by making use of (12.11) and (12.13)) is completely coherent [12.30] no matter how complicated the shape of the femtosecond laser pulse appears. In the first-order autocorrelation function a coherence time of the corresponding bandwidth-limited pulse would be observed. Only in the higher-order autocorrelations the uniquely defined phase relations show up (examples of second-order autocorrelations for phase- and amplitude-shaped laser pulses are given in Fig. 12.27). Figure 12.3f–j exemplifies the temporal intensity, spectral intensity and related phase functions for often employed phase functions. Figure 12.3k–m displays the same quantities for amplitude modulation. Figure 12.3n is an example for self-phase modulation and Fig. 12.3o shows a double pulse with pulse to pulse delay of 60 fs.

In the following discussion we will concentrate mainly on pure phase modulation and therefore set $\tilde{R}(\omega)$ constant for all frequencies and omit it initially. To model the system the most accurate approach is to include the whole spectral phase transfer function. Often however only the first orders of a Taylor expansion around the central frequency ω_0 are needed.

$$\phi_d(\omega) = \phi_d(\omega_0) + \phi_d'(\omega_0)(\omega - \omega_0)$$
$$+ \frac{1}{2}\phi_d''(\omega_0)(\omega - \omega_0)^2$$
$$+ \frac{1}{6}\phi_d'''(\omega_0)(\omega - \omega_0)^3 + \dots . \quad (12.39)$$

If we describe the incident bandwidth-limited pulse by $\tilde{E}_{in}^+(\omega) = |\tilde{E}^+(\omega)| e^{-i\phi(\omega_0)} e^{-i\phi'(\omega_0)(\omega-\omega_0)}$ then the over-

all phase ϕ_{op} of $\tilde{E}_{out}^+(\omega)$ is given by

$$\phi_{op}(\omega) = \phi(\omega_0) + \phi'(\omega_0)(\omega - \omega_0)$$
$$+ \phi_d(\omega_0) + \phi_d'(\omega_0)(\omega - \omega_0)$$
$$+ \frac{1}{2}\phi_d''(\omega_0)(\omega - \omega_0)^2$$
$$+ \frac{1}{6}\phi_d'''(\omega_0)(\omega - \omega_0)^3 + \dots \quad (12.40)$$

As discussed in the context of (12.19) the constant and linear terms do not lead to a change of the temporal envelope of the pulse. Therefore we will omit in the following these terms and concentrate mainly on the second-order dispersion ϕ'' (also termed the group velocity dispersion (GVD) or group delay dispersion (GDD)) and the third-order dispersion ϕ''' (TOD) whereas we have omitted the subscript d. Strictly they have units of fs^2/rad and fs^3/rad^2, respectively, but usually the units are simplified to fs^2 and fs^3.

A main topic in the design of ultrafast laser systems is the minimization of these higher dispersion terms with the help of suitably designed optical systems to keep the pulse duration inside a laser cavity or at the place of an experiment as short as possible. In the following we will discuss the elements that are commonly used for the *dispersion management*.

Dispersion Due to Transparent Media

A pulse traveling a distance L through a medium with index of refraction $n(\omega)$ accumulates the spectral phase

$$\phi_m(\omega) = k(\omega)L = \frac{\omega}{c}n(\omega)L , \quad (12.41)$$

which is the spectral transfer function due to propagation in the medium as defined above.

The first derivative

$$\frac{d\phi_m}{d\omega} = \phi_m' = \frac{d(kL)}{d\omega} = L\left(\frac{d\omega}{dk}\right)^{-1} = \frac{L}{v_g} = T_g \quad (12.42)$$

yields the group delay T_g and describes the delay of the peak of the envelope of the incident pulse. Usually the index of refraction $n(\omega)$ is given as a function of wavelength λ, i. e., $n(\lambda)$. Equation (12.42) then reads

$$T_g = \frac{d\phi_m}{d\omega} = \frac{L}{c}\left(n + \omega\frac{dn}{d\omega}\right) = \frac{L}{c}\left(n - \lambda\frac{dn}{d\lambda}\right) . \quad (12.43)$$

As different groups of the quasi-monochromatic waves move with different group velocities the pulse

will be broadened. For second-order dispersion we obtain the group delay dispersion (GDD)

$$\text{GDD} = \phi_m'' = \frac{d^2\phi_m}{d\omega^2} = \frac{L}{c}\left(2\frac{dn}{d\omega} + \omega\frac{d^2n}{d\omega^2}\right)$$
$$= \frac{\lambda^3 L}{2\pi c^2}\frac{d^2n}{d\lambda^2} . \tag{12.44}$$

For ordinary optical glasses in the visible range we encounter normal dispersion, i.e., red parts of the laser pulse will travel faster through the medium than blue parts. So the symmetric temporal broadening of the pulse due to ϕ'' will lead to a linearly up-chirped laser pulse as discussed in the context of (12.19) and Fig. 12.3c. In these cases the curvature of $n(\lambda)$ is positive (upward concavity) emphasizing the terminology that positive GDD leads to up-chirped pulses.

For the third-order dispersion (TOD) we obtain

$$\text{TOD} = \phi_m''' = \frac{d^3\phi_m}{d\omega^3} = \frac{L}{c}\left(3\frac{d^2n}{d\omega^2} + \omega\frac{d^3n}{d\omega^3}\right)$$
$$= \frac{-\lambda^4 L}{4\pi^2 c^3}\left(3\frac{d^2n}{d\lambda^2} + \lambda\frac{d^3n}{d\lambda^3}\right) . \tag{12.45}$$

Empirical formulas for $n(\lambda)$ such as Sellmeier's equations are usually tabulated for common optical materials so that all dispersion quantities in (12.43–12.45) can be calculated. Parameters for some optical materials are given in Table 12.3 for $L = 1$ mm.

Note that in fiber optics a slightly different terminology is used [12.25]. There the second-order dispersion is the dominant contribution to pulse broadening. The β parameter of a fiber is related to the second-order dispersion by

$$\beta = \frac{\left.\frac{d^2\phi_m}{d\omega^2}\right|_{\omega_0}}{L}\left[\frac{\text{ps}^2}{\text{km}}\right] , \tag{12.46}$$

where L denotes the length of the fiber. The dispersion parameter D is a measure for the group delay dispersion per unit bandwidth and is given by

$$D = \frac{\omega_0^2}{2\pi c}|\beta|\left[\frac{\text{ps}}{\text{nm km}}\right] . \tag{12.47}$$

Angular Dispersion

Transparent media in the optical domain possess positive group delay dispersion leading to up-chirped femtosecond pulses. To compress these pulses, optical systems are needed that deliver negative group delay dispersion, that is systems where the blue spectral components travel faster than the red spectral components.

Convenient devices for that purpose are based on angular dispersion delivered by prisms and gratings. We start our discussion again with the spectral transfer function [12.4]

$$\phi(\omega) = \frac{\omega}{c}P_{op}(\omega) , \tag{12.48}$$

where P_{op} denotes the optical path length. Equation (12.48) is the generalization of (12.41). The group delay dispersion is given by

$$\frac{d^2\phi}{d\omega^2} = \frac{1}{c}\left(2\frac{dP_{op}}{d\omega} + \omega\frac{d^2P_{op}}{d\omega^2}\right) = \frac{\lambda^3}{2\pi c^2}\frac{d^2P_{op}}{d\lambda^2} \tag{12.49}$$

and is similar to (12.44). In a dispersive system the optical path from an input reference plane to an output reference plane can be written

$$P_{op} = l\cos\alpha , \tag{12.50}$$

where $l = l(\omega_0)$ is the distance from the input plane to the output plane for the center frequency ω_0 and α is the angle of rays with frequency ω with respect to the ray corresponding to ω_0. In general, it can be shown [12.4] that the angular dispersion produces negative group delay dispersion

$$\frac{d^2\phi}{d\omega^2} \approx -\frac{l\omega_0}{c}\left(\left.\frac{d\alpha}{d\omega}\right|_{\omega_0}\right)^2 . \tag{12.51}$$
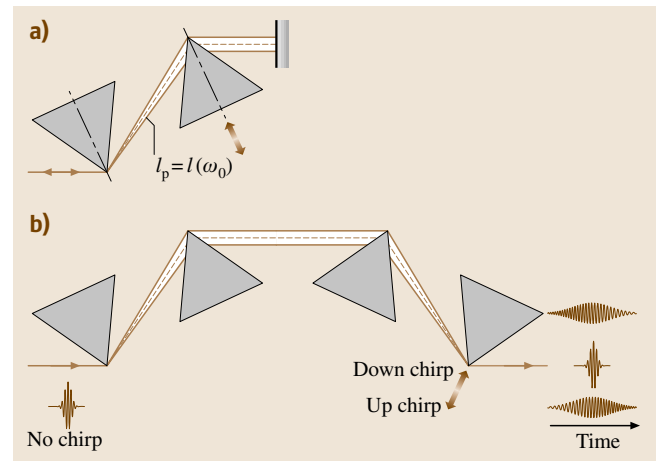
Fig. 12.3a,b Prism sequences for adjustable group delay dispersion. (**a**) Two-prism sequence in double-pass configuration (**b**) four-prism sequence. Note that the spatial distribution of the frequency (spatial chirp) after the second prism can be exploited for phase and/or amplitude manipulations

For pairs of elements (prisms or gratings) the first element provides the angular dispersion and the second element recollimates the spectral components (Fig. 12.3). Using two pairs of elements permits the lateral displacement of the spectral components (spatial chirp) to be canceled out and recovers the original beam profile.

Prism Sequences. Prism pairs [12.31] are well suited to introduce adjustable group delay dispersion (Fig. 12.3). Negative group delay dispersion is obtained via the angular dispersion of the first prism where the second prism is recollimating the beam. Recovering the original beam can be accomplished by either using a second pair of prisms or by using a mirror. Inside a laser cavity one can use either the four-prism arrangement or the two-prism arrangement for linear cavities together with a retroreflecting mirror. Outside a laser cavity the two-prism arrangement is often used, where the retroreflecting mirror is slightly off-axis to translate the recovered beam at the entrance of the system to be picked of by an additional mirror. There is also positive group delay dispersion in the system due to the material dispersion of the actual glass path the laser beam takes through the prism sequence. By translating one of the prisms along its axis of symmetry it is possible to change the amount of glass and therefore the amount of positive group delay dispersion. These devices allow a convenient continuous tuning of group delay dispersion from negative to positive values without beam deviation. The negative group delay dispersion via the angular dispersion can be calculated with the help of (12.48) and (12.50). In the case of minimum deviation and with the apex angle chosen so that the Brewster condition is satisfied (minimum reflection losses), the spectra phase introduced by a four-prism sequence $\phi_p(\omega)$ can be used to approximate the group delay dispersion by [12.4]

$$\frac{\mathrm{d}^2\phi_p}{\mathrm{d}\omega^2} \approx -\frac{4l_p\lambda^3}{\pi c^2}\left(\frac{\mathrm{d}n}{\mathrm{d}\lambda}\right)^2 \tag{12.52}$$

and the corresponding third-order dispersion yields approximately

$$\frac{\mathrm{d}^3\phi_p}{\mathrm{d}\omega^3} \approx \frac{6l_p\lambda^4}{\pi^2 c^3}\frac{\mathrm{d}n}{\mathrm{d}\lambda}\left(\frac{\mathrm{d}n}{\mathrm{d}\lambda}+\lambda\frac{\mathrm{d}^2n}{\mathrm{d}\lambda^2}\right). \tag{12.53}$$

In order to determine the total GDD and TOD of the four-prism sequence the corresponding contributions of the cumulative mean glass path L (12.44), (12.45) have to be added

$$\frac{\mathrm{d}^2\phi_{\mathrm{four-prism}}}{\mathrm{d}\omega^2} \approx \frac{\mathrm{d}^2\phi_m}{\mathrm{d}\omega^2} + \frac{\mathrm{d}^2\phi_p}{\mathrm{d}\omega^2}$$
$$= \frac{\lambda^3 L}{2\pi c^2}\frac{\mathrm{d}^2n}{\mathrm{d}\lambda^2} - \frac{4l_p\lambda^3}{\pi c^2}\left(\frac{\mathrm{d}n}{\mathrm{d}\lambda}\right)^2, \tag{12.54}$$

$$\frac{\mathrm{d}^3\phi_{\mathrm{four-prism}}}{\mathrm{d}\omega^3} \approx \frac{\mathrm{d}^3\phi_m}{\mathrm{d}\omega^3} + \frac{\mathrm{d}^3\phi_p}{\mathrm{d}\omega^3}$$
$$= \frac{-\lambda^4 L}{4\pi^2 c^3}\left(3\frac{\mathrm{d}^2n}{\mathrm{d}\lambda^2}+\lambda\frac{\mathrm{d}^3n}{\mathrm{d}\lambda^3}\right)$$
$$+ \frac{6l_p\lambda^4}{\pi^2 c^3}\frac{\mathrm{d}n}{\mathrm{d}\lambda}\left(\frac{\mathrm{d}n}{\mathrm{d}\lambda}+\lambda\frac{\mathrm{d}^2n}{\mathrm{d}\lambda^2}\right). \tag{12.55}$$

For a more-detailed discussion and other approaches to the derivation of the total GDD and TOD for a prism sequence see [12.31–35].

In principle one can get any amount of negative group velocity using this method. However a prism distance exceeding 1 m is often impractical. Higher amounts of positive group delay dispersion might be compensated for by the use of highly dispersive SF10 prisms but the higher third-order contribution prevent the generation of ultrashort pulses in the 10 fs regime. Fused quartz is a suitable material for ultrashort pulse generation with minimal higher-order dispersion. For example a four-prism sequence with $l_p = 50\,\mathrm{cm}$ of fused quartz used at 800 nm yields roughly $\mathrm{d}^2\phi_p/\mathrm{d}\omega^2 \approx -1000\,\mathrm{fs}^2$. Estimating a cumulative glass path of $L = 8\,\mathrm{mm}$ when going through the apexes of the prisms yields $\mathrm{d}^2\phi_m/\mathrm{d}\omega^2 \approx 300\,\mathrm{fs}^2$. In this way a maximum group delay dispersion of $+700\,\mathrm{fs}^2$ can be compensated.

Note that in such prism sequences the spatial distribution of the frequency components after the second prism can be exploited. Simple apertures can be used to tune the laser or to restrict the bandwidth. Appropriate phase or amplitude masks might be inserted as well.

Grating Arrangements. Diffraction gratings provide group delay dispersion in a similar manner to prisms. Suitable arrangements can introduce positive as well as negative group delay dispersion (see below). When introducing negative group delay dispersion the corresponding device is termed a *compressor*, while a device introducing positive group delay dispersion is termed a *stretcher*. Grating arrangements have the advantage of being much more dispersive but the disadvantage of introducing higher losses than prism arrangements.

As intracavity elements they are used, for example, in high-gain fiber lasers. Outside laser cavities gratings are widely used:

- To compensate for large amounts of dispersion in optical fibers.
- For ultrashort pulse amplification up to the petawatt regime with a technique called chirped pulse amplification (CPA) [12.36]: In order to avoid damage to the optics and to avoid nonlinear distortion of the spatial and temporal profile of the laser beam, ultrashort pulses (10 fs to 1 ps) are typically stretched in time by a factor of 10^3–10^4 prior to injection into the amplifier. After the amplification process the pulses have to be recompressed, compensating also for additional phase accumulated during the amplification process. The topic is reviewed in [12.37].
- For pulse-shaping applications (Sect. 12.1.3).
- In combination with prism compressors to compensate third-order dispersion terms in addition to the group delay dispersion [12.38]. This was the combination employed to establish the long standing world record of 6 fs with dye lasers in 1987 [12.39].

In Fig. 12.4 the reflection of a laser beam from a grating is displayed. The spectrum of an ultrashort laser pulse will be decomposed after reflection into the first order according to the grating equation

$$\sin(\gamma) + \sin(\theta) = \frac{\lambda}{d}, \tag{12.56}$$

where γ is the angle of incidence, θ is the angle of the reflected wavelength component and d^{-1} is the grating constant. Blazed diffraction gratings have maximum transmission efficiency when employed in the Littrow configuration, i.e., $\gamma = \theta(\lambda_0) =$ blaze angle. This has
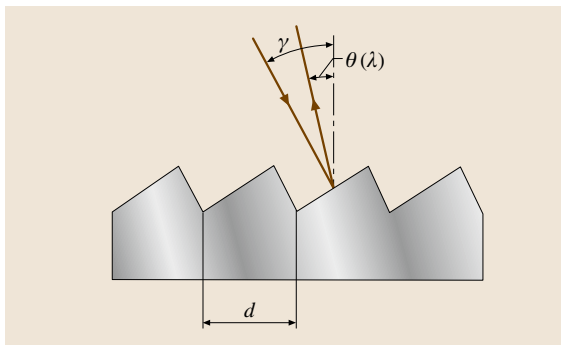
Fig. 12.4 Reflection from a grating: the spectrum of an ultrashort laser pulse will be decomposed after reflection (γ = angle of incidence, $\theta(\lambda)$ = angle of reflection, d^{-1} = grating constant)
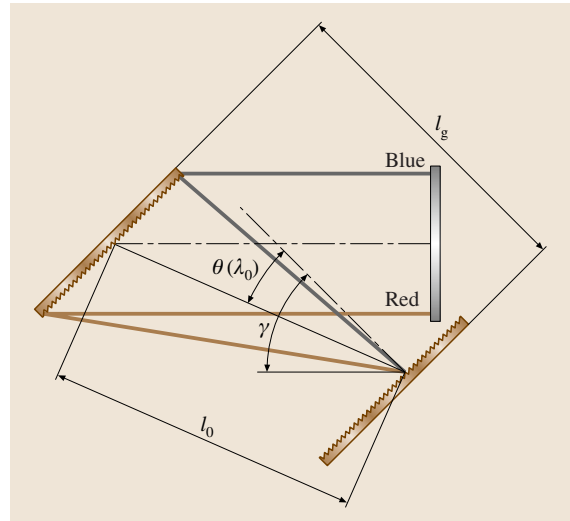

Fig. 12.5 Grating compressor with parallel gratings and a mirror for beam inversion (cf. the corresponding prism setup in Fig. 12.3a). The red spectral components travel a longer optical path than the blue spectral components (l_g denotes the distance between the grating; l_0 denotes the optical path for the center wavelength λ_0 between two gratings; both lengths are used by different authors in deriving the group delay dispersion and the third order dispersion)

the additional advantage that astigmatism is minimized. Blazed gold gratings with an efficiency of 90–95% are commercially available with a damage threshold of $> 250\,\text{mJ/cm}^2$ for a 1 ps pulse. For higher efficiency and higher damage threshold dielectric gratings have been developed, for example, dielectric gratings with 98% efficiency at 1053 nm and a damage threshold $> 500\,\text{mJ/cm}^2$ for fs pulses are available.

A basic grating compressor (Fig. 12.5) consists of two parallel gratings in a double-pass configuration [12.40]. The first grating decomposes the ultrashort laser pulse into its spectral components. The second grating is recollimating the beam. The original beam is recovered by use of a mirror that inverts the beam. As in such a device the red spectral components experience a longer optical path than the blue spectral components, such an arrangement is suitable to compensate for material dispersion.

In Fig. 12.6 different grating configurations are displayed that produce: (a) zero, (b) positive and (c) negative group delay dispersion. Between the gratings an additional telescope is employed.

In Fig. 12.6a, a so-called zero-dispersion compressor is depicted. The system consists of a telescope that
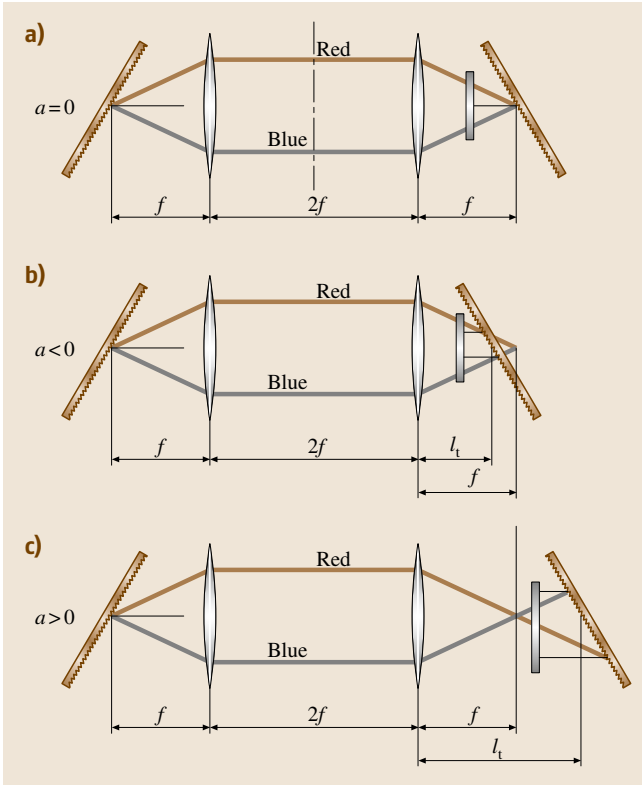
Fig. 12.6a–c Different grating configurations that produce (**a**) zero, (**b**) positive and (**c**) negative group delay dispersion. Arrangement (**a**) corresponds to a zero-dispersion compressor, (**b**) to a stretcher and (**c**) to a compressor. The zero-dispersion compressor is often used in pulse-shaping devices. The *dashed line* in (**a**) indicates the Fourier-transform plane, whereas the stretcher and compressor are key components for chirped pulse amplification

images the laser spot on the first grating onto the second grating. All wavelength components experience the same optical path. In this manner zero net dispersion is obtained. Due to the finite beam size on the grating the components belonging to the same wavelength emerge as a parallel beam and are focused with the lens of focal length f spectrally into the symmetry plane thus providing a Fourier transform plane for pulse shaping, masking or encoding (Sect. 12.1.3, Fig. 12.10).

Translating one of the gratings out of the focal plane closer to the telescope (Fig. 12.6b) results in an arrangement where the red components travel along a shorter optical path. The device introduces positive group delay dispersion (stretcher).

A compressor is realized by translating the grating away from the focal plane (Fig. 12.6c).

The dispersion can be further modified by the use of a magnifying telescope. In order to avoid material dispersion in the lenses and to minimize aberration effects, reflective telescopes and especially Öffner telescopes are usually employed [12.41, 42].

The phase transfer function ϕ_g for these arrangements can be calculated with the help of a matrix formalism [12.43] and considering the case of finite beam size [12.44].

For a reflective setup (neglecting material dispersion) the group delay dispersion and the third-order dispersion of the three telescope arrangements (magnification = 1) in Fig. 12.6 can be described using a characteristic length L

$$\frac{d^2\phi_g}{d\omega^2} = -\frac{\lambda^3}{\pi c^2 d^2} \frac{1}{\cos[\theta(\lambda)]^2} L \,, \tag{12.57}$$

$$\frac{d^3\phi_g}{d\omega^3} = \frac{d^2\phi_g}{d\omega^2} \frac{3\lambda}{2\pi c} \left(1 + \frac{\lambda}{d} \frac{\tan[\theta(\lambda)]}{\cos[\theta(\lambda)]}\right) . \tag{12.58}$$

With the help of the grating equation (12.56) $\cos[\theta(\lambda)]$ is given by:

$$\cos[\theta(\lambda)] = \sqrt{1 - \left(\frac{\lambda}{d} - \sin\gamma\right)^2} . \tag{12.59}$$

In reflective telescope setups usually only one grating is employed using suitable beam-folding arrangements. This reflects the situation when both gratings in Fig. 12.6 are moved out of the focal plane symmetrically. For the telescope arrangements we therefore obtain as the characteristic length $L = 2fa$. According to Fig. 12.6 the parameter a is determined by the distance of the grating to the lens

$$a = \frac{l_t}{f} - 1 \begin{cases} \text{Compressor: } l_t > f, \ a > 0 \\ \text{Zero-dispersion compressor: } l_t = f, \\ \qquad\qquad\qquad\qquad\qquad a = 0 \\ \text{Stretcher: } l_t < f, \ a < 0 \,. \end{cases}$$

$$\tag{12.60}$$

For the grating compressor depicted in Fig. 12.5 the characteristic length L is given by

$$L = l_0 = \frac{l_g}{\sqrt{1 - \left(\frac{\lambda}{d} - \sin(\gamma)\right)^2}} \,, \tag{12.61}$$

where l_0 is the optical path length of the center wavelength λ_0 between the gratings and l_g is the distance of the gratings.

For the compressor in Fig. 12.5 we obtain a group delay dispersion of $-1 \times 10^6 \, \text{fs}^2$ ($\lambda = 800 \, \text{nm}, d^{-1} =$

12001/mm, $l_0 = 300$ mm; $\gamma = 28, 6°$ (Littrow)) being orders of magnitude higher than the example given for the prism sequence.

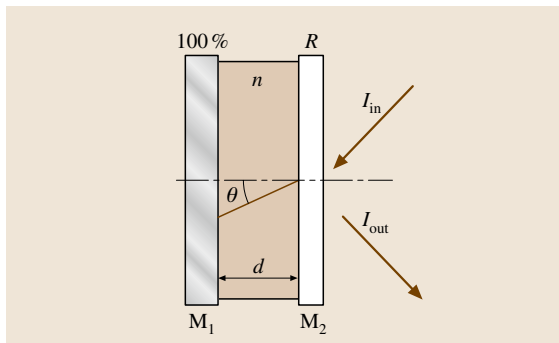### Dispersion Due to Interference (Gires–Tournois Interferometers and Chirped Mirrors)

The physics behind dispersion due to interference can be illustrated in the following way [12.25]. Periodic structures transmit or reflect waves of certain frequencies. Strong Bragg-type scattering usually occurs for wavelengths comparable to the periodicity of the struc-

Fig. 12.7 Schematic diagram of a Gires–Tournois interferometer (GTI)

ture. In this context the periodicity induces a resonance in the transfer function of the system, which then has dispersion associated with it.

A Gires–Tournois interferometer (GTI) [12.45] is a special case of a Fabry–Pérot interferometer in which one mirror (M1) is a 100% reflector and the top mirror (M2) is a low reflector, typically with a reflectivity of a few percent (Fig. 12.7). The group delay dispersion of such a device is given by (see for example [12.46] or [12.3] and references therein)

$$\frac{d^2\phi_{GTI}}{d\omega^2} = \frac{-2t_0^2(1-R)\sqrt{R}\sin\omega t_0}{(1+R-2\sqrt{R}\cos\omega t_0)^2} \; , \qquad (12.62)$$

where $t_0 = (2nd\cos\theta)/c$ is the round-trip time of the Fabry–Pérot [12.47], n is the refractive index of the material between the two layers, d is the thickness of the interferometer and θ is the internal angle of the beam between the layers. In this formula material dispersion is neglected and R is the intensity reflectivity of the top reflector. The group delay dispersion can be conveniently tuned either by tilting the device or by changing the interferometer spacing. Increasing t_0 increases the dispersion, but at the same time reduces the frequency range over which the group delay dispersion is constant. These devices are typically used in applications employing pulses larger than 100 fs. For picosecond pulses

Fig. 12.8a,b Schematic of different types of chirped mirrors: **(a)** simple chirped mirror; the wavelength-dependent penetration depth is depicted. For a proper design, for example, an incoming up-chirped laser pulse can be transformed into a bandwidth-limited pulse after reflection. **(b)** double chirped mirror; impedance matching by an additional antireflection coating on top of the mirror and by a duty-cycle modulation inside the mirror
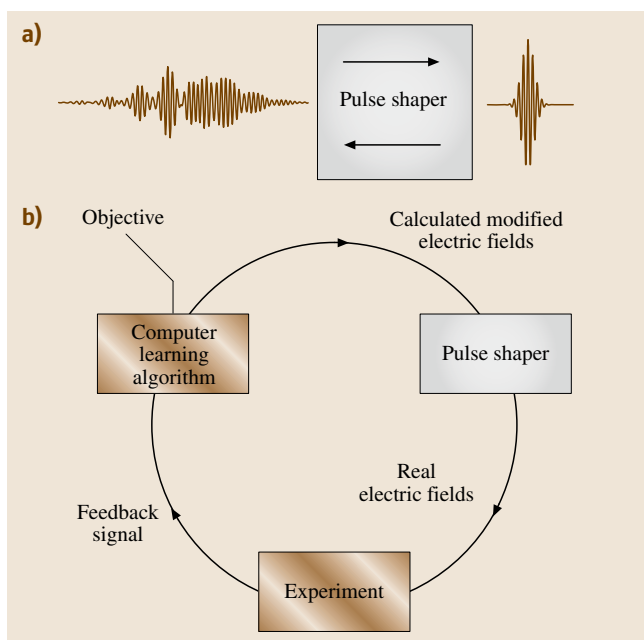
the mirror spacing is on the order of several mm, for femtosecond lasers the spacing has to be on the order of a few μm. In order to overcome the limitations for femtosecond applications, GTIs were constructed on the basis of dielectric multilayer systems [12.48]. The corresponding spectral transfer functions can be found in [12.4].

Nowadays specially designed dielectric multilayer mirrors offer a powerful alternative for dispersion management. Usually a dielectric mirror consists of alternating transparent pairs of high-index and low-index layers where the optical thickness of all layers is chosen to equal to 1/4 of the Bragg wavelength λ_B. Interference of the reflections at the index discontinuities add up constructively for the Bragg wavelength. If the opti-

Fig. 12.9 (a) Pulse-shaping issues (schematic): creation of bandwidth-limited pulses from complex-structured pulses (*left to right*). Creation of *tailored* pulse shapes (*right to left*). **(b)** Adaptive femtosecond pulse shaping: a femtosecond laser system (not indicated) and a computer-controlled pulse shaper are used to generate specific electric fields that are sent into an experiment. After deriving a suitable feedback signal from the experiment a learning algorithm calculates a modified electric fields based on the information from the experimental feedback signal and the user-defined control objective. The improved laser pulse shapes are tested and evaluated in the same manner. Cycling through this loop many times results in iteratively optimized laser pulse shapes that finally approach the objective

cal thickness of the layers along the mirror structure is varied, then the Bragg wavelength depends on the penetration depth. Figure 12.8 shows an example where the red wavelength components penetrate deeper into the mirror structure then the blue wavelength components. An up-chirped pulse impinging on the mirror surface can be transformed into a bandwidth-limited pulse after reflection from this mirror. A gradual increase of the Bragg wavelength along the mirror producing a negative group delay dispersion was demonstrated by [12.49] and the corresponding mirror was termed a chirped mirror, allowing for the construction of compact femtosecond oscillators [12.50]. Of course the Bragg wavelength does not have to be varied linearly with the penetration depth. In principle chirp laws $\lambda_B(z)$ can be found for compensation of higher-order dispersion in addition. It was realized, that the desired dispersion characteristics of the chirped mirrors can be spoiled by spurious effects originating from multiple reflections within the coating stack and at the interface to the ambient medium, leading to dispersion oscillations (see the discussion on GTI). An exact coupled-mode analysis [12.51] was used to develop a so-called double-chirp technique in combination with a broadband antireflection coating, in order to avoid the oscillations in the group delay dispersion. Using accurate analytical expressions double chirped mirrors could be designed and fabricated with a smooth and custom-tailored group delay dispersion [12.52] suitable for generating pulses in the two cycle regime directly from a Ti:sapphire laser [12.53]. Double chirping has the following meaning: in conventional chirped mirrors, equal optical lengths of high-index (hi) and low-index (lo) material within one period are employed, i. e., $P_{lo} = P_{hi} = \lambda_B/4$. Double chirping keeps the duty cycle η as an additional degree of freedom under the constraint: $P_{lo} + P_{hi} = (1-\eta)\lambda_B/2 + \eta\lambda_B/2 = \lambda_B/2$. Dispersion oscillations could further be suppressed by a back-side-coated double-mirror design [12.54].

Pulse Shaping

The methods for dispersion management described so far are well suited to compensate higher-order dispersion terms in linear optical setups such as group delay dispersion and third-order dispersion. Much greater flexibility in dispersion management and the possibility of creating complex-shaped laser pulses with respect to phase, amplitude and polarization state is given with the help of (computer-controlled) pulse-shaping techniques (Fig. 12.9a). The issue was recently reviewed by *Weiner* [12.29, 55].

A new class of experiments emerged in which pulse-shaping techniques were combined with some experimental signal embedded in a feedback learning loop [12.56–59]. In this approach a given pulse shape is evaluated in order to produce an improved pulse shape, which enhances the feedback signal (see Fig. 12.9b). These techniques have an impact on an increasing number of scientists in physics, chemistry, biology and engineering. This is due to the fact that primary light-induced processes can be studied and even actively controlled via adaptive femtosecond pulse shaping. For a small selection of work in various areas see [12.60–71].

Because of their short duration, femtosecond laser pulses cannot be directly shaped in the time domain. Therefore, the idea of pulse shaping is to modulate the incident spectral electric field $\tilde{E}_{\text{in}}^+(\omega)$ by a linear mask, i. e., the optical transfer function, $\tilde{M}(\omega)$ in the frequency domain. According to (12.38) this results in an outgoing shaped spectral electric field $\tilde{E}_{\text{out}}^+(\omega) = \tilde{M}(\omega)\tilde{E}_{\text{in}}^+(\omega) = \tilde{R}(\omega)\,e^{-i\phi_d}\tilde{E}_{\text{in}}^+(\omega)$. The mask may modulate the spectral amplitude response $\tilde{R}(\omega)$ and the spectral phase transfer function $\phi_d(\omega)$. Furthermore, polarization shaping has been demonstrated [12.72].

One way to realize a pulse shaper is the Fourier-transform pulse shaper. Its operation principle is based on optical Fourier transformations from the time domain into the frequency domain and vice versa. In Fig. 12.10 a standard design of such a pulse shaper is sketched. The incoming ultrashort laser pulse is dispersed by a grating and the spectral components are focused by a lens of focal length f. In the back focal plane of this lens – the Fourier plane – the spectral components of the original pulse are separated from each other, having minimum beam waists. By this means, the spectral components can be modulated individually by placing a linear mask into the Fourier plane. Afterwards, the laser pulse is reconstructed by performing an inverse Fourier transformation back into the time domain. Optically, this is realized by a mirrored setup consisting of an identical lens and grating. The whole setup – without the linear mask – is called a zero-dispersion compressor since it introduces no dispersion if the $4f$ condition is met (see also Fig. 12.6a). As a part of such a zero-dispersion compressor, the lenses separated by the distance $2f$, form a telescope with unitary magnification. Spectral modulations as stated by (12.38) can be set by inserting the linear mask.

Due to the damage threshold of the linear masks used, cylindrical focusing lenses (or mirrors) are normally used instead of spherical optics. The standard
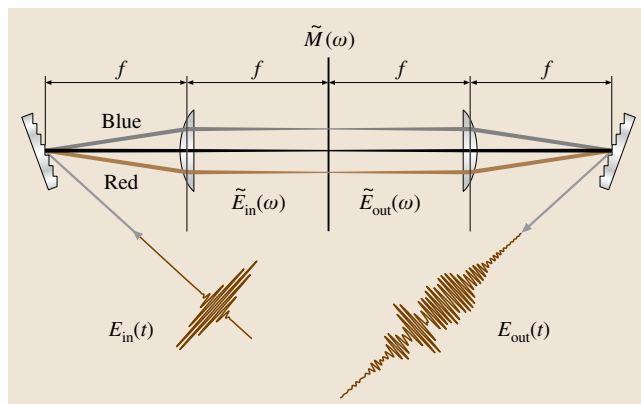

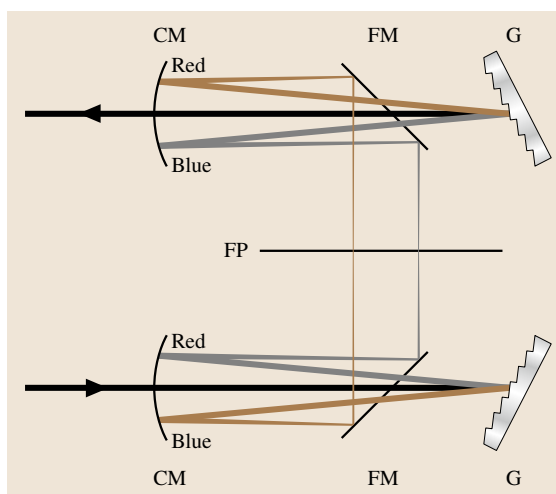**Fig. 12.10** Basic layout for Fourier-transform femtosecond pulse shaping

Fig. 12.11 Dispersion-optimized layout for Fourier transform femtosecond pulse shaping. The incoming beam is dispersed by the first grating (G). The spectral components go slightly out of plane and are sagitally focused by a cylindrical mirror (CM) via a plane-folding mirror (FM) in the Fourier plane (FP). Then the original beam is reconstructed by a mirrored setup

design in Fig. 12.10 has the advantage that all optical components are positioned along an optical line (grating in the Littrow configuration). For ultrashort pulses below 100 fs, however, spatial and temporal reconstruction errors become a problem due to the chromatic aberrations introduced by the lenses. Therefore, lenses are often replaced by curved mirrors. In general, optical errors are minimized if the tilting angles of the curved mirrors within the telescope are as small as possible.
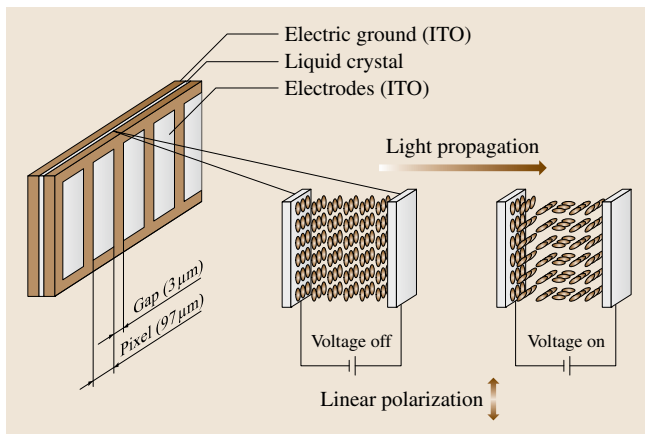
Fig. 12.12 Schematic diagram of an electronically addressed phase-only liquid-crystal spatial light modulator (LC-SLM). By adjusting the voltages of the individual pixels, the liquid-crystal molecules reorient themselves on average partially along the direction of the electric field. This leads to a change in refractive index and therefore to a phase modulation which can be independently controlled for different wavelength components

A folded, compact and dispersion optimized setup is depicted in Fig. 12.11 [12.73]. For ultrashort pulses in the < 10 fs regime prisms have been employed as dispersive elements instead of gratings [12.74].

A very popular linear mask for computer-controlled pulse shaping in such setups is the liquid-crystal spatial light modulator (LC-SLM). A schematic diagram of an electronically addressed phase-only LC-SLM is depicted in Fig. 12.12. In the Fourier plane the indi-
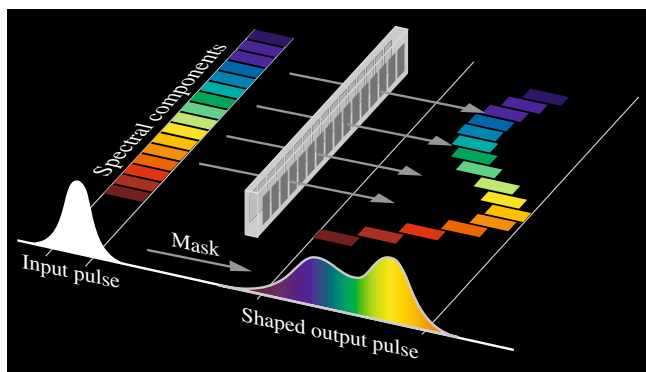
Fig. 12.13 Schematic illustration of shaping the temporal profile of an ultrashort laser pulse by retardation of the spectrally dispersed individual wavelength components in a phase only LC-SLM. The LC-SLM is located in the Fourier plane of the setups displayed in Figs. 12.10 and 12.11

vidual wavelength components of the laser pulse are spatially dispersed and can be conveniently manipulated by applying voltages at the separate pixels leading to changes of the refractive index. Upon transmission of the laser beam through the LC-SLM a frequency-dependent phase is acquired due to the individual pixel voltage values and consequently the individual wavelength components are retarded with respect to each other. Actual LC-SLMs contain up to 640 pixels [12.75]. In this way, an immensely large number of different spectrally phase modulated pulses can be produced. A phase-only LC-SLM does to a first approximation not change the spectral amplitudes and therefore the integrated pulse energy remains constant for different pulse shapes. By virtue of the Fourier transform properties, spectral phase changes result in phase- and amplitude-modulated laser pulse temporal profiles, as depicted schematically in Fig. 12.13.

If such an LC-SLM is oriented at 45° with respect to the linear polarization of the incident light field (either with the help of a wave plate or a suitably designed LC-SLM), polarization is induced in addition to retardance. A single LC-SLM together with a polarizer can be used therefore as an amplitude modulator. However, this also leads to phase modulation depending on the amplitude modulation level. For independent phase and amplitude control dual LC-SLMs are currently used. In such a setup a second LC-SLM is fixed back-to-back at −45° with respect to the linear polarization of light in front of the first LC-SLM and the stack is completed with a polarizer. For an early setup for independent phase and amplitude modulations see [12.76] whereas modern configurations are described in [12.55]. Alternatively, simple amplitude modulation functions $\tilde{R}(\omega)$ can be realized by insertion of absorbing material at specific locations in the Fourier plane, thus eliminating the corresponding spectral components within the pulse spectrum [12.77].

For polarization shaping [12.72] the polarizer is removed and spectral phase modulation can be imposed independently onto two orthogonal polarization directions. The interference of the resulting elliptically polarized spectral components leads to complex evolutions of the polarization state in the time domain. As any element between the LC-SLM stack and the experiment can modify the polarization evolution, dual-channel spectral interferometry and experimentally calibrated Jones matrix analysis have been employed for characterization [12.78]. A representation of a complex polarization shaped pulse is displayed in Fig. 12.14. Such pulses open up an immense range of applications,

Fig. 12.14a,b Electric field representation for a polarization-modulated laser pulse. Time evolves from *left* to *right*, and electric field amplitudes are indicated by the sizes of the corresponding ellipses. The momentary frequency can be indicated by *colors*, and the *shadows* represent the amplitude envelopes of the orthogonal electric field components. (**a**) A Gaussian-shaped laser spectrum supporting 80 fs laser pulses is taken for an illustrative theoretical example. (**b**) A complex experimentally realized polarization modulated laser pulse is shown. The width of the temporal window is 7.5 ps. (After [12.78])▶

especially in quantum control, because vectorial properties of multiphoton transitions can be addressed [12.79, 80].

Another possibility to realize phase-only pulse shaping is based on deformable mirrors consisting of a small number (∼10) of electrostatically controlled membrane mirrors [12.81]. These devices are placed in the Fourier plane and by a slight out-of-plane tilt upon reflection half of the optics can be saved (Fig. 12.15 for an illustration). The use of a micro-mirror array with 240×200 pixels used in reflection and a waveform update rate larger than 1 kHz has also been demonstrated [12.82].

Acoustooptic modulators (AOMs) can be used for programmable pulse shaping as well. Two different approaches exist.

One approach is depicted in Fig. 12.16 and is reviewed in [12.83, 84]. The AOM crystal is oriented at the Bragg angle to the Fourier plane of a zero-dispersion compressor. In the visible TeO_2 crystals are normally used whereas in the infrared InP crystals are employed. A programmable radio-frequency (RF) signal driving the piezoelectric transducer of the AOM creates an acoustic wave that propagates through the crystal. As light travels at orders of magnitude faster velocity, the acoustic wave can be considered as a fixed modulated grating at the moment the spatially dispersed laser beam hits the crystal. The amplitude and phase of the acoustic wave determine the diffraction efficiency and phase shift at each point in space. The beam is diffracted typically below 1° by the AOM via the photoelastic effect. AOMs can place in the order of thousand independent features onto the spectrum and have a significantly faster update rate than an LC-SLMs. On the other hand the optical throughput of such devices is well below 50% and typical mode-locked laser sources running at 100 MHz repetition rate in general cannot be pulse shaped because the acoustic wave is traveling several tens of microns
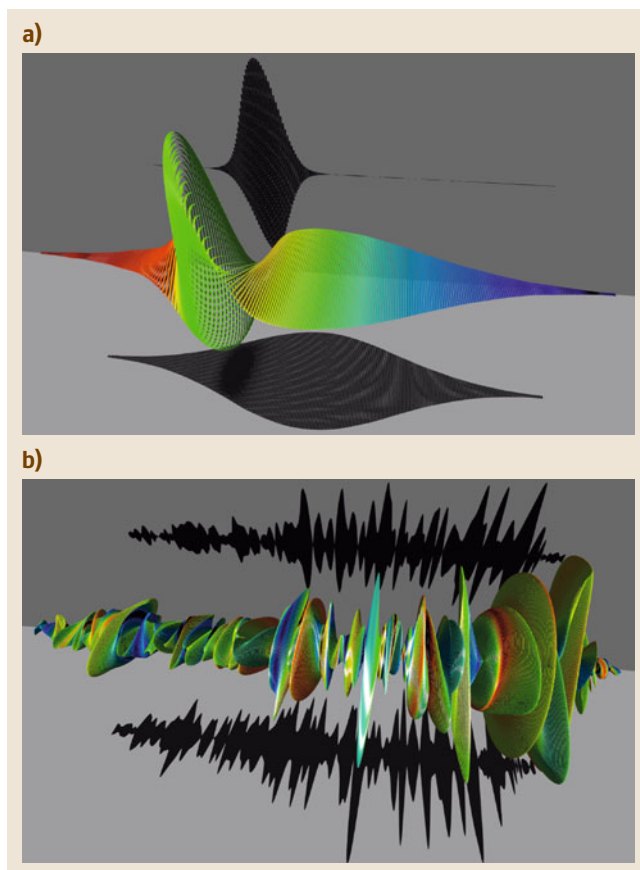
in 10 ns. This is not a limitation for amplified ultrafast laser systems where the pulse repetition rate is usually slower than the acoustic aperture time, since this allows the acoustic pattern to be synchronized to each amplifier pulse and to be refreshed before the next pulse arrives.
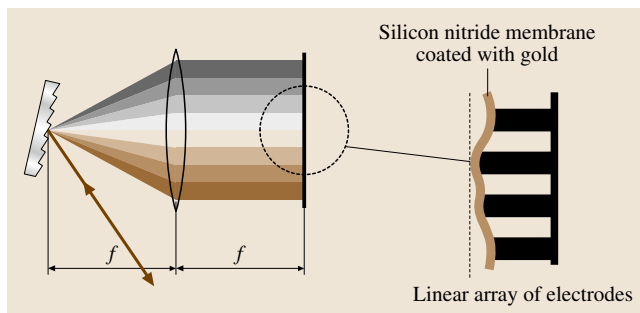
Fig. 12.15 Schematic of a phase-only deformable-mirror pulse shaper
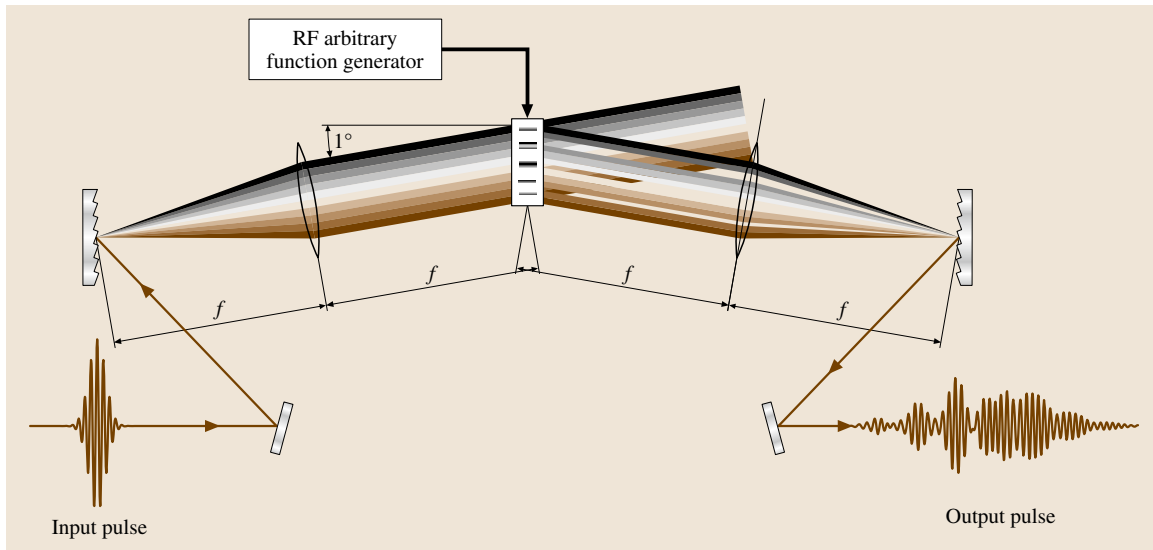
Fig. 12.16 Programmable pulse-shaping device based on the use of an acoustooptic modulator as the spatial light modulator
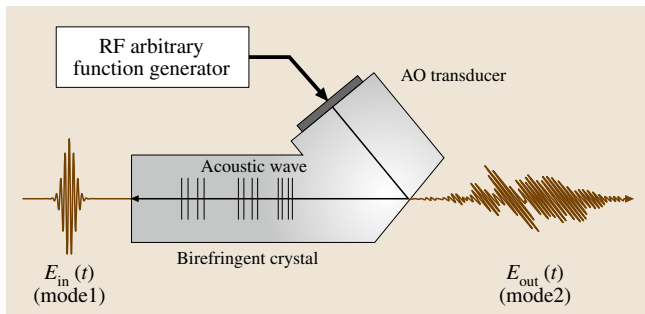
Fig. 12.17 Schematic of an acoustooptic programmable dispersive filter (AOPDF)

The other AOM approach is based on an acoustooptic programmable dispersive filter (AOPDF) and does not need to be placed in the Fourier plane of a $4f$ device [12.85–87]. A schematic of this device is shown in Fig. 12.17. Again, a programmable signal driving the piezoelectric transducer of the AOM creates an acoustic wave that propagates through the crystal and reproduces spatially the temporal shape of the RF signal. Two optical modes can be coupled efficiently by acoustooptic interaction only in the case of phase matching. If there is locally only one spatial frequency in the acoustic grating, then only one optical frequency can be diffracted at that position from the fast ordinary axis (mode 1) to the slow extraordinary axis (mode 2). The incident optical short pulse is initially in mode 1. Different groups of optical frequency components travel a different distance before they encounter phase-matched spatial frequencies in the acoustic grating. At that position part of the energy is diffracted onto mode 2. The pulse leaving the device at mode 2 will be made of all spectral components that have been diffracted at the various positions. If the velocities of the two modes are different, each frequency will see a different time delay. The amplitude of specific frequency components of the output pulse is controlled by the acoustic power at the position where that frequency components are diffracted. With the help of a 2.5 cm long TeO_2 crystal, a group delay range of 3 ps, 6.7 fs temporal resolution and 30% diffraction efficiency has been reported [12.86]. In general pulse shapers based on LC-SLMs or deformable mirrors have low transmission losses, are suitable also for high-repetition-rate mode-locked laser oscillators, do not impose additional chirp and have a low waveform update rate on the order of 10 Hz. Setups based on AOMs have high transmission losses and impose additional chirp, but they have a waveform update rate on the order of 100 kHz. Both AOMs and LC-SLMs can impose on the order of 1000 independent features onto the spectrum and are both suitable for amplitude and phase modulation. Programmable polarization shaping has been demonstrated so far only with LC-SLMs.

The programmable femtosecond pulse-shaping techniques described so far allow control of the temporal profile of an output waveform in phase, amplitude

and polarization. This can be thought of as control over one spatial dimension, the direction of propagation. With that respect this *temporal-only* pulse shaping is one dimensional. Automated two-dimensional phase-only pulse shaping employing an optically addressed reflective two-dimensional SLM with negligible interpixel gaps allows real-space pulse shaping, in which a sample or device is irradiated with different tempo-

rally shaped waveforms at different locations [12.88]. The pulse-shaping arrangement is similar to conventional $4f$ spectral filtering arrangements, with the difference that the incoming beam is expanded in one dimension and the two-dimensional SLM is employed in a reflection geometry. Such a unit has been employed for two-dimensional shaping of surface polaritons [12.89].

12.2 Generation of Femtosecond Laser Pulses via Mode Locking

Femtosecond laser pulses can be generated directly from a wide variety of lasers with wavelengths ranging from the ultraviolet to the infrared. This range is greatly extended by the use of nonlinear frequency-conversion techniques. Continuous tuning is achieved, for example, via optical parametric oscillators followed by (cascaded) sum- and difference-frequency mixing. Tuning of amplified femtosecond laser systems is achieved via optical parametric amplifiers. The generation of a white-light continuum is also a standard technique for the generation of new wavelengths. With high-power femtosecond laser systems the x-ray region can be reached by focusing the radiation into a solid-state material or via high-harmonic generation whereas the latter technique also opens the door to the attosecond regime. The THz spectral region can be accessed via femtosecond lasers as well.

   With very few exceptions the generation of ultrashort pulses relies on a technique known as mode locking. The topic has been covered in review articles [12.46, 90–93], in several books devoted to ultrashort laser pulses [12.2–5, 94] and in general laser text books [12.47, 95–97]. For a recent compilation of mode locking different laser systems ranging from solid-state lasers through fiber lasers to semiconductor lasers see, for example, [12.98].

   Here we will limit the description to the basic concepts of mode locking.

   A laser is typically constructed with a pair of mirrors separated by a distance L which enclose a gain medium and other components. In a continuous-wave (CW) laser or in a pulsed laser where the pulse duration is substantially greater then the cavity round-trip time T_{RT}

$$T_{RT} = \frac{2L}{c} \qquad (12.63)$$

(c is the velocity of light and for simplicity the refractive index is taken as unity) the radiation energy is spread
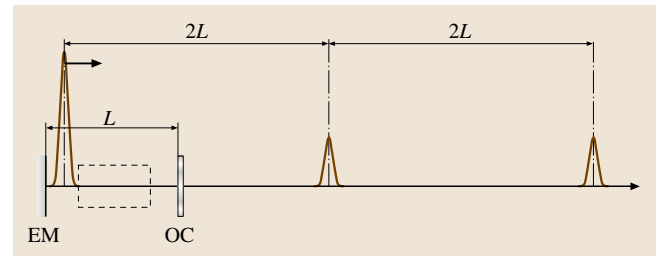
Fig. 12.18 Simple snapshot representation of a mode-locked laser. The pulse is propagating back and forth between the end mirror (EM) and the output coupler (OC). The pulses in the output beam are separated by $2L$ in space (or $2L/c = T_{RT}$ in time). The *dashed box* represents the gain medium and other laser components

out fairly uniform between the mirrors. The generation of ultrashort laser pulses is based on the confinement of the energy in the cavity into a small spatial region. This single pulse bounces back and forth between the mirrors at the velocity of light. As indicated in Fig. 12.18 the output beam arises from partial transmission of the intracavity pulse through the output coupler and therefore consists of a train of replicas of the cavity pulse separated by $2L$ in space or by T_{RT} in time. A laser operating in this fashion is said to be mode locked for reasons that will become apparent soon.

   In order to understand the physics behind mode locking a more precise discussion is necessary. Generally two conditions govern the frequency spectrum of a laser. On the one hand the overall envelope of the spectrum is determined by the emission profile of the lasing medium and by the characteristics of any wavelength selective element within the cavity. On the other hand for each transverse mode the cavity allows oscillations only at discrete frequencies ν_n the so-called *longitudinal* modes. Usually only one *transverse* mode namely the lowest-order mode having a Gaussian profile is permitted to oscillate in mode-locked laser systems. The corresponding set of longitudinal modes consists of
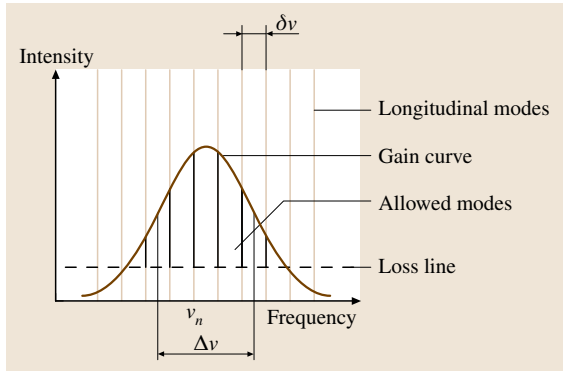
Fig. 12.19 Longitudinal modes in a laser cavity. The spacing δv of the modes is determined by the cavity length via $\delta v = c/2L = 1/T_{RT}$. Only those modes exceeding the loss line will lase. The FWHM of the spectral intensity function δv is also indicated in addition. In lasers used for pulse generation below 10 fs the number of modes lasing is of the order 10^6

a picket fence of regularly spaced modes – also termed the frequency comb – being separated by a frequency of δv

$$\delta v = v_{n+1} - v_n = \frac{c}{2L} = \frac{1}{T_{RT}} . \qquad (12.64)$$

Taking both conditions together the emission spectrum of the laser will consist of those modes which have sufficient gain to lie above the threshold for lasing. The corresponding relationships are depicted in Fig. 12.19. The total electric field $E(t)$ resulting from such a multi-mode oscillation at a fixed point in space, say at one of the mirrors, is given by

$$E(t) = \sum_{n=0}^{N-1} E_n \sin[2\pi(v_0 + n\delta v)t + \varphi_n(t)] , \qquad (12.65)$$

where N is the number of oscillating modes, $\varphi_n(t)$ is the phase of the nth mode and v_0 is the lowest-frequency mode above the lasing threshold.

The average laser power output $P(t)$ is proportional to the square of the total electric field. Unless some method of fixing the relative phases $\varphi_n(t)$ of the modes is used they will generally vary randomly in time. This produces a random variation of the average laser power output $P(t)$ as a result of the random interference between modes.

If the phases are fixed with respect to each other $(\varphi_n(t) \rightarrow \varphi_n)$, it can be shown that $E(t)$ and accordingly $P(t)$ repeats with the period T_{RT}. In the case that the
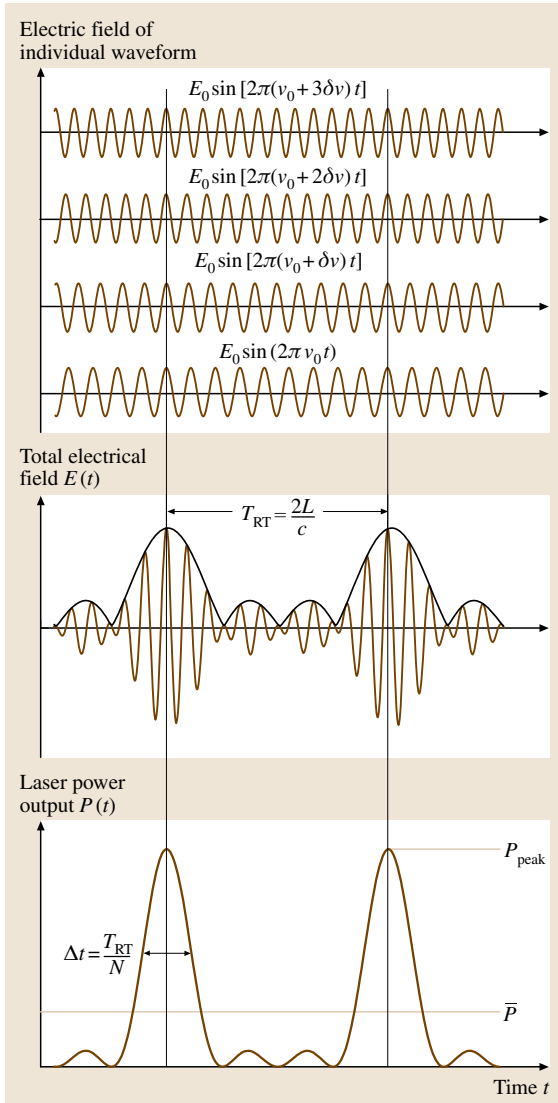
Fig. 12.20 Superposition of four sine waves with equal amplitude E_0, differing in frequency by δv. The electric field of the individual waveforms, the total electric field $E(t)$, its envelope and the output power $P(t)$ as well as the average power $\bar{P}$ are shown

individual φ_n are randomly fixed, each *noise spike* in the random but periodic laser output power has a duration Δt roughly equal to $1/\Delta v$ with Δv being the FWHM of the spectral intensity function (Fig. 12.22e,f). Within this approach the properties of perfectly mode-locked lasers are determined by a linear phase relation $\varphi_n = n\alpha$ amongst the modes, that is, a constant phase re-

lation between two adjacent modes. This is the so-called mode-locking condition. To simplify the analysis of this case identical amplitudes $E_n = E_0$ for all modes are assumed corresponding to a square gain profile and for convenience α is set to zero. The summation of (12.65) then yields

$$E(t) = E_0 \sin\left[2\pi\left(\nu_0 + \frac{N-1}{2}\delta\nu\right)t\right]\frac{\sin(N\pi\delta\nu t)}{\sin(\pi\delta\nu t)} .$$

(12.66)

The resulting electric field consists of a rapid oscillating part at the light central frequency $\nu_c = \nu_0 + N - 1/2\delta\nu$ with the envelope $\left|\sin(N\pi\delta\nu t)/\sin(\pi\delta\nu t)\right|$ oscillating with $\delta\nu = 1/T_{RT}$. Averaging the fast oscillation ν_c the output power $P(t)$ is given by

$$P(t) = P_0\left(\frac{\sin(N\pi\delta\nu t)}{\sin(\pi\delta\nu t)}\right)^2 ,$$

(12.67)

where P_0 is the average power of one wave.

A discussion of this equation yields important insight into the properties of laser pulses generated via mode locking:

1. The power is emitted in the form of a train of pulses with a period corresponding to the cavity round-trip time $T_{RT} = 1/\delta\nu$.
2. The peak power P_{Peak} increases quadratically with the number N of modes locked together: $P_{Peak} = N^2 P_0$. Mode locking is therefore useful to produce high peak powers and by focusing the laser beam to create high peak intensities; the average power $\bar{P}$ of both a mode-locked and a non-mode-locked laser is given by $\bar{P} = NP_0$.
3. The FWHM pulse duration Δt decreases linearly with the number N of modes locked together or equivalent is approximately the inverse of the gain bandwidth $\Delta\nu$:

$$\Delta t \approx \frac{T_{RT}}{N} = \frac{1}{N\delta\nu} = \frac{1}{\Delta\nu} .$$

This is why in the past dye lasers and nowadays solid-state lasers with large gain bandwidths are used to create femtosecond pulses. Ultrafast dye-laser generated pulses as short as 27 fs with around 10 mW of average power [12.99], whereas pulses around 5–6 fs with around 100 mW average power can be produced with Ti:sapphire lasers [12.53, 100]. In general the minimum pulse duration for a given gain profile can be estimated via the bandwidth product introduced in Sect. 12.1.2 and is summarized for various line shapes in Table 12.1.
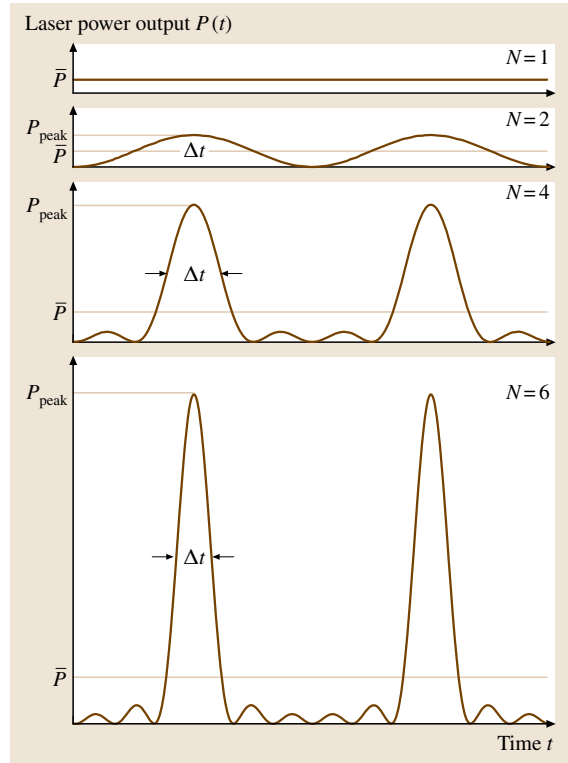

Fig. 12.21 Comparison of the one-, two-, four- and six-mode cases. An increase in the number of modes leads to a decrease in pulse duration. The peak power P_{peak} increases quadratically with the number N of modes locked together, whereas the average power $\bar{P}$ of both a mode-locked and a non-mode-locked laser scales linearly with N

The basic properties of mode locking are visualized with the help of Figs. 12.20–12.22. Figure 12.20 depicts the Fourier synthesis of a pulse obtained by the superposition of four sine waves with same amplitude and $\varphi_n(t) = 0$ according to (12.65), (12.66), and (12.67).

In Fig. 12.21 the dependence of the pulse duration and peak power on the number of locked modes is illustrated for this case. Finally in Fig. 12.22 the shape of the average output power is displayed for $N = 10$ equally spaced modes with different relative amplitudes and phase angles according to (12.65).

In the following we will summarize some more-technical related considerations. Mode locking is essentially achieved by applying a periodic loss (or gain) modulation to the intracavity radiation whose period is matched to the cavity round trip time. The mechanisms can be described either in the frequency or time domain.
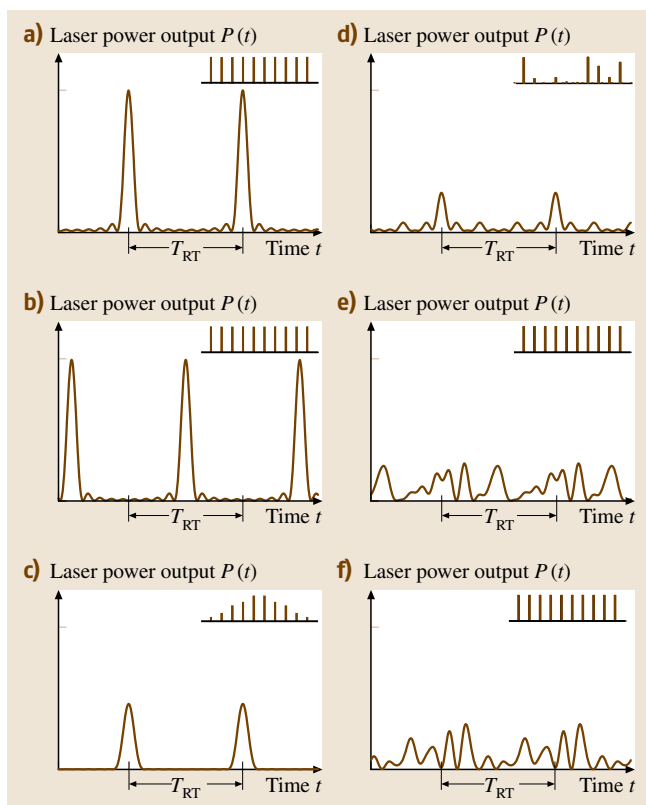
Fig. 12.22a–f Output power for 10 equally spaced modes with different relative amplitudes (as indicated in the *insets*) and phase angles (T_{RT} is the round-trip time): **(a)** linear phase relation $\varphi_n = n\alpha$ amongst the modes (i. e., a constant phase relation between two adjacent modes) with $\alpha = 0$, **(b)** linear phase relation $\varphi_n = n\alpha$ with $\alpha = \pi$, **(c)** Gaussian spectrum with five modes at FWHM and linear phase relation with $\alpha = 0$, **(d)** random spectrum and linear phase relation with $\alpha = 0$, **(e)** constant spectrum and random phase, **(f)** constant spectrum and different random phase

In the frequency domain one can start the consideration from the lowest-loss longitudinal mode. The periodic modulation at the frequency of the round-trip time leads to sidebands whose frequencies coincide with those of the adjacent longitudinal laser modes. In

this way energy is shifted from one mode to adjacent modes and as a result all longitudinal modes become finally locked in phase. In the time domain, the periodic modulation can be visualized as an intracavity shutter that is open once per round trip time. Such a stationary time window of minimum loss will provide a higher net gain on each round trip for those photons that are concentrated in that time window.

Approaches for providing the periodic modulation are grouped into active and passive schemes, and hybrid schemes that make use of a combination of the two. Active mode locking is obtained with an active element within the laser cavity, for example an acoustooptic modulator, generating a loss modulation. The modulation has to be precisely synchronized with the cavity round trips. Modulating the gain is also possible and can be achieved by synchronous pumping. In this case the amplifying medium of the laser is pumped with the output of another mode-locked laser whereby the cavity round-trip times for both lasers have to be matched. Passive mode locking is obtained by the laser radiation itself that produces the modulation via the interaction with a nonlinear device in the laser cavity. Typical nonlinear devices are some type of saturable absorbers which exhibit an intensity dependent loss as they interact with the laser radiation. This modulation is thus automatically synchronized to the cavity round-trip frequency. Because pulse timing does not have to be externally controlled there is usually no need for synchronization electronics, making passive schemes conceptually simpler compared to active schemes. Originally organic dyes were used as real saturable absorbers, for example to generate picosecond pulses from solid-state lasers and pulses down to 27 fs from dye lasers [12.99]. The shortest pulses nowadays are generated in solid-state laser media, being passively mode-locked using the optical Kerr effect. This approach was originated by [12.101]. Pulses with less than 6 fs are nowadays generated directly from Ti:sapphire lasers with Kerr-lens mode locking [12.53, 100]. At a center wavelength of 800 nm a pulse duration of 5.4 fs contains only two optical cycles at full-width half-maximum of the pulse intensity.

12.3 Measurement Techniques for Femtosecond Laser Pulses

For energy, power, spectrum and spatial beam measurements of ultrashort laser pulses standard laser diagnostic techniques are employed [12.5, 47]. For

a measurement of the pulse duration or more interesting of the time-dependent amplitude and phase of an ultrashort laser pulse, dedicated methods have been

developed and are described in several textbooks and references therein [12.4–6]. Here the basic ideas and underlying concepts are highlighted.

As the time and frequency domain are related by the Fourier transformation (12.6, 12.7, 12.11, 12.12) it should be sufficient to measure amplitude and phase in only one of the domains. Let us first shortly reflect on the frequency domain. All spectrometers no matter whether diffraction-grating or Fourier-transform devices measure a quantity that is proportional to the spectral intensity (Sect. 12.3.3) and therefore the phase information is lost.

On the other hand direct electronic techniques for temporal pulse-width measurements, consisting of fast photodiodes and high-bandwidth (sampling) oscilloscopes, are limited to the several-picosecond regime. Fast photodiodes are therefore not suited to record the temporal profile of an ultrashort laser pulse. Often they are employed to check on the mode-locked operation of an ultrafast oscillator or to derive synchronization signals for amplification setups or synchronized experiments. The only detector that reaches a time resolution below one picosecond is the streak camera. However, a characterization of ultrashort pulses with respect to amplitude and phase requires optical correlation techniques, especially methods that operate in the time–frequency

domain. The latter techniques will be described in more detail.

12.3.1 Streak Camera

The basic principle of a streak camera is depicted in Fig. 12.23. The ultrafast optical signal $I(t)$ to be analyzed is focused on a photocathode, where the signal is converted almost instantaneously into a number of electrons. The electrons then pass through a horizontal pair of accelerating electrodes and hit a phosphor screen after passing an electron multiplier (MCP). The screen is then imaged with the help of a highly sensitive camera (not shown). The temporal resolution relies on the concept of transferring a temporal profile into a spatial profile. This is done by passing the electron pulse between a pair of vertical sweep electrodes. A high voltage is applied to the sweep electrodes at a timing synchronized to the incident light. During this high-speed sweep the electrons arriving at different times are deflected at different angles and consequently hit the MCP at different vertical directions. In this manner the vertical position on the phosphor screen serves as a time axis. The brightness of the signal is proportional to the intensity profile of the incident ultrashort optical signal. The horizontal direction of the image corresponds to the horizontal location of
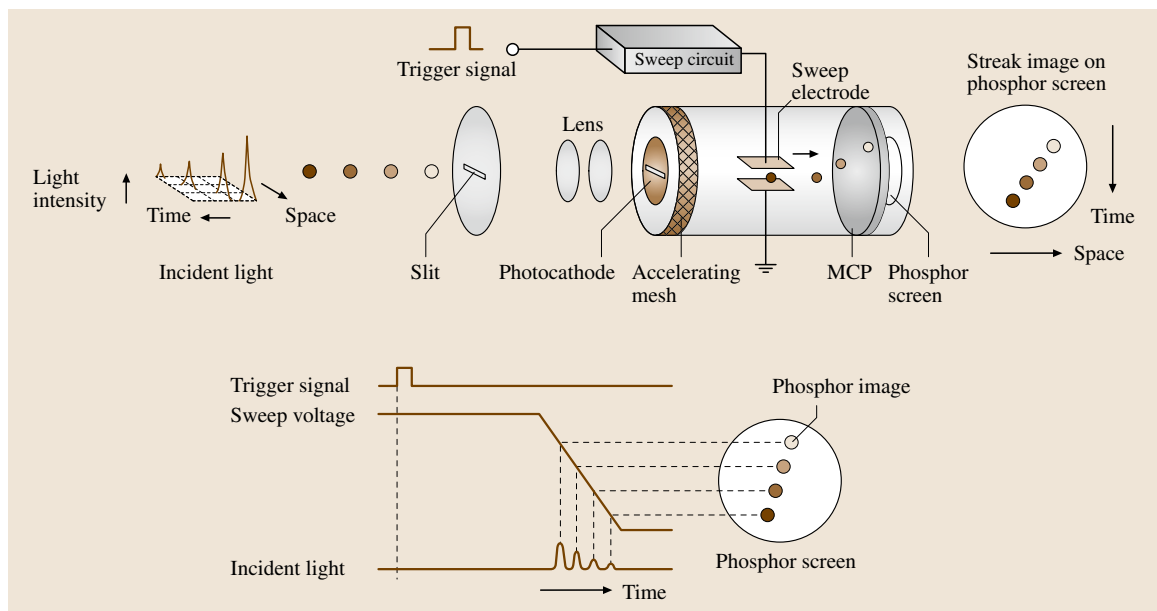
Fig. 12.23 Working principle (*top*) and timing (*bottom*) of a streak camera (after [12.102]). The spatial coordinate might be a wavelength coordinate after having dispersed the ultrashort optical signal with the help of a polychromator

the incident light. For example if the streak camera is used in combination with a polychromator the time variation of the incident light with respect to wavelength can be measured. Time-resolved spectroscopy is therefore one of the application areas of these devices. Commercial devices [12.102, 103] are quoted with a temporal resolution of $< 200\,\text{fs}$. Using different photocathode materials a spectral response can be achieved from 115 nm up to 1600 nm. X-ray streak cameras with a temporal resolution of 1.5 ps are quoted as well.

12.3.2 Intensity Autocorrelation and Cross–Correlation

A widely used technique to estimate the pulse duration or to check whether a laser produces pulses rather than statistical intensity fluctuations is to measure the so-called intensity autocorrelation S_{intAC} [12.104]

$$S_{\text{intAC}}(\tau) = \int_{-\infty}^{\infty} I(t)I(t+\tau)\,\mathrm{d}t$$

$$= \int_{-\infty}^{\infty} I(t)I(t-\tau)\,\mathrm{d}t = S_{\text{intAC}}(-\tau) . \quad (12.68)$$

This is the time integral of one pulse intensity multiplied by the intensity of a time-shifted replica of the same pulse as a function of the time shift τ. The intensity autocorrelation has its maximum at $\tau = 0$ and is always symmetrical (12.68). In this fundamental arrangement one pulse serves as a gate to scan the other.

Fig. 12.24a,b Optical layout for autocorrelation setups. **(a)** Collinear autocorrelator (dispersion minimized): the incoming pulse is split into two parts, where one is variably delayed with respect to the other. The pulses are recombined and focused on a nonlinear signal generator (NLSG). Second-harmonic generation in thin crystals and two-photon absorption in semiconductor photodiodes are commonly used for this purpose. Other second-order nonlinear effects can be used as well. The nonlinear signal is measured as a function of delay. If the measurement is performed with interferometric accuracy the interferometric autocorrelation is recorded. If the setup averages the fast oscillations of the light field (12.76) the intensity autocorrelation with background is recorded, having a center-to-offset ratio of 3 : 1 (12.77). **(b)** Noncollinear autocorrelator for recording the background free intensity autocorrelation (M = mirror; BS = beam splitter; SHG = second harmonic generation; D = detector; L = lens) ▶

It can be realized with any interferometer (Fig. 12.24) that splits the pulse into two pulses and recombines them with an adjustable time delay between them. Note within that context that, for example a 100 fs pulse duration, corresponds to a spatial extent of $30\,\mu\text{m}$, a dimension readily measurable with standard translation stages. Measuring the spatial overlap of the two pulses requires a nonlinear process to generate a detection signal proportional to the intensity product of the
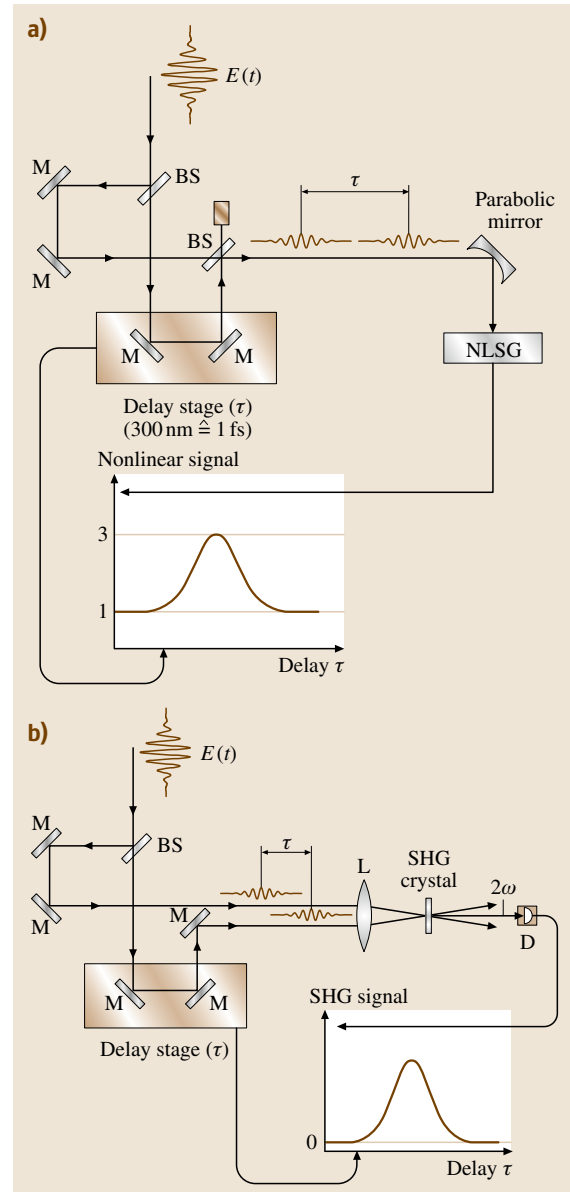
two pulses. Second-harmonic generation in thin crystals and two-photon absorption in semiconductor photodiodes [12.105, 106] are commonly used (in a *two-photon diode* the photon energy is within the band gap and only simultaneous two-photon absorption can lead to a signal). In the case of frequency-doubling crystals thin crystals have to be used in order to ensure that the ratio of the crystals phase-matching bandwidth to the pulse spectral bandwidth is large. For 100 fs pulses at 800 nm the beta-barium borate (BBO) crystal thickness should not be thicker than $\approx 100\,\mu m$ and crystals as thin as $5\,\mu m$ have been used to measure few-fs pulses [12.6].

The intensity autocorrelation is obtained directly, when the two time-delayed laser pulses are not recombined collinearly but focused at a mutual angle into the thin nonlinear crystal. This leads to the so-called background free intensity autocorrelation. For the collinear setup the intensity autocorrelation is obtained by averaging the fast oscillations of the light field (12.76).

The collinear intensity autocorrelation has a signal-to-background ratio of 3 : 1 (12.77).

The intensity autocorrelation provides only limited information on the pulse shape, because there are infinitely many symmetric and asymmetric pulse shapes that lead to very similar symmetric autocorrelation traces. The procedure to estimate a pulse duration from intensity autocorrelations is to assume a pulse shape and then to calculate the FWHM pulse duration Δt from the known ratio with respect to the FWHM of the intensity autocorrelation Δt_{intAC}. In this approach generally Gaussian shapes or hyperbolic secant shapes are assumed. The ratio $\Delta t_{intAC}/\Delta t$ for various shapes [12.22] is given in Table 12.1.

If a pulse $I_1(t)$ is characterized, for example, in such a way it can be used to gate a second unknown pulse $I_2(t)$ by measuring the intensity cross-correlation S_{intCC} with a suitable nonlinear second-order signal like, for example, sum- or difference-frequency mixing or two-photon photodiodes

$$S_{intCC}(\tau) = \int_{-\infty}^{\infty} I_1(t) I_2(t+\tau)\, dt\,. \tag{12.69}$$

For Gaussian pulse shapes the corresponding FWHM quantities are related by

$$\Delta t_{intCC}^2 = \Delta t_1^2 + \Delta t_2^2\,. \tag{12.70}$$

In general the second momenta of the individual pulses have to be considered [12.23].
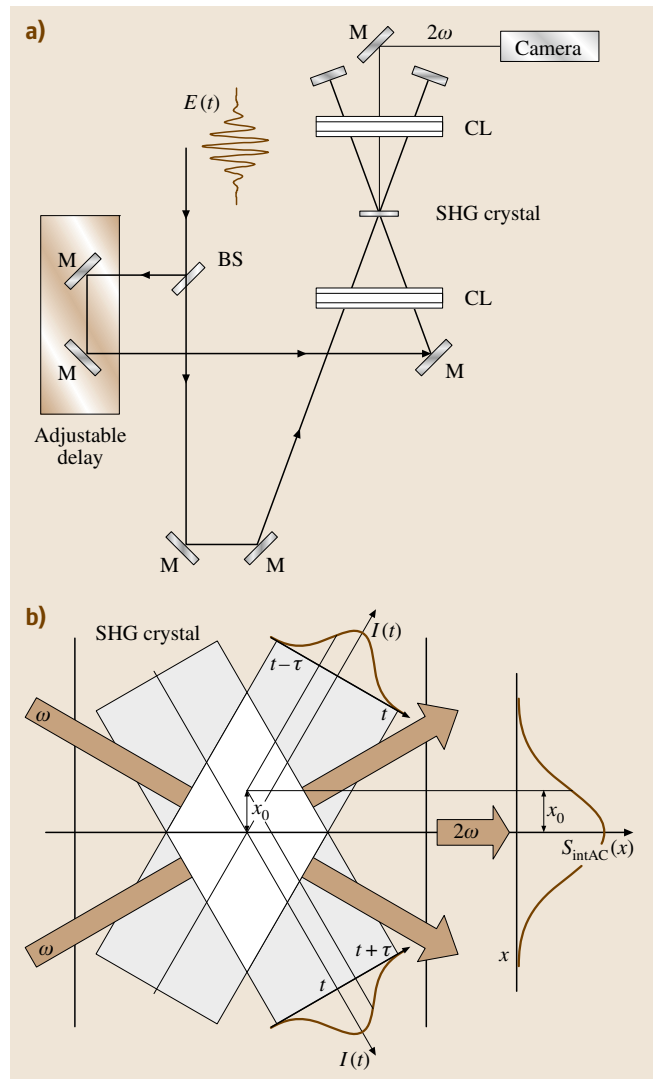
Fig. 12.25 (a) Optical layout for a single-shot autocorrelator. The delayed replicas of the incident pulse are focused with the help of a cylindrical lens (CL) onto a second-harmonic generation (SHG) crystal. The spatiotemporal overlap of the two spatially extended pulses is measured via SHG and recorded with a camera (M = mirror; BS = beam splitter). **(b)** Detail of **(a)**. In the region of spatiotemporal overlap, second-harmonic generation is induced via type I phase matching and the autocorrelation in time is transformed into a spatial intensity distribution along the x-axis (after [12.5])

For high-power femtosecond laser systems higher-order cross-correlations $S_{higher\,order\,int\,CC}$ are a very convenient and powerful tool to determine intensity profiles by making use of nonlinear optical processes of the

order $n + 1$ and $m + 1$

$$S_{\text{higher order intCC}}(\tau) = \int_{-\infty}^{\infty} I_1^n(t) I_2^m(t + \tau) \, dt \; . \quad (12.71)$$

In this case the corresponding FWHM quantities assuming Gaussian pulse shapes are given by

$$\Delta t_{\text{higher-order intCC}}^2 = \frac{1}{n} \Delta t_1^2 + \frac{1}{m} \Delta t_2^2 \; . \quad (12.72)$$

The intensity autocorrelation does not necessarily have to be recorded by moving one interferometer arm as depicted in Fig. 12.24. In a so-called single-shot autocorrelator [12.107, 108] the two pulses are coupled noncollinearly into a thin frequency-doubling crystal (Fig. 12.25). Only in a small region within the crystal the pulses have spatiotemporal overlap. According

to the geometry of the setup in Fig. 12.25b the delay time τ is related to the spatial coordinate x_0. Imaging the frequency-doubled signal yields an intensity autocorrelation as a function of the spatial coordinate

$$S_{\text{intAC}}(x_0) = \int_{-\infty}^{\infty} I(x) I(x + x_0) \, dx \; . \quad (12.73)$$

These single-shot devices are especially suited for high-intensity femtosecond laser pulses and are therefore convenient tools to adjust low-repetition femtosecond amplifiers. Phase-sensitive setups have also been reported [12.108, 109].

12.3.3 Interferometric Autocorrelations

We will now discuss the case of a collinear autocorrelation in more detail. The simplest interferometric signal is that from a linear detector that records the intensity of the recombined pulses. For identical electric fields E of the two pulses, the signal $S_{\text{linear interferometric AC}}$ as a function of their relative delay τ is

$$S_{\text{linear interferometric AC}}(\tau) = \int_{-\infty}^{\infty} [E(t) + E(t + \tau)]^2 \, dt$$

$$= 2 \int_{-\infty}^{\infty} I(t) \, dt$$

$$+ 2 \int_{-\infty}^{\infty} E(t) E(t + \tau) \, dt \quad (12.74)$$

where we have skipped the prefactors defined in Sects. 12.1.1 and 12.1.2. The signal consists of an offset given by the summed intensity of the two pulses and the interference term that is described by an autocorrelation of the electric field. The Wiener–Khintchine theorem states that the Fourier transformation of the

Fig. 12.26a–e Quadratic interferometric autocorrelation **(a)** and the isolated components S_{f_0}, S_{f_1} and S_{f_2} in the time domain **(b)**–**(d)** for a bandwidth-limited Gaussian pulse of 10 fs pulse duration. Note that the offset in **(a)** introduces an additive value at $\omega = 0$ and **(e)** is therefore the Fourier transform of the offset-corrected curve. $\Delta t_{\text{quadratic interferometric AC}}$ is indicated in **(a)** in addition (in the figure qiAC is used as a shorthand notation for quadratic interferometric AC) ◄
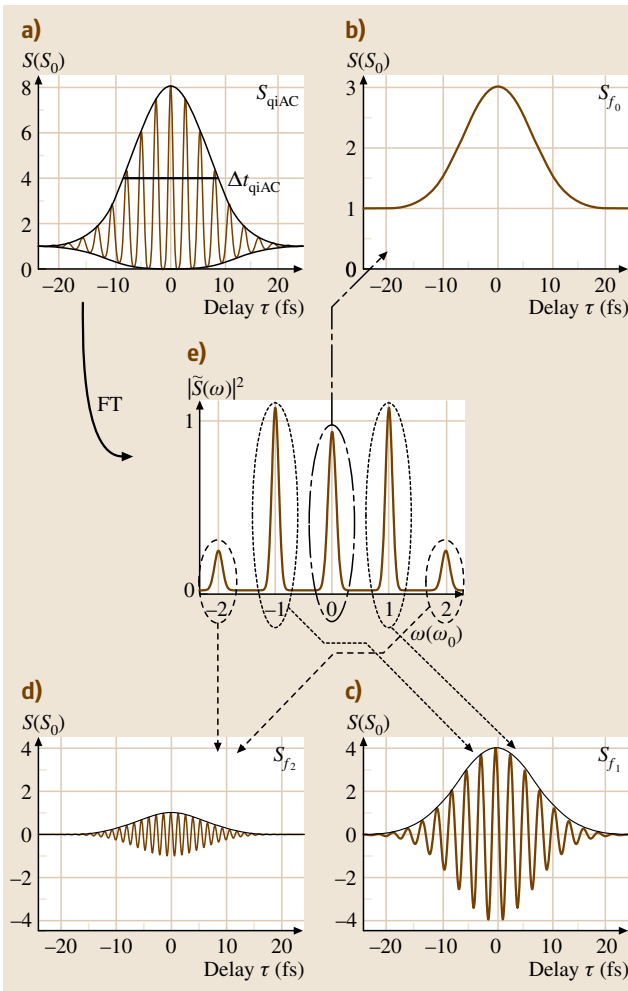
autocorrelation of the electric field yields the spectral density [12.110] – a quantity that is proportional to the spectral intensity $I(\omega)$, which is the basis for Fourier spectroscopy. A linear autocorrelation therefore contains no information beyond the amplitude of the spectrum and the total intensity of the pulse.

A solution to this problem is a nonlinear detector that is sensitive to the squared intensity and yields the signal $S_{\text{quadratic interferometric AC}}$

$$S_{\text{quadratic interferometric AC}}(\tau)$$
$$= \int_{-\infty}^{\infty} \left\{ [E(t) + E(t+\tau)]^2 \right\}^2 dt . \tag{12.75}$$

Taking the electric field as $E(t) = \text{Re}[A(t)e^{i\Phi_a(t)}e^{i\omega_0 t}]$ and defining $S_0 = \int_{-\infty}^{\infty} A^4(t) dt$ in order to normalize one obtains, similar to [12.4, 111],

$$S_{\text{quadratic interferometric AC}}(\tau) = \frac{1}{S_0} \left(S_{f_0} + S_{f_1} + S_{f_2} \right)$$

with

$$S_{f_0} = \int_{-\infty}^{\infty} \left[A^4(t) + 2A^2(t)A^2(t+\tau) \right] dt ,$$

$$S_{f_1} = 2\,\text{Re} \left\{ e^{i\omega_0\tau} \int_{-\infty}^{\infty} A(t)A(t+\tau) \right.$$
$$\left. \times \left[A^2(t) + A^2(t+\tau) \right] e^{i[\Phi_a(t+\tau) - \Phi_a(t)]} dt \right\} ,$$

$$S_{f_2} = \text{Re} \left[e^{i2\omega_0\tau} \int_{-\infty}^{\infty} A^2(t)A^2(t+\tau) \right.$$
$$\left. \times e^{i2[\Phi_a(t+\tau) - \Phi_a(t)]} dt \right] , \tag{12.76}$$

where Re denotes the real part. According to (12.48) the signal $S_{\text{quadratic interferometric AC}}$ can be decomposed into three frequency components, S_{f_0}, S_{f_1} and S_{f_2}, at $\omega \approx 0$, $\omega \approx \pm\omega_0$, and $\omega \approx \pm 2\omega_0$, respectively, as illustrated in Fig. 12.26.

S_{f_0} corresponds to an intensity correlation with background. It can be obtained either by Fourier filtering or by averaging the fast oscillations in the experiment directly. With (12.76) it follows that this

intensity autocorrelation has a center-to-offset ratio of

$$\frac{S_{f_0}(0)}{S_{f_0}(\infty)} = \frac{\int_{-\infty}^{\infty} 3A^4(t) dt}{\int_{-\infty}^{\infty} A^4(t) dt} = \frac{3}{1} . \tag{12.77}$$

S_{f_1} is a sum of two mutual symmetric cross-correlations and depends explicitly on the temporal phase $\Phi_a(t)$.

S_{f_2} represents an autocorrelation of the second harmonic field and is therefore related to the spectral intensity of the second-harmonic spectrum. It also depends on the temporal phase $\Phi_a(t)$. Note that phase-modulated pulses having the same spectral intensity can have very different spectral intensities after frequency doubling (Fig. 12.27). This has been exploited in recent experiments [12.21, 112, 113]. Making use of a pulse shaper (Sect. 12.1.3) that scans calibrated phase functions and at the same time measuring the second-harmonic spectrum is a noninterferometric method to characterize the spectral phase of ultrashort laser pulses [12.114]. All three components add constructively at $\tau = 0$ and yield a center to background ratio of 8 : 1. This can be directly seen from (12.75)

$$\frac{S_{\text{quadratic interferometric AC}}(0)}{S_{\text{quadratic interferometric AC}}(\infty)}$$
$$= \frac{\int_{-\infty}^{\infty} (E+E)^4 dt}{\int_{-\infty}^{\infty} E^4 dt + \int_{-\infty}^{\infty} E^4 dt} = \frac{16 \int_{-\infty}^{\infty} E^4 dt}{2 \int_{-\infty}^{\infty} E^4 dt} = \frac{8}{1} . \tag{12.78}$$

The center-to-background ratios are used in experiments to check the proper alignment of the interferometer. In order to derive phase information analytical functions, for example Gaussians, can be fitted to the $S_{\text{quadratic interferometric AC}}$ [12.111]. Taking the knowledge of the spectrum into account iterative algorithms that make no assumptions about the underlying pulse shapes have been reported [12.115, 116]. Both approaches deliver meaningful results only for linear chirps and in the case of nearly no noise. The influence of noise on autocorrelation measurements is discussed in [12.4, 117]. This is an important point as most often measurements are performed over an average of pulse trains. Other sources of systematic error in autocorrelation measurements are discussed in [12.6].

The ratio $\Delta t_{intAC}/\Delta t$ is only valid for the intensity autocorrelation of a bandwidth-limited pulse. For bandwidth-limited Gaussian pulses the FWHM of a quadratic interferometric autocorrelation signal (taken at 4 in a 8 : 1 plot as displayed in Fig. 12.26a) relates to

the pulse duration by

$$\frac{\Delta t_{\text{quadratic interferometric AC}}}{\Delta t} = 1.6963 \tag{12.79}$$
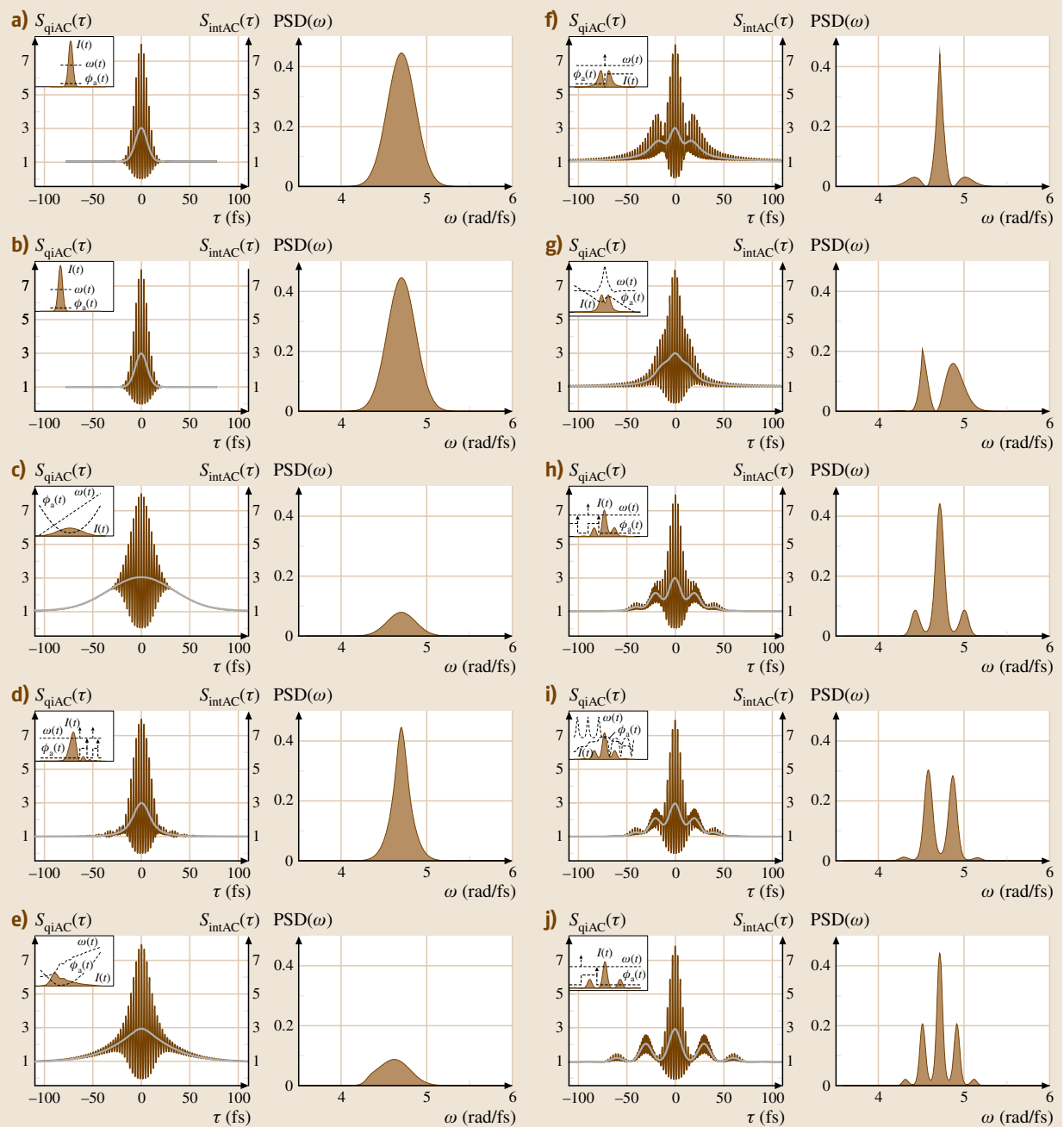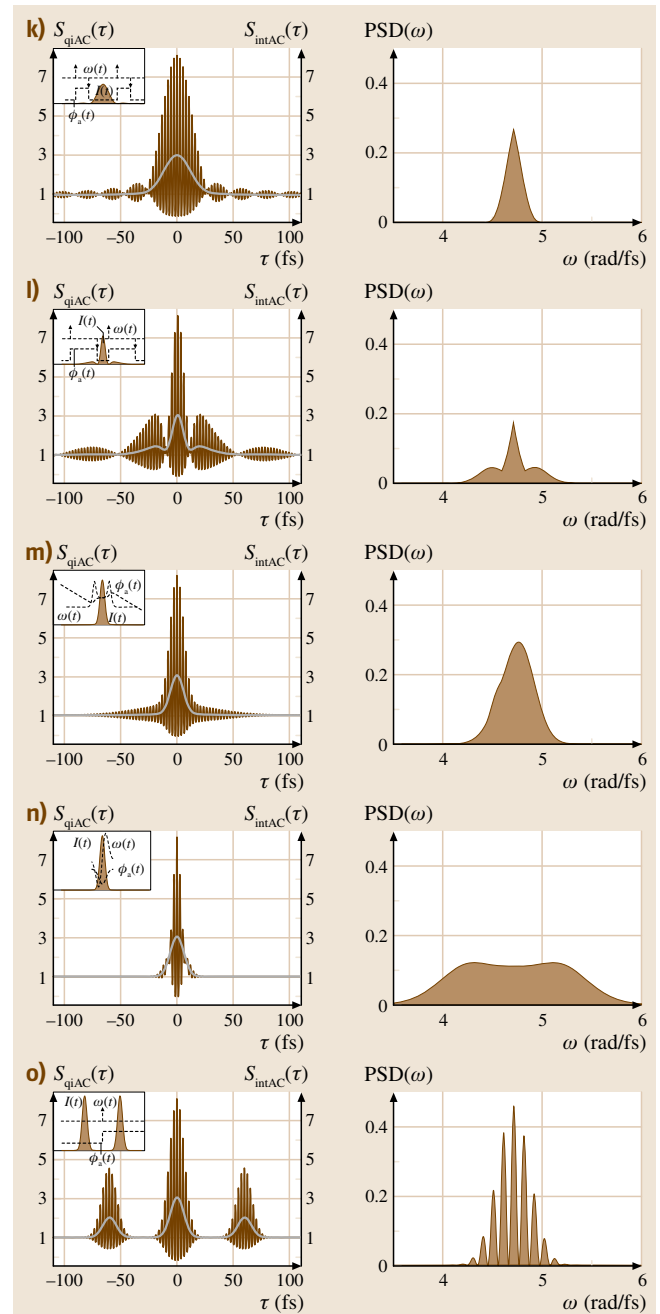
for bandwidth-limited Gaussian pulses. Figure 12.27 compiles for different pulses the resulting interferometric autocorrelation traces together with the intensity autocorrelation and the spectrum at the second harmonic of the fundamental.
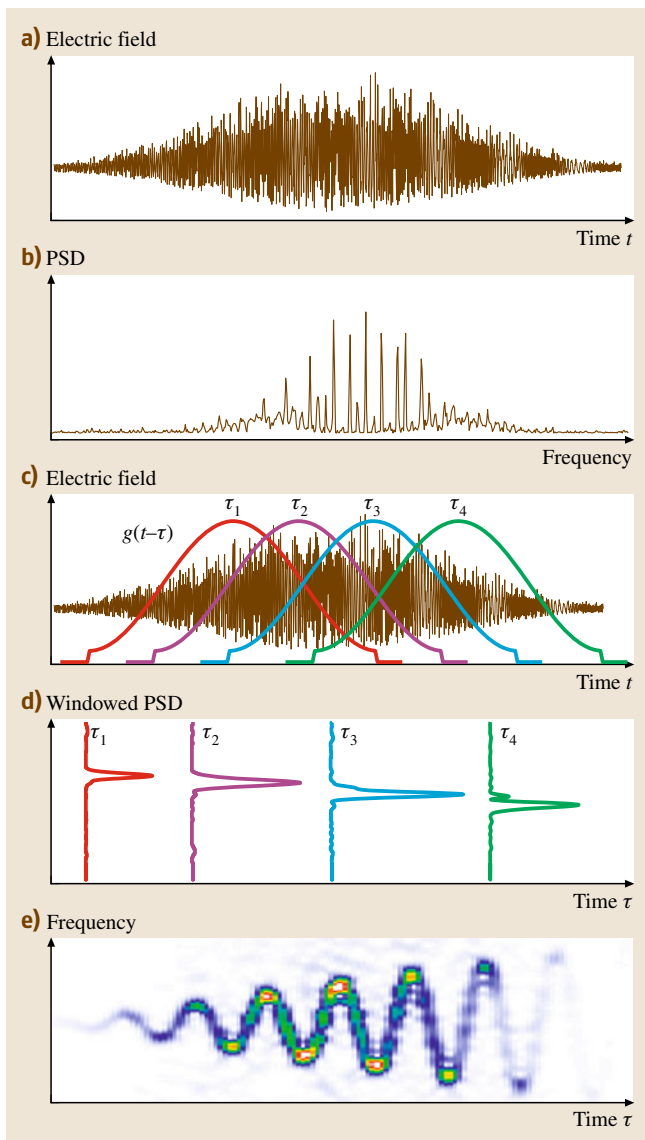
12.3.4 Time–Frequency Methods

As described above, the interferometric autocorrelation, even together with the independently measured spectrum, does not give sufficient information to characterize arbitrary-shaped ultrashort laser pulses with respect to their temporal amplitude $A(t)$ or temporal intensity $I(t)$ and the temporal phase function $\Phi_a(t)$ or their frequency-domain counterparts (Sect. 12.1.2).

Fig. 12.27a–o *Left*: quadratic interferometric autocorrelation $S_{\text{quadratic interferometric AC}}(\tau)$ (*black*) and intensity autocorrelation $S_{\text{int AC}}(\tau)$ (*grey*) for the pulse shapes of Fig. 12.3 with a central wavelength of 800 nm. The temporal intensity $I(t)$, the additional temporal phase $\Phi_a(t)$ and the instantaneous frequency $\omega(t)$ are shown in the *insets*. *Right*: corresponding power spectrum density PSD(ω) of $S_{\text{qiAC}}(\tau)$ displayed in the region of the second harmonic. Note that for pulses **(a)** to **(j)** the linear spectrum remains unchanged. **(a)** Bandwidth-limited Gaussian laser pulse of 10 fs duration, **(b)** bandwidth-limited Gaussian laser pulse of 10 fs duration shifted in time to -20 fs due to a linear phase term in the spectral domain ($\phi' = -20$ fs), **(c)** symmetrical broadened Gaussian laser pulse due to $\phi'' = 200$ fs^2, **(d)** third-order spectral phase ($\phi''' = 1000$ fs^3) leading to a quadratic group delay, **(e)** combined action of all spectral phase coefficients **(a)**–**(d)**, **(f)** π step at the central frequency, **(g)** π step displaced from the central frequency, **(h)** sine modulation at the central frequency with $\phi(\omega) = 1\sin[20\,\text{fs}(\omega - \omega_0)]$, **(i)** cosine modulation at the central frequency with $\phi(\omega) = 1\cos[20\,\text{fs}(\omega - \omega_0)]$, **(j)** sine modulation at the central frequency with $\phi(\omega) = 1\sin[30\,\text{fs}(\omega - \omega_0)]$, **(k)** symmetrical clipping of spectrum, **(l)** blocking of the central frequency components, **(m)** off-center absorption, **(n)** self-phase modulation. Note the spectral broadening, **(o)** double pulse, with a pulse-to-pulse delay of 60 fs. Note that the second harmonic field $E^2(t) = A^2(t)e^{2i\Phi_a(t)}e^{2i\omega_0 t}$ gives rise to the autocorrelation function S_{f_2} is related to the second harmonic PSD, i.e. squared modulus of the Fourier transform of $E^2(t)$ as displayed in the right column. Hence, the shape of the second harmonic PSD is determined by phase modulation of the linear spectrum and can be used to efficiently control two-photon resonant processes [12.21, 112, 113] ◄►
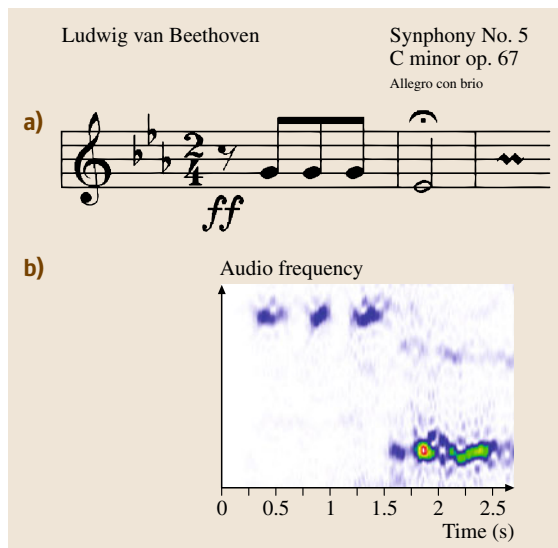
Techniques have emerged that operate not in the time or frequency domain but in the *joint time–frequency domain*, involving both temporal resolution and frequency resolution simultaneously [12.24, 118] and being able to completely determine the pulse shape [12.6].

a) Electric field

Time t

b) PSD

Frequency

c) Electric field

$g(t-\tau)$ τ_1 τ_2 τ_3 τ_4

Time t

d) Windowed PSD

τ_1 τ_2 τ_3 τ_4

Time τ

e) Frequency

Time τ

Fig. 12.28a–e Illustration of a short-time Fourier transform of a complicated electric field. (**a**) Electric field as a function of time; (**b**) power spectrum density as a function of frequency; (**c**) gating the electric field; four different time delays are shown; (**d**) power spectrum density for each gate; (**e**) spectrogram, revealing an oscillating instantaneous frequency as a function of time being the origin for the complicated electric field in (**a**)

Ludwig van Beethoven   Synphony No. 5 C minor op. 67

Allegro con brio

a)

ff

b)   Audio frequency

0   0.5   1   1.5   2   2.5

Time (s)

Fig. 12.29a,b Sheet of music (**a**) and corresponding spectrogram (**b**) of Beethoven's fifth symphony

the frequency has to be held. The sheet of music will tell us in what order the notes have to be played and additional information like *piano* and *forte* is given to indicate the intensity to be played. The first few notes of Beethoven's fifth symphony are given as an example in Fig. 12.29a. If an orchestra is playing the music and we wish to graphically record the music, a spectrogram $S_{\text{spectrogram}}(\omega, \tau)$ is a useful quantity. A spectrogram of a function $f(t)$ is defined as the energy density spectrum of a short-time Fourier transform STFT(ω, τ)

$$S_{\text{spectrogram}}(\omega, \tau) \equiv |\text{STFT}(\omega, \tau)|^2$$

$$= \left| \int_{-\infty}^{\infty} f(t)g(t-\tau)e^{-i\omega t}\, dt \right|^2 ,$$

(12.80)

where $g(t-\tau)$ denotes the gate (or window) function. The concept behind it is simple and powerful. If we want to analyze what is happening at a particular time, we just use a small portion of the signal centered at that time, calculate its spectrum and do it for each instant of time. A spectrogram corresponding to the beginning of Beethoven's fifth symphony is shown in Fig. 12.29b.

Figure 12.28 shows the concept of STFT on a complicated electric field of a laser. Once an electric field is retrieved in amplitude and phase there are other time – frequency distributions in use for displaying

For illustration purposes we start with an example from music: in order to describe a line of music we use notes. The frequency is indicated by the pitch of the note and the duration of the note indicates how long

Fig. 12.30a–o Calculated FROG traces at corresponding frequencies for various ultrashort pulse shapes with a central wavelength of 800 nm according to the pulses displayed in Fig. 12.3. *Left*: polarization gate (PG) FROG. *Right*: second-harmonic generation (SHG) FROG. The temporal intensity $I(t)$, the additional temporal phase $\Phi_a(t)$ and the instantaneous frequency $\omega(t)$ are shown in the *insets* as a reminder. **(a)** Bandwidth-limited Gaussian laser pulse of 10 fs duration, **(b)** bandwidth-limited Gaussian laser pulse of 10 fs duration shifted in time to -20 fs due to a linear phase term in the spectral domain ($\phi' = -20$ fs), **(c)** symmetrical broadened up chirped Gaussian laser pulse due to $\phi'' = 200$ fs^2, **(d)** third-order spectral phase ($\phi''' = 1000$ fs^3) leading to a quadratic group delay, **(e)** combined action of all spectral phase coefficients **(a)**–**(d)**, **(f)** π step at the central frequency, **(g)** π step displaced from the central frequency, **(h)** sine modulation at the central frequency with $\phi(\omega) = 1\sin[20\,\text{fs}(\omega - \omega_0)]$, **(i)** cosine modulation at the central frequency with $\phi(\omega) = 1\cos[20\,\text{fs}(\omega - \omega_0)]$, **(j)** sine modulation at the central frequency with $\phi(\omega) = 1\sin[30\,\text{fs}(\omega - \omega_0)]$, **(k)** symmetrical clipping of spectrum, **(l)** blocking of the central frequency components, **(m)** off-center absorption, **(n)** self-phase modulation, (note the spectral broadening), **(o)** double pulse, with a pulse-to-pulse delay of 60 fs ▶

the data like for example the Wigner [12.24, 119–122] and Husimi representations [12.123, 124]. A quantity closely related to the spectrogram is the sonogram $S_{\text{sonogram}}(\omega, \tau)$

$$S_{\text{sonogram}}(\omega, \tau) \equiv \left| \int_{-\infty}^{\infty} \tilde{f}(\omega')\tilde{g}(\omega - \omega')\,e^{+i\omega'\tau}\,d\omega' \right|^2 ,$$
(12.81)

where $\tilde{g}(\omega - \omega')$ is a frequency gate in analogy to the time gate $g(t - \tau)$ used in the spectrogram. If $\tilde{g}(\omega)$ is the Fourier transform of $g(t)$ then it can be shown that the sonogram is equivalent to the spectrogram [12.6].

In ultrafast optics, the gate to record the spectrogram or the sonogram is usually the pulse itself.

Spectrogram–Based Methods

Recording a spectrogram is accomplished experimentally by gating the pulse with a variable delayed replica of the pulse in an instantaneous nonlinear optical medium followed by spectrally resolving the gated pulse. The basic optical layout of such a device is almost the same as a noncollinear autocorrelation setup
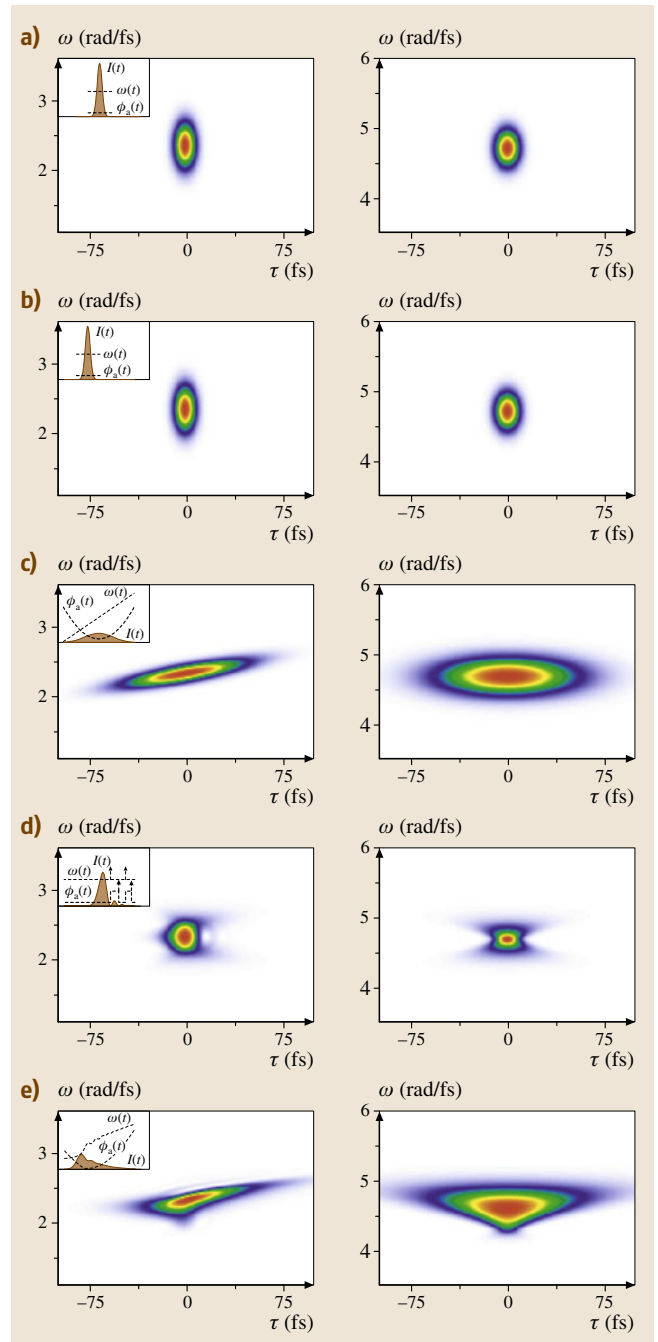
depicted in Fig. 12.24b. Only the detector has to be replaced by a spectrometer and camera system in order to spectrally resolve the gated pulse. The corresponding technique has been termed frequency-resolved optical
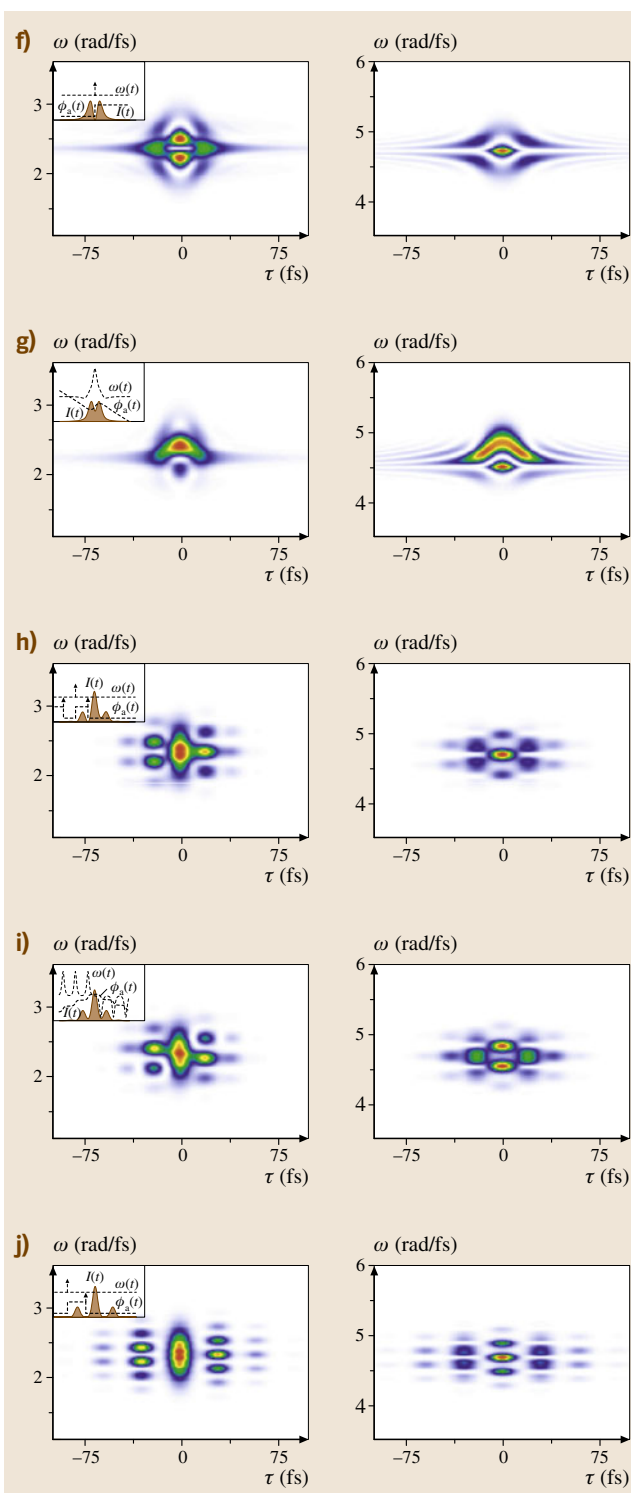
gating (FROG) and is described in great detail in [12.6, 125] and references therein.

Depending on the instantaneous nonlinear optical effect used to gate the pulse in FROG, several different FROG geometries have been investigated (the setup of Fig. 12.24b would correspond to a second-harmonic-generation (SHG) FROG). These geometries can also be implemented as single-shot devices, similar to the single-shot autocorrelator depicted in Fig. 12.25. The FROG trace $I_{\text{FROG}}(\omega, \tau)$, that is a plot of frequency (wavelength) versus delay, is a spectrogram of the complex amplitude E_c (12.15). Neglecting any prefactors, different nonlinear optical effects yield the following expressions according to [12.6, 125].

Polarization–Gate (PG) FROG.

$$
I_{\text{FROG}}^{\text{PG}}(\omega, \tau) = \left| \int_{-\infty}^{\infty} E_c(t)\, |E_c(t - \tau)|^2\, e^{-i\omega t}\, dt \right|^2 .
$$

(12.82)

In a crossed-polarizer arrangement for the probe pulse this technique makes use of induced birefringence in fused silica in the presence of the gate pulse. The third-order optical nonlinearity is the electronic Kerr effect. The FROG traces obtained by this method are very intuitive (Fig. 12.30).

Self–Diffraction (SD) FROG.

$$
I_{\text{FROG}}^{\text{SD}}(\omega, \tau) = \left| \int_{-\infty}^{\infty} E_c(t)^2 E_c^*(t - \tau)\, e^{-i\omega t}\, dt \right|^2 .
$$

(12.83)

In this approach the two beams (with the same polarization) generate a sinusoidal intensity pattern in the nonlinear medium (for example, fused silica) and hence introduce a material grating, which diffracts each beam. One of the diffracted beams is then the signal beam sent to the spectrometer.

Transient–Grating (TG) FROG.

$$
I_{\text{FROG}}^{\text{TG}}(\omega, \tau)
$$
$$
= \left| \int_{-\infty}^{\infty} E_{c1}(t) E_{c2}^*(t) E_{c3}(t - \tau)\, e^{-i\omega t}\, dt \right|^2 . \quad (12.84)
$$

This is a three-beam setup, where two pulses are overlapped in time and space at the optical Kerr medium

(for example fused silica), producing a refractive index grating similar as in SD FROG. In a TG a third pulse is variably delayed and overlapped in the fused silica and is diffracted by the induced grating, producing the signal beam for the spectrometer. The beams in the TG geometry (three input and one output) are kept nearly collinear and form a so-called boxcars arrangement, where the four spots appear in the corners of a rectangle when placing a card into the beams after the nonlinear medium. As TG is a phase-matched process, the sensitivity is higher compared to the SD approach. Depending on which pulse is variably delayed – with the other two coincident in time – the TG FROG trace is mathematically equivalent to the PG FROG (pulse one or three is delayed) or to the SD FROG (pulse two is delayed).

Third–Harmonic–Generation (THG) FROG.

$$I_{\mathrm{FROG}}^{\mathrm{THG}}(\omega, \tau) = \left| \int_{-\infty}^{\infty} E_{\mathrm{c}}(t - \tau)^2 E_{\mathrm{c}}(t) \, \mathrm{e}^{-\mathrm{i}\omega t} \, \mathrm{d}t \right|^2 .$$

(12.85)

This method makes use of third-harmonic generation as the nonlinear process.

Second–Harmonic–Generation (SHG) FROG.

$$I_{\mathrm{FROG}}^{\mathrm{SHG}}(\omega, \tau) = \left| \int_{-\infty}^{\infty} E_{\mathrm{c}}(t) E_{\mathrm{c}}(t - \tau) \, \mathrm{e}^{-\mathrm{i}\omega t} \, \mathrm{d}t \right|^2 .$$

(12.86)

SHG FROG involves spectrally resolving a standard SHG-based noncollinear intensity autocorrelator, which always yields symmetric traces, resulting in a direction of time ambiguity for the SHG FROG. This ambiguity can experimentally be removed, for example, by placing a piece of glass in the beam before the beam splitter to introduce positive chirp or to create satellite pulses via surface reflections. Because of its high sensitivity and as it is based on a standard SHG autocorrelator, this method is widely employed. Examples of SHG FROG traces for various pulse shapes are given in Fig. 12.30.

A comparison of the different approaches is given in Table 12.4. Various calculated traces for common ultrashort pulse distortions for the PG and the SHG FROG geometries are given in Fig. 12.30. Calculated FROG traces for the other beam geometries are given
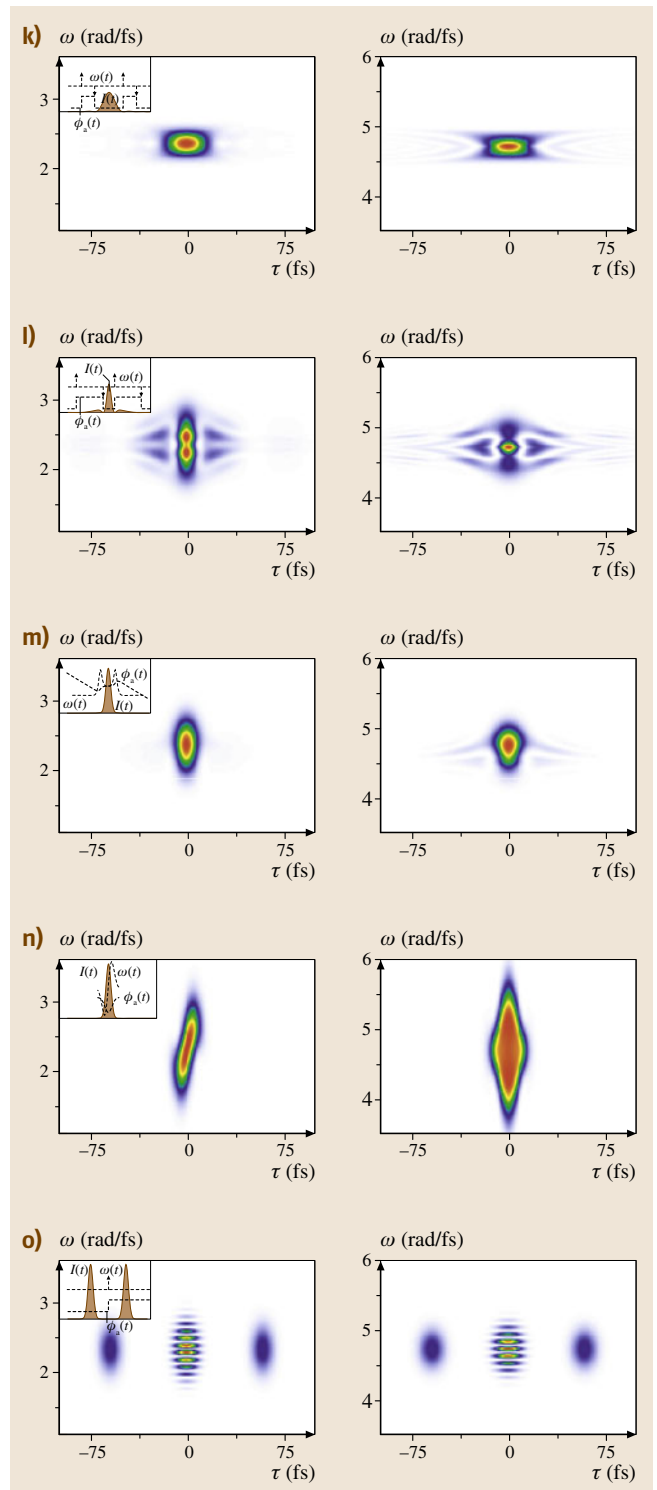
Table 12.4 Comparison of different FROG geometries (PG = polarization gate; SD = self-diffraction; TG = transient grating; THG = third-harmonic generation; SHG = second-harmonic generation). Sensitivities are only approximate and assume 800 nm 100 fs pulses focused to about 100 μm (10 μm for THG) to be measured. In the schematics only the part involving the nonlinear optical effect characterized by its nonlinearity is displayed. Not shown are delay lines and various lenses, as these are common to all setups and are similar to the optical layouts shown in Figs. 12.24b and 12.25. Solid lines indicate input pulses; dashed lines indicate signal pulses. The frequencies shown (ω, 2ω, 3ω) are the carrier frequencies of the pulses taking part and indicate whether the signal pulse has the same carrier frequency as the input pulse or is shifted as in SHG and THG. D denotes a detector being composed of a spectrometer and camera system. (WP = wave plate; P = polarizer) (after [12.6])

Geometry	PG	SD	TG	THG	SHG
Nonlinearity	$\chi^{(3)}$	$\chi^{(3)}$	$\chi^{(3)}$	$\chi^{(3)}$	$\chi^{(2)}$
Sensitivity (single shot) (μJ)	≈ 1	≈ 10	≈ 0.1	≈ 0.03	≈ 0.01
Sensitivity (multi shot) (nJ)	≈ 100	≈ 1000	≈ 10	≈ 3	≈ 0.001
Advantages	Intuitive traces; automatic phase matching	Intuitive traces; deep UV capability	Background-free; sensitive; intuitive traces; deep UV capability	Sensitive; very large bandwidth	Very sensitive
Disadvantages	Requires polarizers	Requires thin medium; not phase matched	Three beams	Unintuitive traces; very short λ signal	Unintuitive traces; short λ signal
Ambiguities	None known	None known	None known	Relative phase of multiple pulses $\phi, \phi \pm 2\pi/3$	Relative phase of multiple pulses $\phi, \phi + \pi$; direction of time
Schematics					

in [12.125]. Measured FROG traces for different geometries are compiled in [12.6].

It is important to note that knowledge of the spectrogram (or sonogram) of the electric field of an ultrashort laser pulse is sufficient to completely determine the electric field in amplitude and phase (besides some ambiguities such as the absolute phase) because a spectrogram is equivalent to the two-dimensional phase-retrieval problem in image science and astronomy [12.126]. In general, phase retrieval is the problem of finding a function knowing only the magnitude (but not the phase) of its Fourier transform. Phase retrieval for a function of one variable is impossible. For example, knowledge of a pulse spectrum does not fully determine the pulse as infinitely many different pulses have the same spectrum (Fig. 12.3a–j). However, phase retrieval for a function of two variables is possible and the FROG trace can be rewritten as the squared magnitude of a two-dimensional Fourier transform [12.125]. Very sophisticated iterative retrieval procedures, which can rapidly retrieve the pulse from the FROG trace with update rates up to several Hz, exist [12.127].

In the following some additional attributes of FROG techniques, which also partially hold for sonogram methods, are summarized:

● As the FROG trace consists of $N \times N$ points, while the intensity and phase on the other hand only have $2N$ points, the FROG trace overdetermines the pulse. This gives rise to an increased robustness of the two-dimensional methods and to an improved immunity towards measurement noise. The noncon-

vergence of the FROG algorithm therefore can be a hint of the presence of systematic errors.

- Other than autocorrelation techniques, FROG offers a built-in consistency check to detect systematic errors. It involves computing the *marginals* of the FROG trace, that is, integrals of the trace with respect to delay or frequency. The marginals can be compared to the independently measured spectrum or autocorrelation. For an SHG FROG the time marginal yields the intensity autocorrelation and the frequency marginal yields the second-harmonic spectrum. The marginals of the SHG FROG traces in Fig. 12.30 are therefore given in the corresponding pictures of Fig. 12.27.

- FROG can also be used in a cross-correlation variant named XFROG [12.129]. In this case a known pulse is used to gate an unknown pulse (usually derived from the known one), where no spectral overlap between the pulses is required. Via sum- or difference-frequency generation or other nonlinear processes, pulses in the ultraviolet (UV) and infrared (IR) spectral range can be characterized. The technique has been refined for measuring pulses in the attojoule (per pulse) regime and is capable of measuring pulses with poor spatial coherence and random phase, such as fluorescence [12.130].

- In the sub-10 fs range SHG FROG has been demonstrated down to 4.5 fs pulse durations with the help of type I phase matching in a 10 μm thick BBO crystal [12.131]. In this regime the noncollinear beam geometry can also introduce beam smearing artefacts. Type II phase matching allows the use of a collinear SHG FROG geometry, which is free of geometrical smearing [12.132, 133]. The FROG traces generated in this arrangement do not contain the optical fringes associated with interferometric autocorrelations and, therefore, can be processed by existing SHG FROG algorithms.

- Making use of a thick SHG crystal as a frequency filter [12.134, 135] allows for the construction of an extremely simple and robust FROG setup that has been demonstrated for 800 nm pulses in the range from 20 fs to 5 ps for different spectral widths of the ultrashort pulses. The device was termed grating-eliminated no-nonsense observation of ultrafast incident laser light E-fields (GRENOUILLE) [12.6]. Spatial temporal distortions such as spatial chirp and pulse front tilt can also be measured via GRENOUILLE [12.136, 137] (spatial chirp: each frequency is displaced in the transverse spatial coordinates, often resulting from
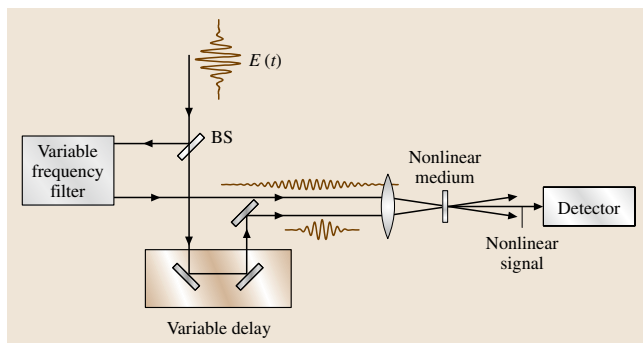
Fig. 12.31 Schematic of a frequency-domain phase measurement (FDPM) or spectrally and temporally resolved upconversion technique (STRUT) apparatus
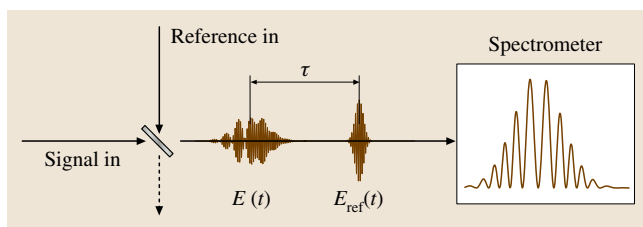

Fig. 12.32 Basic setup for spectral interferometry (SI) to characterize the phase difference between an ultrashort (signal) pulse $E(t)$ and a time-delayed reference pulse $E_{\text{ref}}(t)$
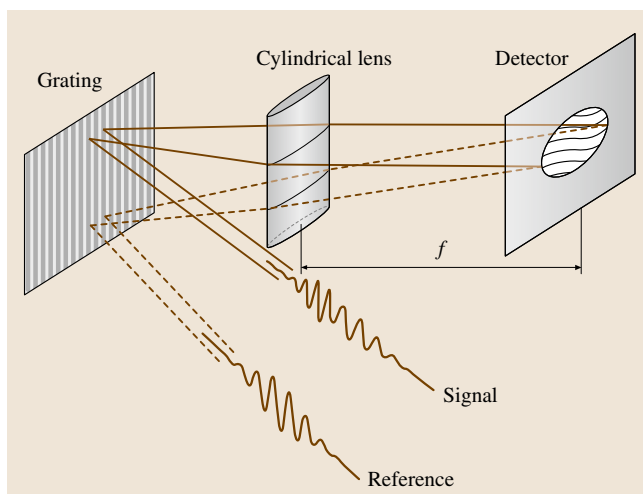
Fig. 12.33 Experimental setup for real-time spatial–spectral interference (SSI) measurements (after [12.128])

misaligned prism pairs and tilted windows; pulse front tilt: the pulse group fronts (intensity contours) are tilted with respect to the perpendicular to the
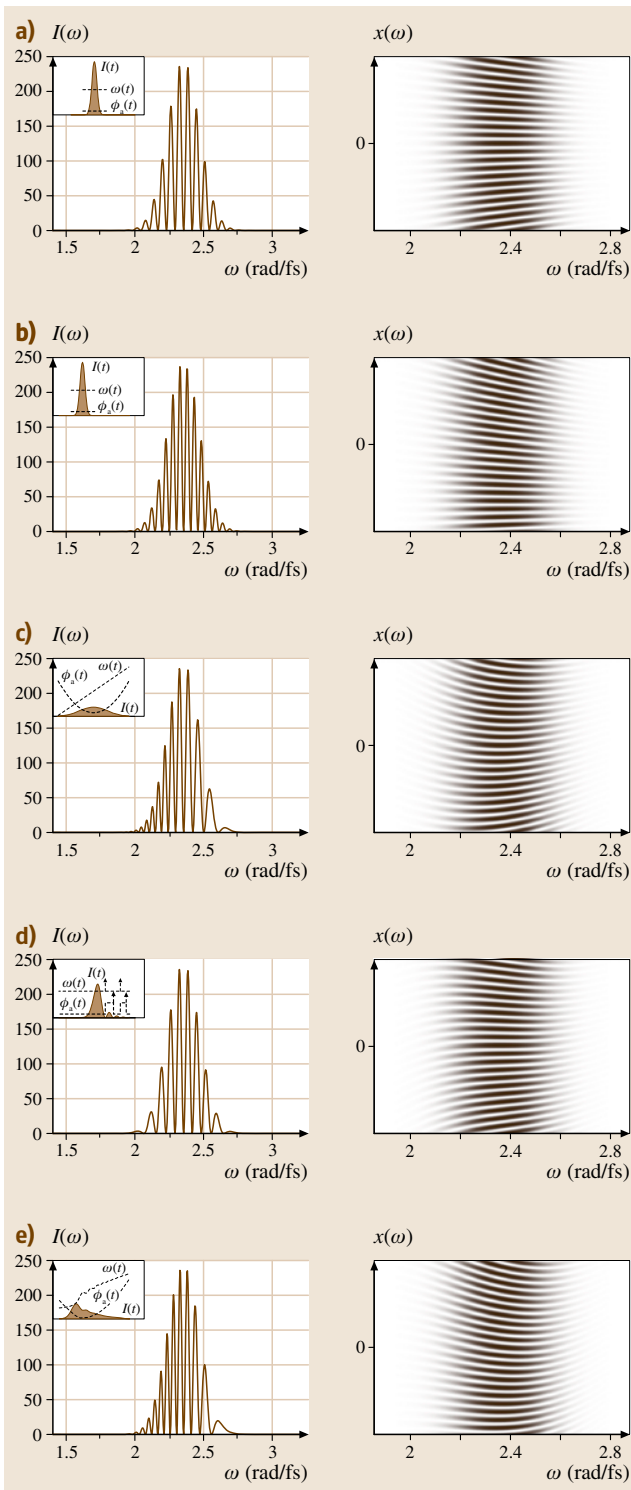
Fig. 12.34a–o Calculated spectral interference (SI) and spatial–spectral interference (SSI) traces for various ultrashort pulse shapes with a central wavelength of 800 nm according to the pulses displayed in Fig. 12.3. *Left* – SI: the time delay between both pulses is 100 fs. *Right*: SSI the angle 2Θ between both beams is 2°. The temporal intensity $I(t)$, the additional temporal phase $\Phi_a(t)$ and the instantaneous frequency $\omega(t)$ are shown in the *insets* as a reminder. **(a)** Bandwidth-limited Gaussian laser pulse of 10 fs duration, **(b)** bandwidth-limited Gaussian laser pulse of 10 fs duration shifted in time to −20 fs due to a linear phase term in the spectral domain ($\phi' = -20$ fs), **(c)** symmetrical broadened Gaussian laser pulse due to $\phi'' = 200$ fs^2, **(d)** third-order spectral phase ($\phi''' = 1000$ fs^3) leading to a quadratic group delay, **(e)** combined action of all spectral phase coefficients, **(a)**–**(d)**,**(f)** π step at the central frequency, **(g)** π step displaced from the central frequency, **(h)** sine modulation at the central frequency with $\phi(\omega) = 1\sin[20\,\text{fs}(\omega - \omega_0)]$, **(i)** cosine modulation at the central frequency with $\phi(\omega) = 1\cos[20\,\text{fs}(\omega - \omega_0)]$, **(j)** sine modulation at the central frequency with $\phi(\omega) = 1\sin[30\,\text{fs}(\omega - \omega_0)]$, **(k)** symmetrical clipping of spectrum, **(l)** blocking of the central frequency components, **(m)** off-center absorption, **(n)** self-phase modulation, (note the spectral broadening) **(o)** double pulse, with a pulse-to-pulse delay of 60 fs ◀, ▶

propagation direction, resulting from residual angular dispersion after pulse compressor or stretcher units).

- The wavelength limitation due to nonlinear optical processes can be circumvented by the use of multiphoton ionization as a nonlinearity. Measurements of interferometrically recorded energy-resolved photoelectron spectra generated by above-threshold ionization were demonstrated to yield FROG-type time–frequency distributions that were used to characterize ultrashort laser pulses [12.138]). This approach is potentially applicable to the XUV wavelength region.

Sonogram–Based Methods

Recording the sonogram involves slicing the frequency spectrum and measuring the arrival time of the frequency components. Experimentally this can be achieved, for example, by cross-correlation of a pulse with a frequency-filtered replica of the pulse in an instantaneous nonlinear medium (Fig. 12.31). The corresponding technique is known as frequency-domain phase measurement (FDPM) and is described in [12.139]. The method gives information on the group
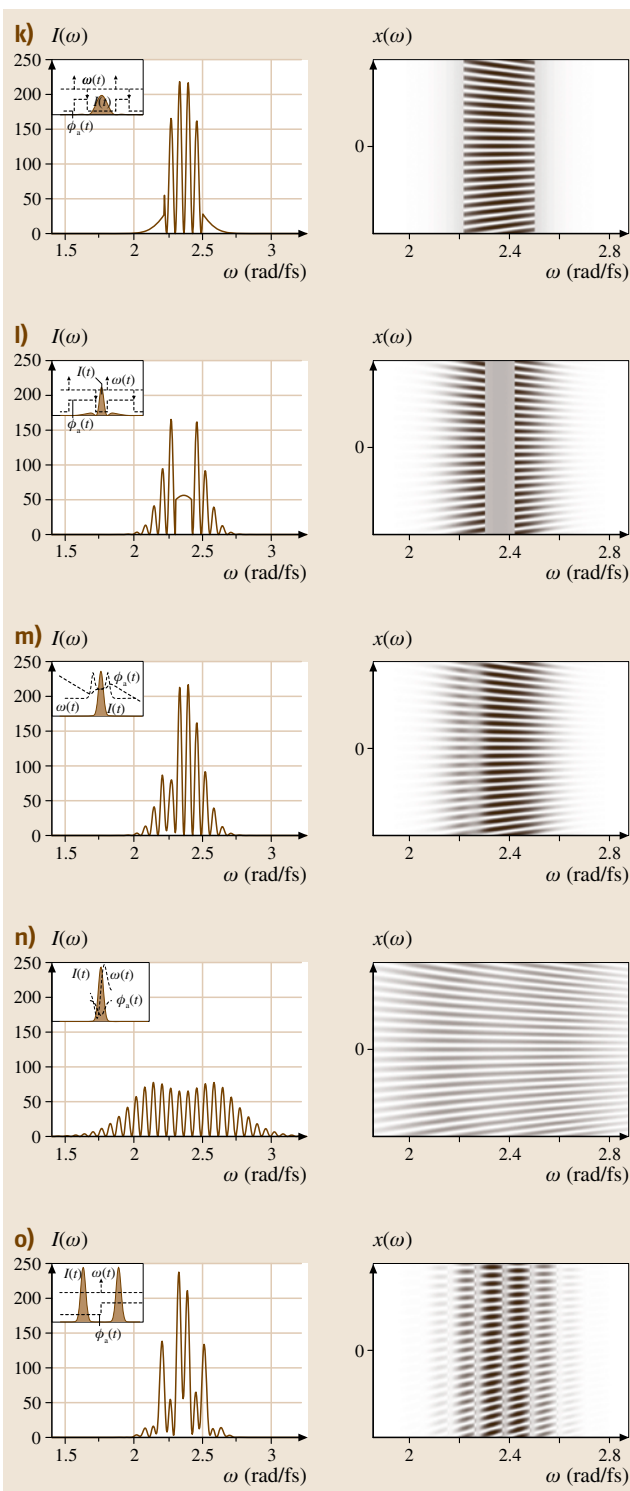
delay and an integration can be performed that gives the spectral phase function without any iterative algorithm. An experimental realization has been termed spectrally and temporally resolved upconversion technique (STRUT) [12.140] and also exists in a single-shot version [12.141]. As the sonogram and the spectrogram are mathematically equivalent FROG retrieval algorithms (being in principle somewhat slower) can also be used in this approach [12.141]. From a practical point of view the method is experimentally more involved than a FROG setup and it is less sensitive, because energy is lost at the filter before the nonlinear medium. In the SHG version, the STRUT apparatus and the FROG apparatus are identical when removing the frequency filter and using a spectrometer as the detector in Fig. 12.31.

12.3.5 Spectral Interferometry

The techniques described so far make use of nonlinear optical processes in order to determine the amplitude and phase of ultrashort laser pulses. Although, with the help of SHG FROG, pulses down to the picojoule regime can be measured in a multishot setup, shaped ultrashort laser pulses might spread out their energy over a time scale of picoseconds and thus prevent characterization with the help of nonlinear processes. However, as these pulses are usually created from an oscillator or an amplifier a well-characterized reference pulse is often available. This allows to make use of highly sensitive linear techniques to determine the amplitude and phase of an ultrashort laser pulse. The technique is named spectral interferometry (SI), frequency-domain interferometry or Fourier-transform spectral interferometry [12.6, 142–145]. The basic SI setup is depicted in Fig. 12.32. A well-characterized reference pulse $E_{ref}(t)$ and a modified signal pulse $E(t)$ derived from an experiment or a pulse shaper are directed collinearly into a spectrometer. The measured SI spectrum $S_{SI}(\omega)$ is proportional to the square of the Fourier transform of the sum of the two fields:

$$S_{SI}(\omega) \propto |\text{Fourier transform}\{E_{ref}(t) + E(t - \tau)\}|^2$$
$$\propto \left| \tilde{E}_{ref}(\omega) + \tilde{E}(\omega) e^{-i\omega\tau} \right|^2$$
$$\propto \left| \sqrt{I_{ref}(\omega)} e^{-i\phi_{ref}(\omega)} + \sqrt{I(\omega)} e^{-i\phi(\omega) - i\omega\tau} \right|^2$$
$$= I_{ref}(\omega) + I(\omega) + \sqrt{I_{ref}(\omega)}\sqrt{I(\omega)}$$
$$\times (e^{i\phi_{ref}(\omega) - i\phi(\omega) - i\omega\tau} + \text{c.c.})$$
$$= I_{ref}(\omega) + I(\omega) + 2\sqrt{I_{ref}(\omega)}\sqrt{I(\omega)}$$
$$\times \cos(\phi_{ref}(\omega) - \phi(\omega) - \omega\tau). \quad (12.87)$$
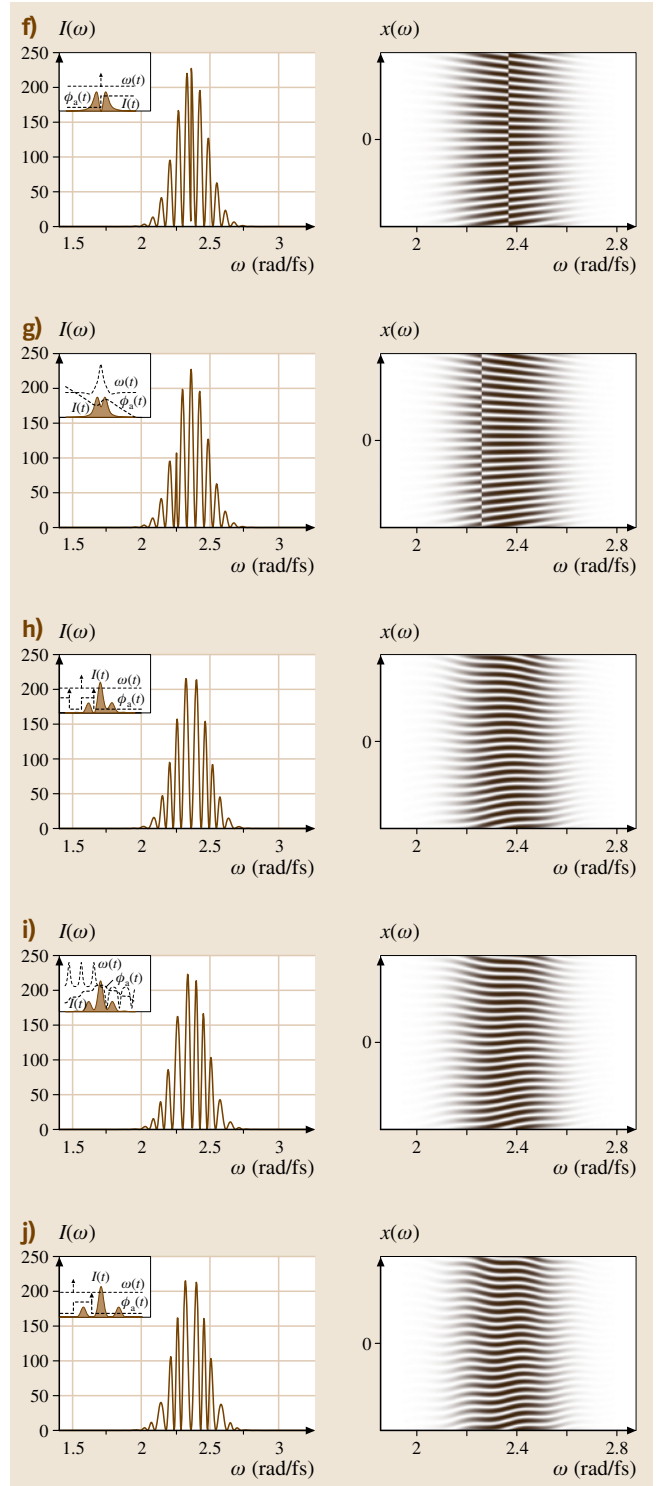
The phase difference

$$\Delta\phi(\omega) = \phi_{\text{ref}}(\omega) - \phi(\omega) \tag{12.88}$$

can be extracted from the measured $S_{\text{SI}}(\omega)$. Using the arcos function is not recommended because experimental noise can lead to large phase errors [12.145]. Commonly a Fourier-transform technique is used [12.145, 146] where the phase difference is extracted by the Fourier transform of the measured spectrum, ignoring the negative and zero-frequency components and shifting the positive-frequency components to direct current (DC) in order to remove the delay term $e^{-i\omega\tau}$. An inverse Fourier transform then yields the phase difference $\Delta\phi(\omega)$. With the help of the known reference phase $\phi_{\text{ref}}(\omega)$, $\phi(\omega)$ is finally obtained.

In the following some attributes of SI are summarized:

- SI requires the spectrum of the reference pulse to contain completely the spectrum of the unknown pulse.
- If the reference pulse and the signal pulse are identical, the phase difference is zero. The remaining oscillations on the spectrum due to the delay term are a convenient tool to adjust, for example, interferometric autocorrelator setups.
- Using the FROG technique for characterization of the reference pulse, the combined technique was termed temporal analysis by dispersing a pair of light E-fields (TADPOLE) [12.6, 147].
- SI is a heterodyne technique and amplifies the generally weak signal pulse (12.87). With the help of TADPOLE, pulse trains with an energy per pulse in the zeptojoule (zepto $= 10^{-21}$) regime have been analyzed [12.147].
- Once the reference phase is known, phase retrieval does not require an iterative procedure and is therefore fast. This allows, for example, for the synthesis of arbitrary laser pulse shapes with the help of feedback-controlled femtosecond pulse shaping techniques [12.148]. Together with its high sensitivity, TADPOLE is well suited to the characterization of complex-shaped femtosecond laser pulses. Furthermore, in a dual-channel setup SI has been used to characterize complex polarization-shaped femtosecond laser pulses [12.78]. The setup for the characterization of time-dependent polarization profiles has been called polarization-labeled interference versus wavelength for only a glint (POLLIWOG) [12.149].

- SI can also be implemented in a spatial variation, where the reference pulse and the signal pulse propagate at an angle of 2Θ with respect to each other (Fig. 12.33). The frequency components of the optical fields of the two propagating pulses are mapped in one dimension by a diffraction grating and a cylindrical lens and interfere at the focal plane of the lens. The technique is called spatial–spectral interference (SSI). The corresponding device is a convenient tool for optimizing various setups such as pulse shapers and compressors as the fringe patterns are displayed in real time and the information is encoded in an intuitively interpretable pattern [12.128]. A comparison of calculated SI and SSI traces for various ultrashort pulse distortions is given in Fig. 12.34.
- There also exists a self-referencing variant of SI that does not require separate characterization of the ref-erence pulse. This technique is called spectral phase interferometry for direct electric field reconstruction (SPIDER) [12.17,150] and involves appropriate temporal stretching of a reference pulse followed by sum-frequency generation with two well-displaced copies of the unstretched input pulse. This technique has been successfully demonstrated for the characterization of ultrashort pulses in the few-cycle regime [12.151]. Due to the nonlinear process involved, SPIDER is less sensitive than TADPOLE. A comparison of SHG FROG and SPIDER for sub-ten-femtosecond pulse characterization is given in [12.152]. A spatially resolved version of SPIDER has also been demonstrated [12.153]. A setup that is capable of characterizing a pulse at the interaction point of an experiment, called zero additional phase (ZAP) SPIDER, has been demonstrated for visible and sub-20-femtosecond ultraviolet pulses [12.154].

References

12.1 U. Keller: Recent developments in compact ultra-fast lasers, Science **424**, 831–838 (2003)

12.2 B. Wilhelmi, J. Herrmann: *Lasers for Ultrashort Light Pulses* (North-Holland, Amsterdam 1987)

12.3 S.A. Akhmanov, V.A. Vysloukh, A.S. Chirkin: *Optics of Femtosecond Pulses* (American Institute of Physics, New York 1992)

12.4 J.C. Diels, W. Rudolph: *Ultrashort Laser Pulse Phenomena* (Academic, San Diego 1996)

12.5 C.E. Rullière: *Femtosecond Laser Pulses* (Springer, Berlin Heidelberg 1998)

12.6 R. Trebino: *Frequency-Resolved Optical Gating: The Measurement of Ultrashort Laser Pulses* (Kluwer Academic Publishers, Norwell 2000)

12.7 D.J. Jones, S.A. Diddams, J.K. Ranka, A. Stentz, R.S. Windeler, J.L. Hall, S.T. Cundiff: Carrier-envelope phase control of femtosecond mode-locked lasers and direct optical frequency synthesis, Science **288**, 635–639 (2000)

12.8 A. Apolonski, A. Poppe, G. Tempea, C. Spielmann, T. Udem, R.H.T.W. Holzwarth, F. Krausz: Controlling the phase evolution of few-cycle light pulses, Phys. Rev. Lett. **85**, 740–743 (2000)

12.9 F.W. Helbing, G. Steinmeyer, J. Stenger, H.R. Telle, U. Keller: Carrier-envelope-offset dynamics and stabilization of femtosecond pulses, Appl. Phys. B **74**, 35–42 (2002)

12.10 M. Kakehata, Y. Fujihira, H. Takada, Y. Kobayashi, K. Torizuka, T. Homma, H. Takahashi: Measurements of carrier-envelope phase changes of 100-Hz amplified laser pulses, Appl. Phys. B **74**, 43–50 (2002)

12.11 G.G. Paulus, F. Grasbon, H. Walther, P. Villoresi, M. Nisoll, S. Stagira, E. Priori, S. De Silvestri: Absolute-phase phenomena in photoionization with few-cycle laser pulses, Nature **414**, 182–184 (2001)

12.12 J. Ye, S.T. Cundiff, S. Foreman, T.M. Fortier, J.L. Hall, K.W. Holman, D.J. Jones, J.D. Jost, H.C. Kapteyn, K.A.H.V. Leeuwen, L.S. Ma, M.M. Murnane, J.L. Peng, R.K. Shelton: Phase-coherent synthesis of optical frequencies and waveforms, Appl. Phys. B **74**, 27–34 (2002)

12.13 A. Baltuska, T. Udem, M. Uiberacker, M. Hentschel, E. Goulielmakis, C. Gohle, R. Holzwarth, V.S. Yakovlev, A. Scrinzi, T.W. Hänsch, F. Krausz: Attosecond control of electronic processes by intense light fields, Nature **421**, 611–615 (2003)

12.14 D.J. Bradley, G.H.C. New: Ultrashort pulse measurements, Proc. IEEE **62**, 313–345 (1974)

12.15 L. Cohen: *Time-Frequency Analysis* (Prentice Hall, New Jersey 1995)

12.16 L. Mandel, E. Wolf: *Optical Coherence and Quantum Optics* (Cambridge Univ. Press, Cambridge 1995)

12.17 C. Iaconis, I.A. Walmsley: Self-referencing spectral interferometry for measuring ultrashort optical pulses, IEEE J. Quant. Electron. **35**, 501–509 (1999)

12.18 T. Feurer, M. Hacker, B. Schmidt, G. Stobrawa: *A Virtual Femtosecond-Laser Laboratory* (Inst. Appl. Phys., Bern 2004), (2000), http://www.lab2.de

12.19 R. Bracewell: *The Fourier Transform and Its Applications* (McGraw-Hill, Singapore 2000)

12.20 A.W. Albrecht, J.D. Hybl, S.M. Gallagher Faeder, D.M. Jonas: Experimental distinction between

phase shifts and time delays: Implications for femtosecond spectroscopy and coherent control of chemical reactions, J. Chem. Phys. **111**, 10934–10956 (1999)

12.21 A. Präkelt, M. Wollenhaupt, C. Sarpe-Tudoran, T. Baumert: Phase control of a two-photon transition with shaped femtosecond laser-pulse sequences, Phys. Rev. A **70**, 063407–1–063407–10 (2004)

12.22 K.L. Sala, G.A. Kenney-Wallace, G.E. Hall: CW autocorrelation measurements of picosecond laser pulses, IEEE J. Quant. Electron. **16**, 990–996 (1980)

12.23 E. Sorokin, G. Tempea, T. Brabec: Measurement of the root-mean-square width and the root-mean-square chirp in ultrafast optics, J. Opt. Soc. Am. B **17**, 146–150 (2000)

12.24 L. Cohen: Time–frequency distributions – a review, Proc. IEEE **77**, 941–981 (1989)

12.25 I. Walmsley, L. Waxer, C. Dorrer: The role of dispersion in ultrafast optics, Rev. Sci. Instrum. **72**, 1–29 (2001)

12.26 S. De Silvestri, P. Laporta, O. Svelto: The role of cavity dispersion in CW mode-locked lasers, IEEE J. Quant. Electron. **20**, 533–539 (1984)

12.27 J.D. McMullen: Chirped-pulse compression in strongly dispersive media, J. Opt. Soc. Am. **67**, 1575–1578 (1977)

12.28 M. Wollenhaupt, A. Präkelt, C. Sarpe-Tudoran, D. Liese, T. Bayer, T. Baumert: Femtosecond strong-field quantum control with sinusoidally phase-modulated pulses, Phys. Rev. A **73**, 063409–1–063409–15 (2006)

12.29 A.M. Weiner: Femtosecond optical pulse shaping and processing, Prog. Quant. Electron. **19**, 161–237 (1995)

12.30 P. Meystre, M. Sargent III: *Elements of Quantum Optics* (Springer, Berlin Heidelberg 1998)

12.31 R.L. Fork, O.E. Martinez, J.P. Gordon: Negative dispersion using pairs of prism, Opt. Lett. **9**, 150–152 (1984)

12.32 O.E. Martinez, J.P. Gordon, R.L. Fork: Negative group velocity dispersion using refraction, J. Opt. Soc. Am. A **1**, 1003–1006 (1984)

12.33 F.J. Duarte: Generalized multiple-prism dispersion theory for pulse compression in ultrafast dye lasers, Opt. Quant. Electron. **19**, 223–229 (1987)

12.34 V. Petrov, F. Noack, W. Rudolph, C. Rempel: Intracavity dispersion compensation and extracavity pulse compression using pairs of prisms, Exp. Tech. Phys. **36**, 167–173 (1988)

12.35 C.P.J. Barty, C.L. Gordon, B.E. Lemoff: Multiterawatt 30-fs Ti:Sapphire laser system, Opt. Lett. **19**, 1442–1444 (1994)

12.36 D. Strickland, G. Mourou: Compression of amplified chirped optical pulses, Opt. Commun. **56**, 219–221 (1985)

12.37 S. Backus, C.G. Durfee III, M.M. Murnane, H.C. Kapteyn: High power ultrafast lasers, Rev. Sci. Instrum. **69**, 1207–1223 (1998)

12.38 C.H.B. Cruz, P.C. Becker, R.L. Fork, C.V. Shank: Phase correction of femtosecond optical pulses using a combination of prisms and gratings, Opt. Lett. **13**, 123–125 (1988)

12.39 R.L. Fork, C.H. Brito Cruz, C.H. Becker, C.V. Shank: Compression of optical pulses to six femtoseconds by using cubic phase compensation, Opt. Lett. **12**, 483–485 (1987)

12.40 E.B. Treacy: Optical pulse compression with diffraction gratings, IEEE J. Quant. Electron. **5**, 454–458 (1969)

12.41 A. Suzuki: Complete analysis of a two mirror unit magnification system, Appl. Opt. **22**, 3943 (1983)

12.42 G. Cheriaux, P. Rousseau, F. Salin, J.P. Chambaret, B. Walker, L.F. DiMauro: Aberration-free stretcher design for ultrashort pulse amplification, Opt. Lett. **21**, 414 (1996)

12.43 O.E. Martinez: Matrix formalism for pulse compressors, IEEE J. Quant. Electron. **24**, 2530–2536 (1988)

12.44 O.E. Martinez: Grating and prism compressor in the case of finite beam size, J. Opt. Soc. Am. B **3**, 929–934 (1986)

12.45 F. Gires, P. Tournois: Interferometre utilisable pour la compression d'impulsions lumineuses modulees en frequence, C. R. Acad. Sci. Paris **258**, 6112–6115 (1964)

12.46 P.M.W. French: The generation of ultrashort laser pulses, Rep. Prog. Phys. **58**, 169–267 (1995)

12.47 W. Demtröder: *Laser Spectroscopy* (Springer, Berlin Heidelberg 1996)

12.48 J. Heppner, J. Kuhl: Intracavity chirp compensation in a colliding pulse mode-locked laser using thin-film interferometers, Appl. Phys. Lett. **47**, 453–455 (1985)

12.49 R. Szipöcs, K. Ferencz, C. Spielmann, F. Krausz: Chirped multilayer coatings for broadband dispersion control in femtosecond lasers, Opt. Lett. **19**, 201–203 (1994)

12.50 A. Stingl, C. Spielmann, F. Krausz, R. Szipocs: Generation of 11 fs pulses from a Ti:sapphire laser without the use of prisms, Opt. Lett. **19**, 204 (1994)

12.51 N. Matuschek, F.X. Kärtner, U. Keller: Exact coupled mode theories for multilayer interference coatings with arbitrary strong index modulation, IEEE J. Quant. Electron. **33**, 295–302 (1997)

12.52 N. Matuschek, F.X. Kärtner, U. Keller: Analytical design of double-chirped mirrors with custom-tailored dispersion characteristics, IEEE J. Quant. Electron. **35**, 129–137 (1999)

12.53 D.H. Sutter, G. Steinmeyer, L. Gallmann, N. Matuschek, F. Morier-Genoud, U. Keller, V. Scheuer, G. Angelow, T. Tschudi: Semiconductor saturable-absorber mirror-assisted Kerr-lens mode-locked Ti:sapphire laser producing pulses in the two-cycle regime, Opt. Lett. **24**, 631–633 (1999)

12.54 N. Matuschek, L. Gallmann, D.H. Sutter, G. Steinmeyer, U. Keller: Back-side-coated chirped mirrors with ultra-smooth broadband dispersion characteristics, Appl. Phys. B **71**, 509–522 (2000)

12.55 A.M. Weiner: Femtosecond pulse shaping using spatial light modulators, Rev. Sci. Instrum. **71**, 1929–1960 (2000)

12.56 R.S. Judson, H. Rabitz: Teaching lasers to control molecules, Phys. Rev. Lett. **68**, 1500–1503 (1992)

12.57 T. Baumert, T. Brixner, V. Seyfried, M. Strehle, G. Gerber: Femtosecond pulse shaping by an evolutionary algorithm with feedback, Appl. Phys. B **65**, 779–782 (1997)

12.58 C.J. Bardeen, V.V. Yakolev, K.R. Wilson, S.D. Carpenter, P.M. Weber, W.S. Warren: Feedback quantum control of molecular electronic population transfer, Chem. Phys. Lett. **280**, 151–158 (1997)

12.59 D. Yelin, D. Meshulach, Y. Silberberg: Adaptive femtosecond pulse compression, Opt. Lett. **22**, 1793–1795 (1997)

12.60 A. Assion, T. Baumert, M. Bergt, T. Brixner, B. Kiefer, V. Seyfried, M. Strehle, G. Gerber: Control of chemical reactions by feedback-optimized phase-shaped femtosecond laser pulses, Science **282**, 919–922 (1998)

12.61 T. Brixner, M. Strehle, G. Gerber: Feedback-controlled optimization of amplified femtosecond laser pulses, Appl. Phys. B **68**, 281–284 (1999)

12.62 R. Bartels, S. Backus, E. Zeek, L. Misoguti, G. Vdovin, I.P. Christov, M.M. Murnane, H.C. Kapteyn: Shaped-pulse optimization of coherent emission of high-harmonic soft X-rays, Nature **406**, 164–166 (2000)

12.63 T. Brixner, N.H. Damrauer, P. Niklaus, G. Gerber: Photoselective adaptive femtosecond quantum control in the liquid phase, Nature **414**, 57–60 (2001)

12.64 J.L. Herek, W. Wohlleben, R. Cogdell, D. Zeidler, M. Motzkus: Quantum control of energy flow in light harvesting, Nature **417**, 533–535 (2002)

12.65 J. Kunde, B. Baumann, S. Arlt, F. Morier-Genoud, U. Siegner, U. Keller: Adaptive feedback control of ultrafast semiconductor nonlinearities, Appl. Phys. Lett. **77**, 924–926 (2000)

12.66 T.C. Weinacht, R. Bartels, S. Backus, P.H. Bucksbaum, B. Pearson, J.M. Geremia, H. Rabitz, H.C. Kapteyn, M.M. Murnane: Coherent learning control of vibrational motion in room temperature molecular gases, Chem. Phys. Lett. **344**, 333–338 (2001)

12.67 R.J. Levis, G.M. Menkir, H. Rabitz: Selective bond dissociation and rearrangement with optimally tailored, strong-field laser pulses, Science **292**, 709–713 (2001)

12.68 C. Daniel, J. Full, L. Gonzáles, C. Lupulescu, J. Manz, A. Merli, S. Vajda, L. Wöste: Deciphering the reaction dynamics underlying optimal control laser fields, Science **299**, 536–539 (2003)

12.69 T. Brixner, G. Gerber: Quantum control of gas-phase and liquid-phase femtochemistry, Chem. Phys. Chem **4**, 418–438 (2003)

12.70 M. Wollenhaupt, A. Präkelt, C. Sarpe-Tudoran, D. Liese, T. Baumert: Strong field quantum control by selective population of dressed states, J. Opt. B **7**, S270–S276 (2005)

12.71 C. Horn, M. Wollenhaupt, M. Krug, T. Baumert, R. de Nalda, L. Banares: Adaptive control of molecular alignment, Phys. Rev. A **73**, 031401-1–031401-4 (2006)

12.72 T. Brixner, G. Gerber: Femtosecond polarization pulse shaping, Opt. Lett. **26**, 557–559 (2001)

12.73 A. Präkelt, M. Wollenhaupt, A. Assion, C. Horn, C. Sarpe-Tudiran, M. Winter, T. Baumert: A compact, robust and flexible setup for femtosecond pulse shaping, Rev. Sci. Instrum. **74**, 4950–4953 (2003)

12.74 L. Xu, N. Nakagawa, R. Morita, H. Shigekawa, M. Yamashita: Programmable chirp compensation for 6-fs pulse generation with a prism-pair-formed pulse shaper, IEEE J. Quant. Electron. **36**, 893–899 (2000)

12.75 G. Stobrawa, M. Hacker, T. Feurer, D. Zeidler, M. Motzkus, F. Reichel: A new high-resolution femtosecond pulse shaper, Appl. Phys. B **72**, 627–630 (2001)

12.76 M.M. Wefers, K.A. Nelson: Programmable phase and amplitude femtosecond pulse shaping, Opt. Lett. **18**, 2032–2034 (1993)

12.77 A. Präkelt, M. Wollenhaupt, C. Sarpe-Tudoran, A. Assion, T. Baumert: Filling a spectral hole via self-phase modulation, Appl. Phys. Lett. **87**, 121113-1–121113-3 (2005)

12.78 T. Brixner, G. Krampert, P. Niklaus, G. Gerber: Generation and characterization of polarization-shaped femtosecond laser pulses, Appl. Phys. B **74**, 133–144 (2002)

12.79 T. Brixner, G. Krampert, T. Pfeifer, R. Selle, G. Gerber, M. Wollenhaupt, O. Graefe, C. Horn, D. Liese, T. Baumert: Quantum control by ultrafast polarization shaping, Phys. Rev. Lett. **92**, 208301-1–208301-4 (2004)

12.80 M. Wollenhaupt, V. Engel, T. Baumert: Femtosecond laser photoelectron spectroscopy on atoms and small molecules: Prototype studies in quantum control, Annu. Rev. Phys. Chem. **56**, 25–56 (2005)

12.81 E. Zeek, K. Maginnis, S. Backus, U. Russek, M.M. Murnane, G. Mourou, H.C. Kapteyn: Pulse compression by use of deformable mirrors, Opt. Lett. **24**, 493–495 (1999)

12.82 M. Hacker, G. Stobrawa, R.A. Sauerbrey, T. Buckup, M. Motzkus, M. Wildenhain, A. Gehner: Micromirror SLM for femtosecond pulse shaping in the ultraviolet, Appl. Phys. B **76**, 711–714 (2003)

12.83 J.X. Tull, M.A. Dugan, W.S. Warren: High-resolution, ultrafast laser pulse shaping and its

applications. In: *Adv. in Magn. and Opt. Resonance*, ed. by W.S. Warren (Academic, New York 1997) pp. 1–65

12.84 D. Goswami: Optical pulse shaping approaches to coherent control, Phys. Rep. **374**, 385–481 (2003)

12.85 P. Tournois: Acousto-optic programmable dispersive filter for adaptive compensation of group delay time dispersion in laser systems, Opt. Commun. **140**, 245–249 (1997)

12.86 F. Verluise, V. Laude, Z. Cheng, C. Spielmann, P. Tournois: Amplitude and phase control of ultrashort pulses by use of an acousto-optic programmable dispersive filter: pulse compression and shaping, Opt. Lett. **25**, 575–577 (2000)

12.87 F. Verluise, V. Laude, J.P. Huignard, P. Tournois: Arbitrary dispersion control of ultrashort optical pulses using acoustic waves, J. Opt. Soc. Am. B **17**, 138–145 (2000)

12.88 J.C. Vaughan, T. Feurer, K.A. Nelson: Automated two-dimensional femtosecond pulse shaping, J. Opt. Soc. Am. B **19**, 2489–2495 (2002)

12.89 T. Feurer, J.C. Vaughan, K.A. Nelson: Spatiotemporal coherent control of lattice vibrational waves, Science **299**, 374–377 (2003)

12.90 G.H.C. New: The generation of ultrashort light pulses, Rep. Prog. Phys. **46**, 877–971 (1983)

12.91 J.D. Simon: Ultrashort light pulses, Rev. Sci. Instrum. **60**, 3597–3624 (1989)

12.92 P.M.W. French: Ultrafast solid state lasers, Contemp. Phys. **37**, 283–301 (1996)

12.93 H.A. Haus: Mode-locking of lasers, IEEE J. Quant. Electron. **6**, 1173–1185 (2000)

12.94 G.R. Fleming: *Chemical Applications of Ultrafast Spectroscopy* (Oxford Univ. Press, New York 1986)

12.95 O. Svelto: *Principles of Lasers* (Plenum, New York 1998)

12.96 A.E. Siegmann: *Lasers* (Univ. Sci. Books, Mill Valley 1986)

12.97 A. Yariv: *Quantum Electronics* (Wiley, New York 1989)

12.98 M.E. Fermann, A. Galvanauskas, G. Sucha: *Ultrafast Lasers – Technology and Applications* (Marcel Dekker, New York 2003)

12.99 J.A. Valdmanis, R.L. Fork: Design considerations for a femtosecond pulse laser balancing self phase modulation, group velocity dispersion, saturable absorption and saturable gain, IEEE J. Quant. Electron. **22**, 112–118 (1986)

12.100 R. Ell, U. Morgner, F.X. Kärtner, J. Fujimoto, E.P. Ippen, V. Scheuer, G. Angelow, T. Tschudi, A. Lederer, A. Boiko, B. Luther-Davies: Generation of 5-fs pulses and octave-spanning spectra directly from a Ti:sapphire laser, Opt. Lett. **26**, 373–375 (2001)

12.101 D.E. Spence, P.N. Kean, W. Sibbett: 60-fs pulse generation from a self-mode-locked Ti:sapphire laser, Opt. Lett. **16**, 42–44 (1991)

12.102 K.K. Hamamatsu Photonics: *Guide to Streak Cameras* (1999), http://www.hamamatsu.com

12.103 Y. Tsuchiya: Advances in streak camera instrumentation for the study of biological and physical processes, IEEE J. Quant. Electron. **20**, 1516–1528 (1984)

12.104 E.P. Ippen, C.V. Shank: *Ultrashort Light Pulses*, ed. by S.L. Shapiro (Springer, Berlin, Heidelberg 1977), p. 83

12.105 J.K. Ranka, A.L. Gaeta, A. Baltuska, M.S. Pshenichnikov, D.A. Wiersma: Autocorrelation measurements of 6-fs pulses based on the two-photon-induced photocurrent in a GaAsP photodiode, Opt. Lett. **22**, 1344–1346 (1997)

12.106 W. Rudolph, M. Sheik-Bahae, A. Bernstein, L.F. Lester: Femtosecond autocorrelation measurements based on two-photon photoconductivity in ZnSe, Opt. Lett. **22**, 313–315 (1997)

12.107 F. Salin, P. Georges, A. Brun: Single-shot measurements of a 52-fs pulse **26**, 4528–4531 (1987)

12.108 A. Brun, P. Georges, G. Le Saux, F. Salin: Single-shot characterization of ultrashort light pulses, J. Phys. D **24**, 1225–1233 (1991)

12.109 G. Szabó, Z. Bor, A. Müller: Phase-sensitive single-pulse autocorrelator for ultrashort laser pulses, Opt. Lett. **13**, 746–748 (1988)

12.110 B.W. Shore: *The Theory of Coherent Atomic Excitation*, Vol. 1 (Wiley, New York 1990)

12.111 J.C. Diels, J.J. Fontaine, I.C. McMichael, F. Simoni: Control and measurement of ultrashort pulse shapes (in amplitude and phase) with femtosecond accuracy, Appl. Opt. **24**, 1270–1282 (1985)

12.112 D. Meshulach, Y. Silberberg: Coherent quantum control of two-photon transitions by a femtosecond laser pulse, Nature **396**, 239–242 (1998)

12.113 V.V. Lozovoy, I. Pastirk, A. Walowicz, M. Dantus: Multiphoton intrapulse interference. II. Control of two- and three-photon laser induced fluorescence with shaped pulses, J. Chem. Phys. **118**, 3187–3196 (2003)

12.114 V.V. Lozovoy, I. Pastirk, M. Dantus: Multiphoton intrapulse interference. IV Ultrashort laser pulse spectral phase characterization and compensation, Opt. Lett. **29**, 1–3 (2004)

12.115 J. Peatross, A. Rundquist: Temporal decorrelation of short laser pulses, J. Opt. Soc. Am. B **15**, 216–222 (1998)

12.116 K. Naganuma, K. Mogi, H. Yamada: General method for ultrashort light pulse chirp measurement, IEEE J. Quant. Electron. **25**, 1225–1233 (1989)

12.117 E.W. Van Stryland: The effect of pulse to pulse variation on ultrashort pulsewidth measurements, Opt. Commun. **31**, 93–96 (1979)

12.118 S. Quian, D. Chen: *Joint Time–Frequency Analysis. Methods and Applications* (Prentice Hall, New Jersey 1996)

12.119 M.O. Scully, M.S. Zubairy: *Quantum Optics* (Cambridge Univ. Press, Cambridge 1995)

12.120 W.P. Schleich: *Quantum Optics in Phase Space* (Wiley-VCH, Weinheim 2001)

12.121 H.O. Bartelt, K.H. Brenner, A.W. Lohmann: The Wigner distribution function and its optical production, Opt. Commun. **32**, 32–38 (1980)

12.122 J. Paye, A. Migus: Space time Wigner functions and their application to the analysis of a pulse shaper, J. Opt. Soc. Am. B **12**, 1480–1490 (1995)

12.123 H.W. Lee: Generalized antinormally ordered quantum phase-space distribution functions, Phys. Rev. A **50**, 2746–2749 (1994)

12.124 D. Lalovic, D.M. Davidovic, N. Bijedic: Quantum mechanics in terms of non-negative smoothed Wigner functions, Phys. Rev. A **46**, 1206–1212 (1992)

12.125 R. Trebino, K.W. DeLong, D.N. Fittinghoff, J.N. Sweetser, M.A. Krumbügel, B.A. Richman, D.J. Kane: Measuring ultrashort laser pulses in the time-frequency domain using frequency-resolved optical gating, Rev. Sci. Instrum. **68**, 3277–3295 (1997)

12.126 H. Stark: *Image Recovery: Theory and Application* (Academic, Orlando 1987)

12.127 D. Kane: Recent progress toward real-time measurement of ultrashort laser pulses, IEEE J. Quant. Electron. **35**, 421–431 (1999)

12.128 D. Meshulach, D. Yelin, Y. Silberberg: Real-time spatial-spectral interference measurements of ultrashort optical pulses, J. Opt. Soc. Am. B **14**, 2095–2098 (1997)

12.129 S. Linden, J. Kuhl, H. Giessen: Amplitude and phase characterization of weak blue ultrashort pulses by downconversion, Opt. Lett. **24**, 569–571 (1999)

12.130 J. Zhang, A.P. Shreenath, M. Kimmel, E. Zeek, R. Trebino: Measurement of the intensity and phase of attojoule femtosecond light pulses using optical-parametric-amplification cross-correlation frequency-resolved optical gating, Opt. Express **11**, 601–609 (2003)

12.131 A. Baltuska, M. Pshenichnikov, D.A. Wiersma: Amplitude and phasecharacterization of 4.5-fs pulses by frequency-resolved optical gating, Opt. Lett. **23**, 1474–1476 (1998)

12.132 D.N. Fittinghoff, J. Squier, C.P.J. Barty, J.N. Sweetser, R. Trebino, M. Müller: Collinear type II second-harmonic-generation frequency-resolved optical gating for use with high-numerical aperture objectives, Opt. Lett. **23**, 1046–1048 (1998)

12.133 L. Gallmann, G. Steinmeyer, D.H. Sutter, N. Matuschek, U. Keller: Collinear type II second harmonic-generation frequency-resolved optical gating for the characterization of sub-10-fs optical pulses, Opt. Lett. **25**, 269–271 (2000)

12.134 P. O'Shea, M. Kimmel, X. Gu, R. Trebino: Highly simplified device for ultrashort-pulse measurement, Opt. Lett. **26**, 932–934 (2001)

12.135 C. Radzewicz, P. Wasylczyk, J.S. Krasinski: A poor man's FROG, Opt. Commun. **186**, 329–333 (2000)

12.136 S. Akturk, M. Kimmel, P. O'Shea, R. Trebino: Measuring pulse-front tilt in ultrashort pulses using GRENOUILLE, Opt. Express **11**, 491–501 (2003)

12.137 S. Akturk, M. Kimmel, P. O'Shea, R. Trebino: Measuring spatial chirp in ulrashort pulses using single-shot frequency-resolved optical gating, Opt. Express **11**, 68–78 (2003)

12.138 M. Winter, M. Wollenhaupt, T. Baumert: Coherent matter waves for ultrafast laser pulse characterization, Opt. Commun. **264**, 285–292 (2006)

12.139 J.L.A. Chilla, O.E. Martinez: Direct determination of the amplitude and the phase of femtosecond light pulses, Opt. Lett. **16**, 39–41 (1991)

12.140 J.P. Foing, J.P. Likforman, M. Joffre, A. Migus: Femtosecond pulse phase measurement by spectrally resolved up-conversion; application to continuum compression, IEEE J. Quant. Electron. **28**, 2285–2290 (1992)

12.141 J.K. Rhee, T.S. Sosnowski, A.C. Tien, T.B. Norris: Real-time dispersion analyzer of femtosecond laser pulses with use of a spectrally and temporally resolved upconversion technique, J. Opt. Soc. Am. B **13**, 1780–1785 (1996)

12.142 C. Froehly, A. Lacourt, J.C. Vienot: Time impulse response and time frequency response of optical pupils. Experimental confirmation and applications, Nouv. Rev. Opt. **4**, 183–196 (1973)

12.143 J. Piasecki, B. Colombeau, M. Vampouille, C. Froehly, J.A. Arnaud: Nouvelle methode de mesure de la reponse impulsionnelle des fibres optiques, Appl. Opt. **19**, 3749–3755 (1980)

12.144 F. Reynaud, F. Salin, A. Barthelemy: Measurement of phase shifts introduced by nonlinear optical phenomena on subpicosecond pulses, Opt. Lett. **14**, 275–277 (1989)

12.145 L. Lepetit, G. Cheriaux, M. Joffre: Linear techniques of phase measurement by femtosecond spectral interferometry for applications in spectroscopy, J. Opt. Soc. Am. B **12**, 2467–2474 (1995)

12.146 M. Takeda, H. Ina, S. Kobayashi: Fourier-transform method of fringe-pattern analysis for computer-based topography and interferometry, J. Opt. Soc. Am. **72**, 156–159 (1981)

12.147 D.N. Fittinghoff, J.L. Bowie, J.N. Sweetser, R.T. Jennings, K.W. DeLong, M.A. Krumbügel, R. Trebino, I.A. Walmsley: Measurement of the intensity and phase of ultraweak, ultrashort laser pulses, Opt. Lett. **21**, 884–886 (1996)

12.148 T. Brixner, A. Oehrlein, M. Strehle, G. Gerber: Feedback-controlled femtosecond pulse shaping, Appl. Phys. B **70**, S119–S124 (2000)

12.149 W.J. Walecki, D.N. Fittinghoff, A.L. Smirl, R. Trebino: Characterization of the polarization state of weak ultrashort coherent signals by dual-channel spectral interferometry, Opt. Lett. **22**, 81–83 (1997)

12.150 C. Iaconis, A. Walmsley: Spectral phase interferometry for direct electric-field reconstruction of ultrashort optical pulses, Opt. Lett. **23**, 792–794 (1998)

12.151 L. Gallmann, D.H. Sutter, N. Matuschek, G. Stein-meyer, U. Keller, C. Iaconis, I.A. Walmsley: Characterization of sub-6-fs optical pulses with spectral phase interferometry for direct electric-field reconstruction, Opt. Lett. **24**, 1314–1316 (1999)

12.152 L. Gallmann, D.H. Sutter, N. Matuschek, G. Stein-meyer, U. Keller: Techniques for the characterization of sub-10-fs optical pulses: a comparison, Appl. Phys. B **70**, 67–75 (2000)

12.153 L. Gallmann, G. Steinmeyer, D.H. Sutter, T. Rupp, C. Iaconis, I.A. Walmsley, U. Keller: Spatially resolved amplitude and phase characterization of femtosecond optical pulses, Opt. Lett. **26**, 96–98 (2001)

12.154 P. Baum, S. Lochbrunner, E. Riedle: Zero-aditional-phase SPIDER: full characterization of visible and sub 20-fs ultraviolet pulses, Opt. Lett. **29**, 210–212 (2004)